Iron-based electrode materials for solid oxide fuel cells and electrolysers

Chengsheng Ni [a], Jun Zhou [b], Ziye Zhang [a], Shuangbin Li [c], Jiupai Ni [a, d], Kai Wu [b] and John T.S. Irvine [a,c*]

a College of Environment and Resources, Southwest University, Beibei, Chongqing, 400715, People's Republic of China

b Center of Nanomaterials for Renewable Energy, State Key Laboratory of Electrical Insulation and Power Equipment, Xi'an Jiaotong University, Xi'an 710049, People's Republic of China

c School of Chemistry, University of St Andrews, Fife, Scotland, KY16 9ST

d National Base of International S&T Collaboration on Water Environmental Monitoring and Simulation in Three Gorges Reservoir Region, Chongqing 400716, China

**Email:J.T.S.I.: jtsi@st-andrews.ac.uk*

Abstract

A critical new research direction in solid oxide cells (SOCs) relates to balancing power grid or integrating energy interconnection with heat-electricity-gas simply by switching operations between fuel-cell and electrolyser mode. The rational design of robust and high-performance materials for SOCs is urgent for high conversion/energy efficiencies. Iron is highly abundant and offers suitable and flexible redox chemistry for the two operation modes. Iron-based oxide materials are widely investigated for SOCs because of the low cost and, more importantly, the appropriate valence stability of the Fe-O bond for excellent redox activity across a wide range of electrode functions. This review describes the progress in iron-based materials for SOCs, especially the recent applications in electrode materials or catalysts. The stable structure of the ferrite oxides provides an important platform for improved performance *via* the substitution of Fe in fuel electrodes of an SOC with H_2/H_2O or carbonaceous fuel/feedstock. Furthermore, we discuss nano-sized Fe^0 metal or alloys on an oxide electrode *via* infiltration and *in situ* exsolution aiming to fabricate highly active electrocatalysts. The advances of ferrite oxide-based oxygen

electrode are also discussed in terms of thermal expansion, stability and electrocatalysis before the development of symmetrical and reversible SOCs based on ferrite oxides are classified and summarized. Thereby, the challenges and future prospects are discussed.

Broad context

The aim of reducing greenhouse gas emissions (mainly CO_2) can be achieved by either improving conversion efficiency of fossil fuel or integrating renewable energies (such as solar and wind). However, these renewable energies are intermittent and do not always meet the timing of consumption unless a large-scale energy storage device is integrated into the grid. Solid oxide cells excelling at a highly efficient conversion between the electrical and chemical energies can increase both the efficiency of electricity production from fossil fuel and serve as an energy-storage device. As the polarization loss is crucially important in impeding the *to and fro* conversion, efficient and robust electrode materials are pursued to enable an excellent performance and long-term operation. Iron-based materials are promising candidates due to their optimum valency energy of Fe-O bonds in creating oxide-ion vacancies in both air and fuel conditions, compared to other transition-metal-based electrodes. Here, recent advances of iron-based electrode materials in metal/alloy or complex oxides were reviewed in terms of solid oxide fuel cells and electrolysers, as well as in reversible operation, with an emphasis on exploring critical understandings of hydrocarbon electrochemical oxidation or CO_2/H_2O reduction

1 Introduction

1.1 Fuel cells and electrolysers

Fuel cells are electrochemical devices that directly convert chemical energy in various fuels into electrical energy, promising power generation with high efficiency and low environmental impact [1, 2]. A typical solid oxide fuel cells (SOFCs) consists of three major components: a cathode and an anode separated by a solid oxide-ion (O^{2-}) or proton conducting electrolyte. SOFCs operated at 600-1000 ^{o}C where significant ion conduction in solids takes place are able to use carbonaceous fuel directly for energy conversion [3]. The use of carbonaceous fuel is advantageous in the commercialization as it does not need the overhaul of the current infrastructure to distribute high purity hydrogen[4, 5].

Although the fuel versatility of an SOFC allows for the use of natural gas, the decrease in greenhouse gas emissions to avoid uncontrollable climate changes requires the integration of renewable energies apart from fossil fuels[6, 7]. The coupling of an SOFC and solid oxide electrolyser cell (SOEC, jointly termed as solid oxide cells, SOC) is capable of long-term storage of the energy from the electricity generation from water/CO_2 splitting for H_2/CO as fuel stock [6, 8].

The state-of-the-art electrode materials for an SOC stack are Ni-YSZ cermet fuel and strontium lanthanum manganites (LSM) oxygen electrode [1, 3]. The electronic and ionic conductors are in separate phases of Ni-YSZ cermet or LSM-YSZ composite[9], but they can also merge in a mixed-ionic-and-electronic conductor (MIEC) as for expanded reaction sites [10]. Particularly, the recent advances iron-based electrode for both cathode and anode enable the purpose of a higher performance, better durability, and lower operation temperature of an SOC[11]. The low-cost iron based materials were found to be important in the metal support and oxide electrode along with the lowering temperature of an SOC [12]: Fe^0 in chromia-forming steel can act as support for electronic conductance, while ferrite oxides with MIEC can be used for reduced polarization in both cathode and anode. More importantly, the ferrite oxide that is more resistant to coking and reducing-oxidation (redox) cycle than Ni^0 was attractive in carbonaceous fuel oxidation and CO_2 electrolysis [4, 13, 14], which could linked to the Fe-O bond strength.

1.2 Thermodynamic considerations

1.2.1 Stability of 3d transition metals in reducing and oxidizing conditions

The development of anode materials for an SOFC using a carbonaceous fuel in the last decade has been focused on modified Ni(O) cermet [15] or alternative oxide electrodes [4, 16] to suppress the deposition of carbon [4, 14, 17]. Oxides of 3*d* transition metal (M) are popular choice for oxide anode because of their variable valency state allowing for electric and ionic conductivity. The selection of electrode for the fuel electrode is determined by the stability of the element in redox conditions. Although the formation of complex oxides will change the bond length and coordination, the redox stability of the oxides of transition metal is dependent on the bond strength of the cations with oxygen [18].

According to the Gibbs energy (ΔG) diagram of the oxides (Figure 1(a)) of Ti, V, Cr, Mn, Fe, Co, Ni, and Cu, the first four can maintain the oxide state under humidified H_2 (3% H_2O), while the others can be reduced to metal state. The stability of Fe/FeOx stands in a very peculiar position: FeO can be reduced to Fe^0 in 3% H_2O-H_2, but it can also maintain the oxide state if the steam is high, e.g. in 50% H_2O-50%H_2. The alloying of Fe with Ni^0, Cu^0, and Co^0 is advantageous in avoiding the sintering and growth of alloys in SOCs [19] partially because the regional or temporary high steam concentration would induce the formation of iron oxides.

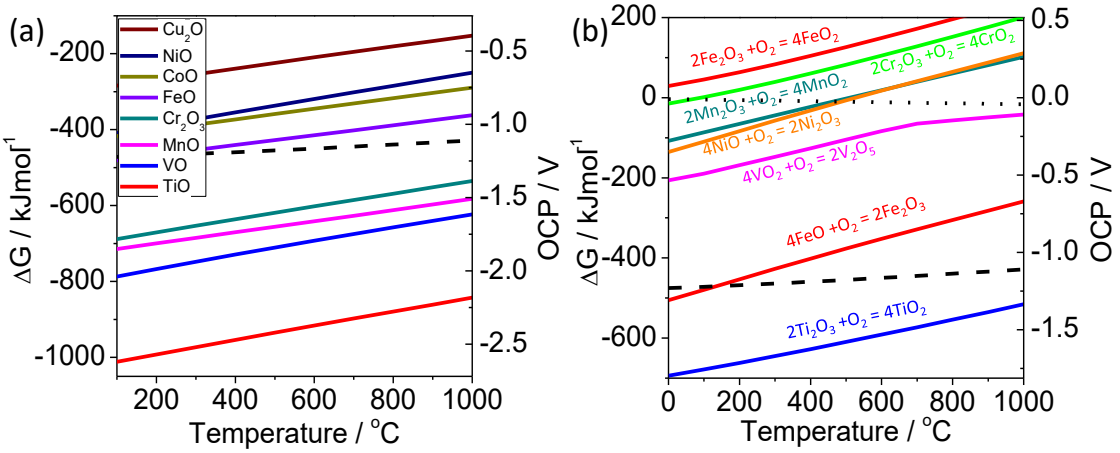

Figure 1. Gibbs energy (ΔG) for the selected 3*d* transition metals (M) in the reaction $xM + O_2$ (g) $= M_xO_2$ (a) or the selected redox reactions between oxides (b). The equilibrium

oxygen partial pressure was presented on the right *y* ordinate using the open circuit potential (OCP) of the oxygen pump against 1 bar O_2. The OCP of 3% H_2O-H_2 and air ($P(O_2)$= 0.21 atm.) against 1 bar O_2 was presented in dashed and dotted line, respectively, for comparison.

Stable chromites and titanates could be candidates for the fuel electrode, but a high-temperature reduction or intricate doping is required to produce oxygen vacancies for better electrocatalysis [20]. Because the equilibrium $P(O_2)$ of FeO/Fe is approaching that of 3% H_2O-H_2, as temperature decreases, a stable ferrite oxide can be achieved though the design of complex oxides with a lower ΔG and a decrease the activity of Fe cations. The multiple valence changing from V^{5+}, V^{4+}, V^{3+}, to V^{2+} makes the vanadates difficult to control and dramatic variation in crystal structure is implied.

For the application in oxygen electrode of an SOC, FeO_2, the oxygenated state of stable Fe_2O_3, can only be found at high pressure (76 GPa, Figure 1(b)) [21] at room temperature. Pyrite-structured FeO_2 with O-O bonds of 2.4~2.5 Å, shorter than the O-O bonds (2.72 Å) in $SrFeO_3$, indicating the spatial extension of the Fe 3*d* orbitals is the reason for the presence of Fe^{4+}/Fe^{3+} couple possible in the ambient air. These redox couples in Mn and Ni-based oxides provide the electric conductivity in oxidizing conductions, but the high-valence Fe^{4+}/Fe^{3+} and Co^{4+}/Co^{3+} redox couples could provide the MIEC.

1.2.2 Thermodynamics of perovskite with 3d transition metals

Perovskite oxides (with the formulae ABO_3) offer a large family of compounds along with several perovskite-related structures that are currently recognized and widely used in SOCs [16, 22-24]. The 3-D <BO> framework in the perovskite could be engineered to be a mixed-ion-and-electron (MIEC) conductor assisting the mobility of oxide ions and electrons/electron holes through the oxide-ion vacancies and B-O-B bonds, respectively[4, 14, 25].

Although FeO is found to be unstable in fuel condition of an SOFC, perovskite-type ferrites, *i.e.* $SrFeO_{3-\delta}$ (SFO) and $LaFeO_3$ (LFO), could be stabilized for oxide anode of an SOFC. The theoretical decomposition of a perovskite can be viewed in two steps and if LFO is taken as an example:

$LaFeO_3 = 1/2\ Fe_2O_3 + 1/2\ La_2O_3$ (1)

$1/2Fe_2O_3 = Fe^0 + 3/4\ O_2$ (2)

Combined the two reactions:

$LaFeO_3 = Fe^0 + 1/2Fe_2O_3 + 3/4O_2 + 1/2La_2O_3$ (3)

The enthalpy changes of reaction (1), ΔH^0(eq.1), is the negative value of the stabilization energy of a perovskite, Σ, that depends on the tolerance factor of the perovskite[26, 27] and ΔH^0(eq.2) characterizes the valence stability between Fe^{3+} and Fe^0. The superior stability of perovskite-type $LaFeO_3$ over Fe_2O_3/FeO could be explained by the stabilizing energy (Σ) that is dependent on the tolerance factor[18, 28], τ, of the final perovskite:

$$\tau = (R_A + R_B)/(\sqrt{2}(R_B + R_O)) \quad (4)$$

where R_A, R_B, and R_O represent the ionic radii of cation on A and B site, and oxide ion, respectively. Σ tends to increase when τ is approaching unity (Figure 2.). The Σ value is in the range of 60-80 kJ mol^{-1} if the τ is larger than 0.9.

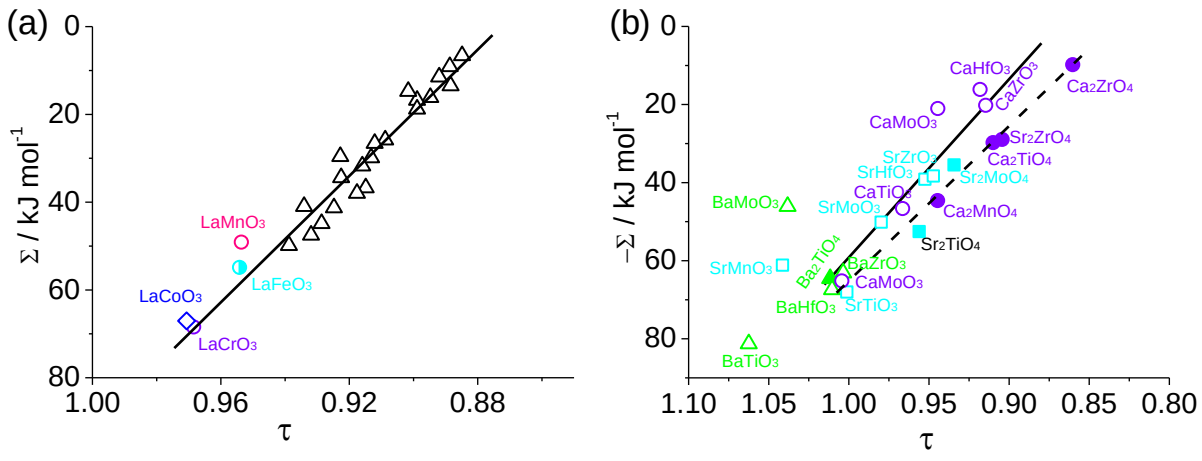

Figure 2. Stabilizing energy (Σ) per mole of oxygen as a function of tolerance factor (τ) for $A^{III}B^{III}O_3$ (a) and $A^{II}B^{IV}O_3$ (b) perovskites. The corresponding Σ for A_2BO_4 R-P phase in (b) is provided for comparison. Data were replotted from reference [28] and [18].

Comparing to the very stable perovskite $SrTiO_3$ and $LaCrO_3$, the lanthanum-based perovskites of Co, Mn, Ni, and Fe can be subjected to significant valence variation (e.g., Fe oxidation state from Fe^{4+}, Fe^{3+} to Fe^{2+} or even Fe^0) under a hydrogen atmosphere (Figure 3a). LFO is stable thermodynamically under a humidified H_2 (3% H_2O) without

decomposing to metallic iron and La_2O_3, but this does not guarantee that LFO can maintain the perovskite phase as the thermodynamic calculation is under the assumption of unity activity of solid phases (LFO and FeO)[29]. The stability of LFO is actually quite close to $Sr_2Fe_2O_5$ under reducing atmosphere (Figure 3a): both can survive in a reducing atmosphere of 10^{-20} bar at 850 °C [30]. $La_{0.6}Sr_{0.4}FeO_{3-\delta}$ started to decompose at a $P(O_2)$ lower than $10^{-20.5}$ bar (equivalent to 1.11 V vs 1 bar O_2) at 800 °C [31], but it underwent superficial decomposition at 600 °C in dry H_2 to produce Fe^0 nanorods and SrO [32].

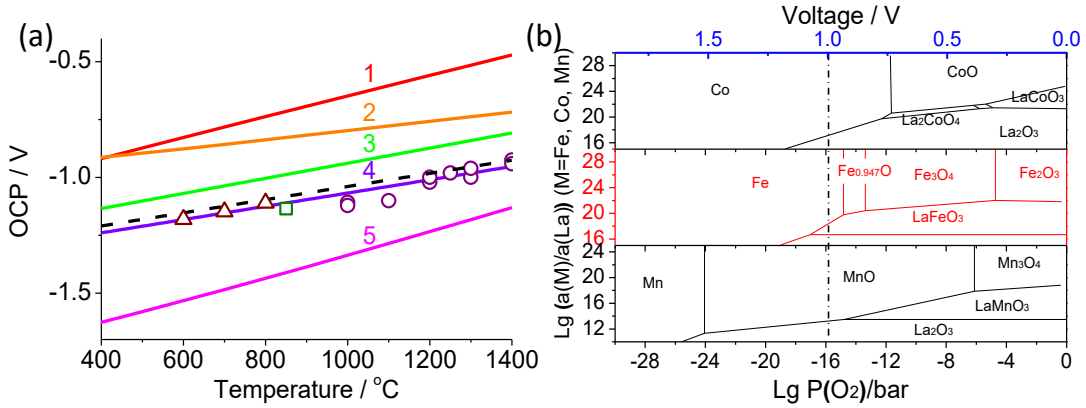

Figure 3. Theoretical OCP of the oxygen pump between 1 bar oxygen and the equilibrium oxygen pressure in different decomposition reactions: 1: $LaCoO_3$=1/2 La_2O_3 + CoO + 1/4O_2 [27]; 2: $LaMnO_3$ = 1/2 La_2O_3 + MnO + 1/4 O_2 [27]; 3: FeO = Fe + 1/2 O_2 [33]; 4: $LaFeO_3$ = 1/2 La_2O_3 + Fe + 3/4 O_2 [33]; 5: 2$LaCrO_3$ = La_2O_3+ 2Cr + 3/2O_2 [34]; the dashed line is the Nernst potential of 3% H_2O-H_2 against 1 bar O_2. The open marks are experimental decomposition data for LFO (circles[35, 36]) and $La_{0.6}Sr_{0.4}FeO_3$ (triangles[31]) and $Sr_2Fe_2O_5$ (square[30]). (b) Stability field of perovskites in the La-M-O (M=Fe, Mn, Co, Cr) systems at 1000 °C as a function of $P(O_2)$ (the corresponding EMF against 1 bar O_2) and the activity of cations on A and B site. (a) and (b) are modified and replotted from reference 29 and 27 respectively.

As it can be seen from the stability field (Figure 3b) in terms of $P(O_2)$, the activity of La^{3+} on A site and transition metal, M, on B-site, (Lg(a(M)/a(La)) is also important in determining the stability of the perovskite. This is the reason why A-site deficient perovskite is usually employed to increase the exsolution of metals from B site *via* the increase of the activity of transition cations [37-43]. The development of stable R-P phase

with A-site element excess could be explained by the decrease of activity of cations on B site and the increased Σ comparing with the parent perovskite (Figure 2b).

$SrFeO_3$ contains iron in an unusual Fe^{4+} oxidation state should be considered to result from the interplay of Fe 3*d* electrons and O *p* holes [44], providing significant oxygen non-stoichiometry for MIEC for excellent oxygen reduction or oxidation evolution as oxygen electrode[44]. The Fe^{4+} can be reduced to Fe^{3+} even by the thermal treatment in air: *e.g.* SFO is reduced to $SrFeO_{2.675}$ at 800 ^oC under a $P(O_2)$ of 0.21 bar as a result of oxygen loss from the lattice [45, 46].

The analyses of thermodynamics indicate that Fe-based materials boast a great versatility in the metal/oxide fuel electrode and oxygen electrode. The characteristics of increased stability in fuel condition with a lowering of temperature and the possible mixed electron and oxide-ion conductivity of Fe-based materials were in line with the development of intermediate- and low-temperature SOCs, which makes them popular choice in the last decades.

1.3 Objective and organization of the review

The maturity of SOCs for efficient electricity generation from chemical energy or chemical synthesis from electricity requires low-cost, highly stable and enhanced electrocatalytic electrode materials to reduce the cost in construction and operation. There are quite a few excellent reviews on the development for SOFC or SOEC in terms of materials [15, 16, 47, 48], microstructure [49, 50], interface [10, 51, 52] and systems[53, 54].

As the second most abundant metal element in the Earth's crust, iron has been selected to prepare highly conductive and light-weight support, efficient nanoscale catalyst with a high selectivity, redox-stable oxide electrode for symmetrical and reversible SOCs. In the context of extensive research in the last decade, we aim to provide a comprehensive review of the Fe-based materials for SOCs. In the meantime, the infiltration and exsolution into or from Fe-based electrodes are highlighted for the development of advanced electrodes for SOCs. The advancement of symmetrical and reversible SOCs for energy storage was summarized.

Iron-based materials have been used in the development of both anode (*section 2*) of an SOFC and cathode (*section 3*) of an SOEC for the fuel oxidation or feedstock reduction, respectively. The strategies of balancing the stability and performance for fuel electrode have been reviewed in terms of the thermodynamics and practical demonstrations. As one important family of materials for the cobalt-free oxygen electrode, ferrite based perovskite (*section 4*) was reviewed as oxygen electrode before we move to the construction of symmetrical and reversible SOCs (*section 5*).

2 Iron-based anodes for SOFCs

As the most abundant transition metal in the earth crust, Fe has been incorporated into the construction of SOFCs due to the low cost, stable metal/oxide reversibility and great mechanic strength at the oxygen potential of fuel and selective catalysis supporting fuel conversion. These advantages are very important to the commoditization and fuel versatility of an SOFC, and Fe can be included in the anode in the forms of *metal alloy support* (section 2.1), *oxide anode* (section 2.2) for the utilization of H_2 or carbonaceous fuel and *nano-sized catalysts* (section 2.3) on the surface of non-ferrite support to enhance the electrocatalysis for the FOR. Infiltration/exsolution [37-43, 50, 55] are popular methods to enhance the performance of the anode either to increase the fuel adsorption/dissociation and electronic/ionic conduction. The structure of this section is graphically present in Figure 4.

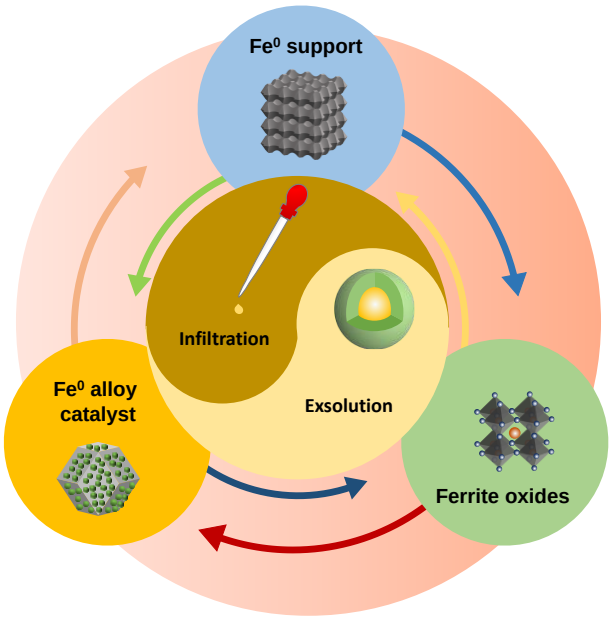

Figure 4. Relationship between different types of Fe-based materials and processing.

2.1 Iron-based alloys

Ferritic stainless steels have been used for interconnects of an SOFC operating at 600-800 ^{o}C due to the abundance, low-cost, high electric conductivity and high machinability, and it is beneficial for the construction of light-weight SOFC stacks[56-59]. High Cr content (> 22 wt.%) ferritic stainless steels, such as Crofer 22 APU, ZMG 232 or E-BRITE, were designed for the operating temperature at 800 ^{o}C to avoid the rapid growth of oxidation scale *via* the formation of dense protective chromia layer, but lower Cr content ones (16–20%) that are less prone to embrittlement by σ-FeCr phase formation could be used for SOFCs operated at temperatures below 800 ^{o}C to reduce the cost and increase the workability[60].

Analogous to the advantages of stainless steel over ceramic interconnect, metal-supported SOFCs provide significant advantages over conventional ceramic cells, including low cost, mechanical ruggedness, and tolerance to rapid thermal and redox cycling [61]. With the development of metal-supported SOFCs, porous stainless steel (Figure 5) has been used for either anode or cathode support due to its high conductivity in both air and reducing atmosphere [62]. However, with near-to-none ionic conductivity, high sinterability and tendency towards formation of superficial chromia, infiltration of ionic conductors, mixing with oxides for cermet for functional layer and depositing dense oxide coatings to inhibit corrosion have been explored for the practical uses of these metals for electrode and interconnects in solid oxide fuel cells [63]. The infiltrated materials could be ionic conductors or metal/oxide electrocatalysts for either oxygen or fuel electrode. With Ni-GDC and $SmBa_{0.5}Sr_{0.5}Co_2O_5$ infiltration into either layers of porous 430L stainless steel sandwiching 15-μm scandia-stabilized zirconia (SSZ) electrolyte, a remarkable performance of 1.02 W cm^{-2} has been achieved at 650 ^{o}C [62].

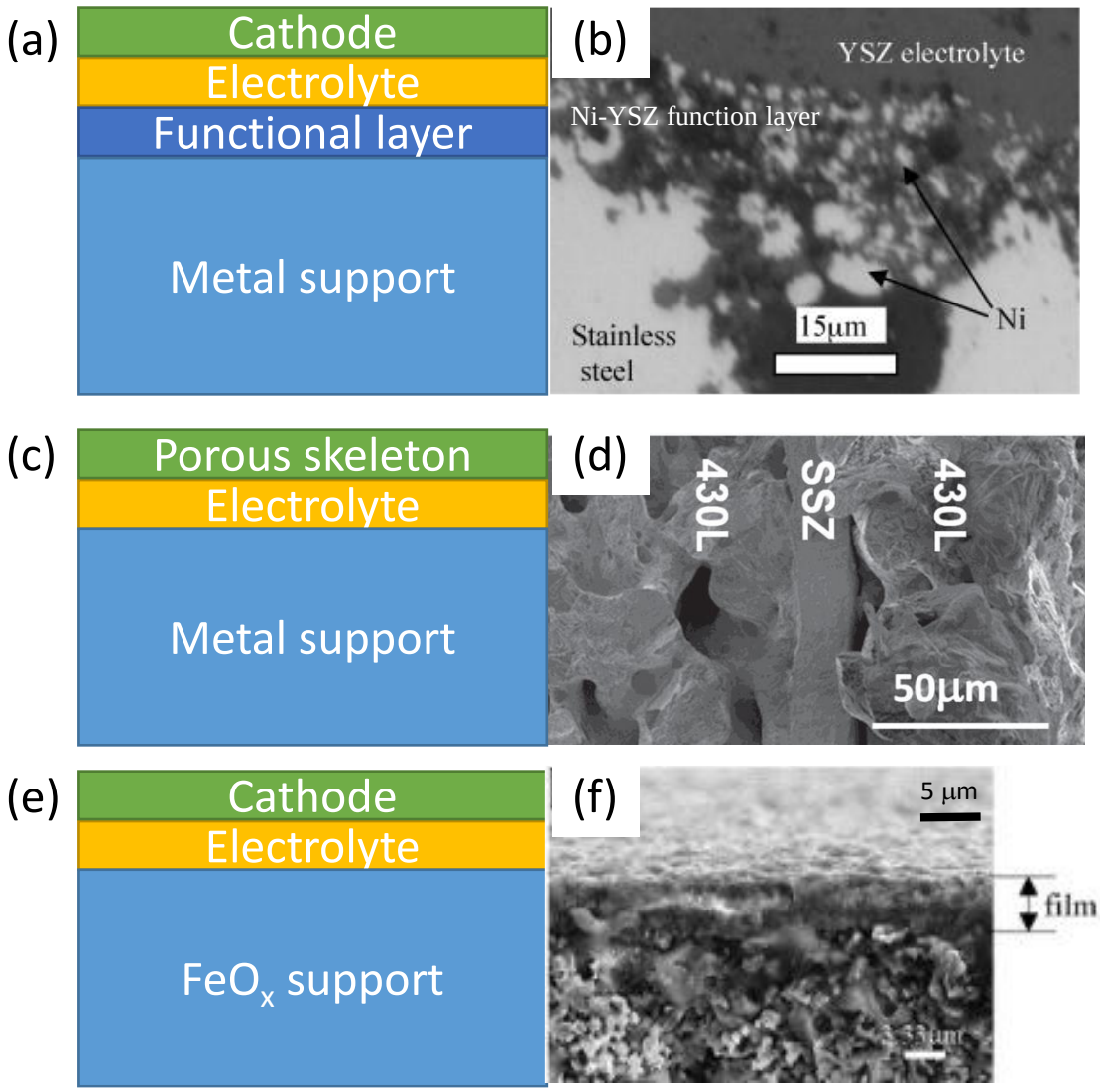

Figure 5. Typical configurations of Fe-metal supported SOFC with functional layer [64] (a,b), infiltrated electrodes [62] (c,d) and FeO_x oxide precursors [65] (e,f). (b), (f) are taken from reference 64 and 65, respectively. Copyright Elsevier. Image (d) were taken from reference [62]. Copyright Wiley-VCH.

Stainless-steel supported SOFCs are generally processed under an inert or reducing gas to avoid the oxidation of steel at the high temperature for the densification of the ceramic electrolyte[66], but, alternatively, the metal support can be obtained from the oxide precursor along with the *in-operando* reduction under hydrogen (Figure 5c)[67]. The conventional Ni-YSZ cermet anode has been achieved through the co-sintering of NiO/YSZ composite with the YSZ electrolyte at a temperature around 1400 °C and the *in situ*

reduction of the oxide precursor can cause the loss of oxygen and increase the porosity of the anode for gas transport, but the incorporation of FeO_x into the NiO in the cermet would be difficult to survive the co-sintering with YSZ due to the reactivity of FeO_x with the zirconia-based electrolyte. Virkar *et al.*[68] developed the idea of incorporation of iron in the anode support to reduce the cost of the anode substrate and a high content of iron (Fe_2O_3:NiO =3:7 in molar ratio) was incorporated and a cell showing a power density of $\sim$ 180 $mWcm^{-2}$ at 550 ^oC was achieved if GDC and NiO-GDC (50:50 wt.%) were used as the electrolyte and functional layer, respectively.

The reactivity of binary oxides with LSGM is in the order of Co_2O_3>NiO>Fe_2O_3 for the production of La-containing oxides at 1150 ^oC [69]. Ni-Fe(O)-based anode without mixing with ionic conductors has been developed initially to reduce the reactivity of the conventional Ni(O) anode with the LSGM electrolyte that produces insulating phases blocking the reaction sites[65, 70]. A Ni-Fe(O)-SDC composite with a thin GDC buffer layer was used as the cermet support for the deposition of LSGM electrolyte through the pulsed laser deposition (PLD) and high performance of 2 Wcm^{-2} was achieved at 600 ^oC [65]. With the low concentration of iron (10 wt.% Fe_2O_3) in NiO, an Fe-Ni alloy was achieved under reduction condition at 700 ^oC for one hour and the area-specific resistance (ASR) of the cell was limited by the cathode and ohmic resistance of the electrolyte at high and low temperatures, respectively[70]. Cu-Fe-Ni nano alloy particles consisting of immiscible face-centered cubic Cu- and body-centered cubic Fe-based phases were obtained by reducing the Cu(Ni)Fe_2O_4 spinel precursor for an efficient anode at temperatures between 800 and 600 ^oC [67].

The interaction between the steel support and the superficial catalysts and ionic conductors is crucial to understanding the durability of the cell. A layer of $CeFeO_3$ was found on the top of the chromia layer (Figure 6) under operated in H_2 condition at 650 ^oC if GDC/Ni has been infiltrated on to the surface of the Fe-Cr alloy (Fe-22 wt. % Cr-0.4% Mn)[66, 71]. $CeFeO_3$ is unstable in the ambient air, showing CeO_2 impurities even at a low temperature[72], and the magnetic measurement and Mössbauer spectra both showed that the cation valencies in single-phase $CeFeO_3$ are Ce^{3+} and Fe^{3+} [73]. The formation of $CeFeO_3$

acts as a protective layer to inhibit the growth of underneath chromia layer, similar to the proposed $CeCrO_3$ layer in ceria infiltrated metal support in reducing condition[63].

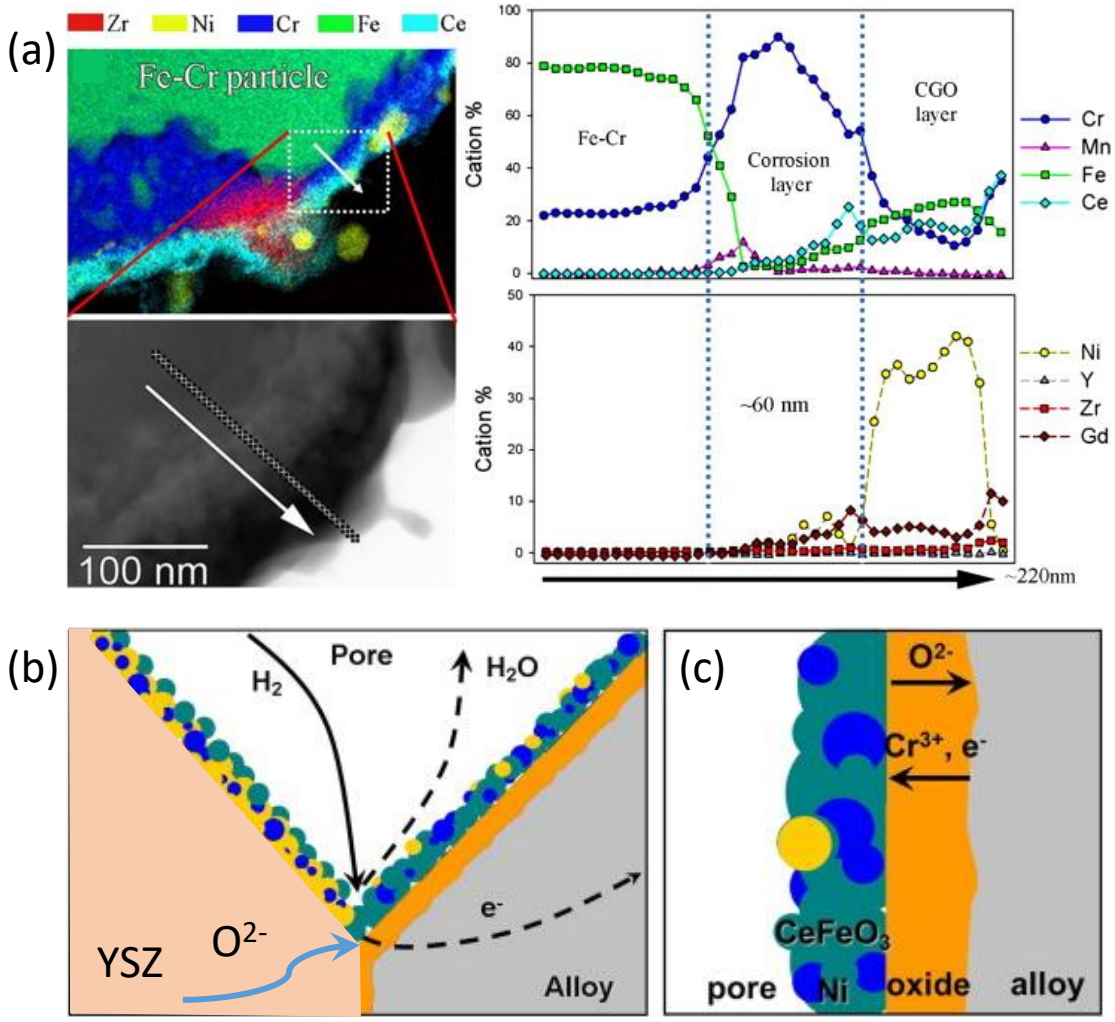

Figure 6 (a) TEM images and EDS line scan of a Fe-Cr anode with GDC and Ni infiltration after an operation under a bias between 0.7-0.8 V for 120 hours. (b) Schematics illustrating the O^{2-} and H_2 transport to the TPB and the H_2O and electron transport away from the TPB. (c) Schematics of the O^{2-}, Cr^{3+} and e^- transport through the Cr_2O_3 layer under OCV conditions. Symbols in (c): yellow – CGO, blue – Ni, green – $CeFeO_3$, orange – Cr_2O_3 [66]. Image are taken from reference 66. Copyright Elsevier.

2.2 Ferrite-oxide anode

The comparable stability of SFO and LFO against the fuel condition indicates that the partial substitution for $Fe^{4+/3+}$ could be more meaningful in stabilizing the oxides by maintaining the oxygen content in the perovskite lattice and decreasing the activity of

$Fe^{3+/2+}$ than A-site doping. Cr^{3+}, Ti^{4+}, Nb^{5+}, W^{6+}, and Mo^{6+} in perovskite-type ferrite which are the most popular cations used for the synthesis of a stable oxide anode in a reducing atmosphere (Table 1), while the ferrites with Ni^{2+}, Cu^{2+}, and $Co^{2+/3+}$ substitution tend to destabilize the structure and induce the formation of layered perovskite during the fuel cell operation. An investigation into the literature on stabilizing the ferrite perovskite with stable cations indicated that a substitution level around 20% was sufficient to achieve a stable perovskite at 800 °C in H_2. The $La_{0.30}Sr_{0.70}Fe_{0.70}Cr_{0.30}O_{3-\delta}$ perovskite was shown to be stable down to a $P(O_2)$ of 10^{-20} atm. at 800 °C and a $P(O_2)$ of 10^{-18} atm. at 900 °C. Further reduction at lower $P(O_2)$ led to the formation of Fe^0, but the phase separation was also shown to be completely reversible with an increase in the partial oxygen pressure and re-oxidation of the sample [74]. The substitution of $Mn^{4+/3+/2+}$ for $Fe^{3+/4+}$ in a perovskite could be conditional as Mn^{2+} is more stable than Fe^{2+} to be reduced to metal, but Mn^{3+} is less stable than Fe^{3+} in the production of divalent cations. Ishihara *et al.* [75, 76] found that $La_{0.6}Sr_{0.4}Fe_{0.9}Mn_{0.1}O_3$ maintained the perovskite phase after the fuel cell testing at 800 °C, but the further increase of the Mn content as in $La_{0.6}Sr_{0.4}Mn_{0.2}Fe_{0.8}O_{3-\delta}$ induced the formation of R-P phase $La_{1.2}Sr_{0.8}Mn_{0.4}Fe_{0.6}O_4$ and Fe^0 particles on the surface [77]. Since the doping on B site is more important in stabilizing the perovskite lattice, we select the most popular Mo, Cr and Ti doping as examples to represent the progress in ferrite anodes.

Table 1. Research work on the Fe-based oxide anode for SOFCs.

Cell configuration [a] Anode|buffer|electrolyte(μm)|buffer|cathode	σ in H_2 Scm^{-1}	R_p [b] Ωcm^2	Performance $mWcm^{-2}$	Final Phase	Ref
$Sm_{0.5}Sr_{0.5}FeO_{3-\delta}$/GDC|GDC|YSZ(400)|GDC|&	0.19@750 °C	0.91@750 °C	201@750° C	R-P+Fe	78
$Sm_{0.95}Ce_{0.05}FeO_{3-\delta}$|YSZ(700)|&	0.40@800 °C	0.08@800 °C	130@800° C	Per	79
$Ce_{0.2}Sr_{0.8}Fe_{0.95}Ru_{0.05}O_{3-\delta}$|LSGM(320)|&	0.70@800 °C	0.10@800 °C	482@800° C	Per+CeO_2	13

Pd	$La_{0.6}Sr_{0.4}Fe_{0.95}Pd_{0.05}O_{3-\delta}$/GDC|LSGM(300)|&	-	-	350@750°C	R-P+Pd	80
	$LaCo_{0.3}Fe_{0.67}Pd_{0.03}O_{3-\delta}$|SDC(300)|&	-	0.02@800°C	650@750°C	Per+Pd	81
	$La_{0.6}Sr_{0.4}Fe_{0.9}Pd_{0.1}O_{3-\delta}$|LSGM(350)|&	~0.10@750°C	1.0@750°C	370@750°C	Per+Pd	82
Ru	$Ce_{0.2}Sr_{0.8}Fe_{0.95}Ru_{0.05}O_{3-\delta}$|LSGM(320)|&	0.78@800°C	0. 08@800°C	0.80@800°C	Per+Ru + SrO+CeO_2	13
	$(Pr_{0.5}Sr_{0.5})_{0.9}Fe_{0.8}Ru_{0.1}Nb_{0.1}O_{3-\delta}$|LSGM(~ 300 μm)|LSCF/GDC		0.08@800°C	0.683@800°C	Per +Ru	83
Ni	$PrNi_{0.4}Fe_{0.6}O_{3-\delta}$|LSGM(30)|&	-	-	663@800°C in CH_4	R-P+Fe	84
	$La_{0.6}Ca_{0.4}Fe_{0.8}Ni_{0.2}O_{3-\delta}$|SDC(300)|&	-	-	350@800°C	Per+Ni	85
	$La_{0.6}Ca_{0.4}Fe_{0.8}Ni_{0.2}O_{3-\delta}$/SDC|SDC(280)|&	-	0.15@800°C	303@800°C	Per+ $FeNi_3$	86
	$La_{0.6}Ce_{0.1}Sr_{0.3}Fe_{0.9}Ni_{0.1}O_{3-\delta}$|LSGM(30)|&	0.45@800°C	0.12@850°C	900@850°C	R-P+Per+ NiFe	87
	$Sr_2FeMo_{0.65}Ni_{0.35}O_{6-\delta}$|LDC|LSGM(300)|LSCF	65@800°C	0.16@800°C	792@800°C 500@850° CinCH4	R-P+Fe- Ni	88
	$La_{0.7}Sr_{0.3}Cr_{0.85}Ni_{0.1125}Fe_{0.0375}O_{3-\delta}$|YSZ (100)|LSM	10@800°C	0.20@800°C5000ppmH_2S–H_2	580@800°C	Per+ Ni- Fe	89

Cu	$La_{0.5}Sr_{0.5}Fe_{0.8}Cu_{0.2}O_{3-\delta}$|SSZ(230)|&	-	0.20@800 °C	577@800° C	R-P+Per+Cu	90
Co	$PrBaFe_{2-x}Co_xO_{5+\delta}$(x=0,0.2)|LSGM|&	1.0@800° C	0.25@800 °C	735@850° C	R-P+ Co_3Fe_7	91
	$Pr_{0.4}Sr_{0.6}Co_{0.2}Fe_{0.7}Nb_{0.1}O_{3-\delta}$|LSGM(~300)|LDC| $Ba_{0.9}Co_{0.7}Fe_{0.2}Nb_{0.1}O_{3+\delta}$	15.3@800 °C	-	900@800° C	Per+ Co- Fe	92
	$Pr_{0.4}Sr_{0.6}Co_{0.2}Fe_{0.7}Nb_{0.1}O_{3-\delta}$|LSGM(300)| $Ba_{0.9}Co_{0.7}Fe_{0.2}Nb_{0.1}O_{3+\delta}$	-	-	1150@800 °C 910@800° C in C_3H_8	R-P+Co- Fe	93
	$La_{0.5}Sr_{0.5}Co_{0.45}Fe_{0.45}Nb_{0.1}O_{3-\delta}$|LSGM(~300)|&	1.8@750° Cor800°C	0.45@750 °C;0.3@800°C	-	Per+Co-Fe	94
Mn	$La_{0.6}Sr_{0.4}Mn_{0.2}Fe_{0.8}O_3$/GDC|LSGM(280)|&	2.8@800° C	0.42@800 °C	720@800° C	R-P+Fe	77
Nb	$La_{0.9}Ca_{0.1}Fe_{0.9}Nb_{0.1}O_{3-\delta}$|SSZ|LSM/YSZ	-	0.40@800 °C	610@800° C	Per	95
	$Pr_{0.95}Ba_{0.95}(Fe_{0.9}Nb_{0.1})_2O_{5+\delta}$|SDC|LSGM(450)| $PrBaCo_2O_{5+\delta}$	-	-	1050@800 °C 640 @800 °C in CH_4	Per	96
	$(La_{0.6}Sr_{0.4})_{0.9}Co_{0.2}Fe_{0.6}NbO_{3-\delta}$|SDC|LSGM(200)|&	0.59@800 °C	0.382@800°C	593@800° C	Per	97
	$La_{0.5}Sr_{0.5}Fe_{0.9}Nb_{0.1}O_{3-\delta}$|LSGM(~300)|&	0.40@800 °C	0.18 @800 °C	1000 @850 °C	R-P+Fe	98
	$La_{0.4}Sr_{0.6}Co_{0.2}Fe_{0.7}Nb_{0.1}O_{3-\delta}$/GDC|YSZ|&	-	-	348@850° C	-	99

	$Pr_{0.44}Sr_{0.6}Co_{0.2}Fe_{0.7}Nb_{0.1}O_{3-\delta}$|LSGM(265)|&	-	0.2@800°C	972@900°C	-	100
	$La_{0.4}Sr_{0.6}Co_{0.2}Fe_{0.7}Nb_{0.1}O_{3-\delta}$|GDC|YSZ(200)|GDC&	-	0.25@850°C	395@850°C	-	102
	$La_{0.9}Ca_{0.1}Fe_{0.9}Nb_{0.1}O_{3-\delta}$|SSZ(60)|	-	0.12@850°C	392@850°C	Per	103
	$Sr_{1.9}FeNb_{0.9}Mo_{0.1}O_{6-\delta}$|LSGM(200)|&	8.8@850°C	0.35@800°C	833@800°C 150@800° C in CH_4 with Pd	Per	104
Ga	$La_{0.7}Sr_{0.3}Fe_{0.7}Ga_{0.3}O_{3-\delta}$|LSGM(320)|&	0.42@800°C		489@800°C	Per	105
Ti	$La_{0.3}Sr_{0.7}Ti_{0.3}Fe_{0.7}O_{3-\delta}$|SSZ|LSM/SSZ	low	0.18@800°C	401@800°C	Per	106
	$Y_{0.08}Sr_{0.92}Ti_{0.6}Fe_{0.4}O_{3-\delta}$|YSZ(85)|LSF/YSZ	0.10@800°C	~0.46@800°C	321@800°C Pd/CeO_2	Per	108
	$La_{0.3}Sr_{0.7}Ti_{0.3}Fe_{0.7}O_{3-\delta}$|YSZ(400)|&	-	0.18@900°C	374@900°C	-	109
	$Sm_{0.8}Sr_{0.2}Fe_{0.8}Ti_{0.15}Ru_{0.05}O_{3-\delta}$|GDC|&	1.0@800°C	0.12@800°C	271@800°C	Per+Ru	110
	$Sm_{0.9}Sr_{0.1}Fe_{0.9}Ru_{0.1}O_{3-\delta}$|SDC(600)|&	-	0.24@800°C	119	Per+Ru	111
	$Sr_{0.98}Fe_{0.8}Ti_{0.2}O_{3-\delta}$|LSGM(300)|&	low	0.18@800	700@800°C	Per	112
	$Sr_{0.95}(Ti_{0.3}Fe_{0.63}Ni_{0.07})O_{3-\delta}$|LSGM(300)|LSCF		0.081@800°C.	950@800°C	Per+Fe Ni	113

	$SrTi_{0.3}Fe_{0.7}O_{3-\delta}$/GDC|LSGM(300)|LSCF	0.10@800 °C	0.17@800 °C	337@800° C	-	114
	$La_{0.3}Sr_{0.7}Fe_{0.7}Ti_{0.3}O_{3-\delta}$|SDC|YSZ(500)|LSM/YSZ		1.45@800 °C	162@800° C	Per	115
	$La_{0.95}Fe_{0.8}Ni_{0.05}Ti_{0.15}O_{3-\delta}$|LSGM(300)| $La_{0.8}Sr_{0.2}CoO_{3-\delta}$	100@800° C	0.32@800 °C	280@800° C; 600@800° Cwithceria	Per+Ni	29
	$La_{0.7}Sr_{0.3}Ti_{0.1}Fe_{0.6}Ni_{0.3}O_{3-\delta}$|LDC|LSGM(400)|&	1.1@800° C	0.20@800 °C	402@800° C	Per	116
	$Sr(Ti_{0.3}Fe_{0.7}Ru_{0.07})O_{3-\delta}$|LSGM(300)|LSCF/GDC	-	0.22@750 oC	350@700° C	Per+Ru	117
Cr	$LaSr_2Fe_2CrO_{9-\delta}$|LDC|LSGM(440)|LSCF	-	0.22@800 °C	>400@800 °C	Per	118
	$LaSr_2Fe_2CrO_{9-\delta}$ |LSGM(50)|&	0.17@800 °C	0.55@800 °C	224@800° C	Per	119
	$La_{0.75}Sr_{0.25}Cr_{0.5}Fe_{0.5}O_{3-\delta}$|YSZ|&	0.21@900 °C	1.15@850 °C	-	Per	120
	$La_{0.75}Sr_{0.25}Cr_{0.5}Fe_{0.5}O_{3-\delta}$|LSGM(1500)|&	-	0.2@800° C	35@800°C	Per	121
	$La_{0.7}Sr_{0.3}Cr_{0.5}Fe_{0.5}O_{3-\delta}$|YSZ(300)|LSM	-	1.4@800° C insyngas		Per	122
	$La_{0.65}Sr_{0.3}Ce_{0.05}Cr_{0.5}Fe_{0.5}O_{3-\delta}$|YSZ(300)|LSM	-	0.25@800 °C insyngas	270@800° Cinsyngas	Per	122

	$La_{0.75}Sr_{0.25}Fe_{0.5}Cr_{0.5}O_{3-\delta}$/SDC|LSGM(300)|LSCF/SDC	0.07@800 °C	0.8@800° C	390@800° C 240@800° Cin syngas	Per	1 2 3
	$La_{0.65}Bi_{0.1}Sr_{0.25}Fe_{0.5}Cr_{0.5}O_{3-\delta}$/SDC|LSGM(300)|LSCF/SDC	0.14@800 °C	0.32@800 °C	550@800° C 360@800° Cinsyngas	Per	123
Sc	$La_{0.6}Sr_{0.4}Fe_{0.9}Sc_{0.1}O_{3-\delta}$|LSGM(18)|&	0.69at800° C.	0.29@800 °C.	560@800° C	Per+R-P	1 2 4
Mo	Ba_2FeMoO_6|SDC|LSGM(300)|$SrCo_{0.8}Fe_{0.2}O_{3-\delta}$	196@850° C	0.73@800 °C	398@800° C	Per	125
	$Sr_{1.6}K_{0.4}FeMoO_{6-\delta}$|LDC|LSGM(300)|LDC| $Sr_{0.9}K_{0.1}FeO_{3-\delta}$	>400@800 °C		973@850° C	-	126
	$Sr_2FeMo_{0.8}Nb_{0.2}O_{6-\delta}$|LSGM(200)|$PrBaCo_2O_{5+\delta}$	5.3@800° C	0.1@800° C	520@800° C 380inCH_4	Per	127
	Stainlesssteel/$SrFe_{0.75}Mo_{0.25}O_{3-\delta}$|YSZ(18)|&	-	0.16@750 °C	740@800° C	Per	128
	$Sr_2Fe_{1.5}Mo_{0.5}O_{6-\delta}$|LSGM(265)|&	310@780° C	0.27@800 °C	500@800° C	Per	129
	$Sr_{1.75}Ca_{0.25}Fe_{1.5}Mo_{0.5}O_{3-\delta}$|LSGM(430)|&	93.1@800 °C	0.20@800 °C	709@800° C	Per	130
	$Sr_2TiFe_{0.8}Mo_{0.2}O_{6-\delta}$ |LSGM(200)|&	2.0@850° C	0.55@800 °C	573@850	Per	131
	$Sr_2Fe_{1.5}Mo_{0.5}O_{6-\delta}$|LSGM(15)|&		0.22@800 °C	970@800° C	Per	1 3 2

	$Sr_{1.8}La_{0.2}FeMoO_{6-\delta}$|GDC|YSZ(300)|LSCF	500@800°C	0.30@800°C	885@800°C	Per	133
	$Sr_2Fe_{1.4}Nb_{0.1}Mo_{0.5}O_{6-\delta-\delta}$|LSGM(243)|&	25@800°C	0.09@800°C	364@800°C		134
	$Pr_{0.95}Ba_{0.95}Fe_{1.9-x}Ni_xMo_{0.1}O_{6-\delta}$(x=0.1-0.4)/SDC|SDC(200)|LSCF/SDC	8@800°C	0.06@700°C	450@750°C	Per+Ni_3Fe	135
	$La_{0.5}Sr_{0.5}Fe_{0.9}Mo_{0.1}O_{3-\delta}$|SDC|LSGM(280)|$Ba_{0.6}Sr_{0.4}Co_{0.9}Nb_{0.1}O_{3-\delta}$	16@800°C	-	722@800°C 513 in CH_4	Per	136
	$Pr_{0.4}Sr_{0.6}(Co_{0.2}Fe_{0.8})_{0.95}Mo_{0.05}O_{3-\delta}$|LSGM(293)|&		0.4@850°C	493@850°C	Oxide+CoFe	137
	$La_{0.6}Sr_{0.4}Co_{0.2}Fe_{0.7}Mo_{0.1}O_{3-\delta}$|LSGM(270)|&	2.5@850°C	0.23@850°C	929@850°C	-	138
Zr	$BaFe_{0.9}Zr_{0.1}O_{3-\delta}$/GDC|LSGM(200)|&	0.01@800°C	0.06@750°C	1097@800°C	Per	139
	$SrFe_{0.75}Zr_{0.25}O_{3-\delta}$/GDC|LSGM(~400)|&	~0.5@800°C	0.06@750°C	425@800°C	Per	140
W	$SrFe_{0.8}Zr_{0.2}O_{3-\delta}$|LSGM(~300)|&	1.16@850°C	0.2@750°C	580@800°C		141
	$SrFe_{0.8}Zr_{0.2}O_{3-\delta}$|SDC(~200)|&			190@750°C		142
	$MnFeCrO_4$|YSZ|&	~0.4@850°C	4.15@850°C	-	stable	143
	$Fe_{0.5}Mg_{0.25}Ti_{0.25}Nb_{0.9}Mo_{0.1}O_{4-\delta}$|GDC|&	0.29@750°C	12@700°C	-	stable	144

a: "&" indicates the cathode is identical to anode and "/" indicates the mixture. "R-P" and "Per" refers to R-P phase and perovskite, respectively. b: Polarization resistance in wet H_2 unless specified. "LSCF"and LDC represents $La_{0.6}Sr_{0.4}Co_{0.2}Fe_{0.8}O_{3-\delta}$ and $La_{0.4}Ce_{0.6}O_{2-\delta}$, respectively.

Mo doping: Mo doped SFO is well studied as the anode of an SOFC because of its high conductivity in reducing atmosphere, superior stability and electrocatalysis towards the FOR. $SrFe_{1-x}Mo_xO_{3-\delta}$ ($0 \leqslant x \leqslant 0.25$) is fairly stable in air as the Mo and Fe valence are mostly 6+ and 3+ in $SrFe_{0.75}Mo_{0.25}O_3$, but the further increase of x requires a reducing atmosphere for single-phase perovskite [145]. $SrMo^{IV}O_3$ is a cubic perovskite at room temperature with a cell parameter 3.976 Å, [146] close to that of SFO, 3.855 Å, but the maximum substitution of Mo on Fe site achieved so far was $Sr_2Fe_{0.4}Mo_{1.6}O_6$ *via* the reduction in H_2 [147]. $SrFe_{1-x}Mo_xO_3$ ($0.25 \leqslant x \leqslant 0.6$) with Fe and Mo cations ordering as in a typical double perovskite Sr_2FeMoO_6 could be used as an oxide anode for SOFC[148]. The redox couple $Fe^{2+} + Mo^{6+} \leftrightarrow Fe^{3+} + Mo^{5+}$ is expected to generate electronic carriers, as well as oxygen vacancies into the lattice for oxide-ion conduction[149]. $Sr_{2-x}La_xFeMoO_{6-\delta}$ ($0 \leqslant x \leqslant 1$) with La^{3+} doping in Sr_2FeMoO_6 can increase the cation disordering, oxygen vacancy and Mo^{4+} formation[133]. Ni doping in SMFO generally destabilizes the structure: $Sr_2Fe_{1.5-x}Ni_xMo_{0.5}O_{6-\delta}$ was stable under H_2 at 750 ^oC when x= 0.05 and 0.10, but Ni^0 was shown on the surface when x=0.2 and 0.3 [150]. The reduction of $Sr_2FeMo_{0.65}Ni_{0.35}O_{6-\delta}$ in H_2 at 850 ^oC produced R-P type $Sr_3FeMoO_{7-\delta}$ and Fe-Ni alloy [88]. A-site deficiency also promoted the exsolution of Ni particles in the Ni/Mo co-doped SFO: $Sr_{2-x}Fe_{1.4}Ni_{0.1}Mo_{0.5}O_{6-\delta}$ (x = 0, 0.025, 0.05, 0.075, 0.1) exhibited a thermal stability in reducing atmosphere at 750 °C, though some nickel particles were exsolved on the surface at 800 °C for x = 0-0.075. The cell with these oxide anodes delivered a peak power density of 326, 438, 606, 407 and 348 mW cm^{-2} at 800 °C with humidified H_2 as the fuel when x = 0, 0.025, 0.05, 0.075, 0.1, respectively[151]. $Sr_2Fe_{1.5}Mo_{0.5}O_6$ with GDC composite showed the best performance when it was mixed with 40 wt.% GDC[152]. Infiltration of $Sr_2Fe_{1.5}Mo_{0.5}O_6$ into a porous-dense-porous LSGM scaffold was used to prepare a

symmetrical SOFC and a maximum power density 880 mW cm^{-2} at 700 °C and 306 mW cm^{-2} at 900 °C was obtained under H_2 and CH_4 fuel, respectively[153]. The anode performance of $A_2FeMoO_{6-\delta}$ (A=Ca, Sr, Ba) with variable A-site cation was in the sequence $Ca_2FeMoO_{6-\delta}$ < $Ba_2FeMoO_{6-\delta}$ < $Sr_2FeMoO_{6-\delta}$ and, specifically, $Ca_2FeMoO_{6-\delta}$ was found to be unstable even in a nitrogen atmosphere [154].

Cr doping: The $3d^54S^1$ valence electron of Cr indicates that Cr^{6+} is achievable as in CrO_3 or $SrCrO_4$. CrO_3 is volatile at a temperature above 200 °C, while $SrCrO_4$ is one of the products during Cr-poisoning of LSM oxygen electrode [155]. $SrCrO_3$ shows metallic conductivity but is unstable at 800 °C in the ambient air [156]. On the contrary, $LaCrO_3$ with orthorhombic structure is stable in both ambient air and reducing atmosphere. The stable (La, Sr)(Cr, Fe)O_3 could be engineered to a perovskite in the formula $La_{1-x}Sr_xCr_{1-x}Fe_xO_{3-\delta}$ (x = 0.2−0.67) [157] and their polarization resistances as anode for H_2 oxidation decrease with Cr content. Ce-doped $La_{0.7}Sr_{0.3}Fe_{0.5}Cr_{0.5}O_{3-\delta}$ was found to decrease the polarization resistance of the oxide anode in syngas [122] and the best performance was achieved when 5 at.% $Ce^{4+/3+}$ was used to replace La^{3+} on the A site. Recent research on Bi^{3+} doping on the La^{3+} site ($La_{0.65}Bi_{0.1}Sr_{0.25}Cr_{0.5}Fe_{0.5}O_{3-\delta}$) showed a great enhancement in the performance in H_2 and syngas comparing to $La_{0.75}Sr_{0.25}Cr_{0.5}Fe_{0.5}O_{3-\delta}$ anode [123] and a remarkable performance (360 mW at 800 °C with syngas fuel) can be achieved for the cell $La_{0.65}Bi_{0.1}Sr_{0.25}Fe_{0.5}Cr_{0.5}O_{3-\delta}$ /SDC|LSGM(300)|LSCF/SDC.

Ti doping: Ti^{4+} doping in a cubic $SrFe_{1-x}Ti_xO_{3-\delta}$ ($0 \leqslant x \leqslant 1$) lowers both the ionic and electronic conductivity in air but increases the structural stability of perovskite[158, 159]. $SrFe_{0.7}Ti_{0.3}O_3$ anode showed much higher electric conductivity and smaller area-specific resistance than $SrTi_{0.7}Fe_{0.3}O_3$ counterpart in a reducing atmosphere[160]. $SrFe_{0.7}Ti_{0.3}O_3$ was stable at 650-750 °C under a hydrogen-fueled condition, but showed Fe^0 exsolution at 800 °C for 78 h under 5% H_2 [114]. With Fe^0 exsolution, $SrFe_{0.7}Ti_{0.3}O_3$ anode had an anode polarization resistance (R_p) of 0.17 Ωcm^2 at 800 °C in humidified H_2, much lower than the value 0.39 Ωcm^2 measured for $SrFe_{0.6}Ti_{0.4}O_3$, and 3.14 Ωcm^2 for $SrTiO_3$. A-site deficient $Sr_{0.95}Fe_{0.63}Ti_{0.3}Ni_{0.07}O_3$ was designed for Ni^0 exsolution under a reducing atmosphere and the cell with this anode showed a high power output around 1 W cm^2 at 800 °C (Figure 7

a and c)[113]. Ti^{4+} doping was also used to stabilize LFO and (La, Sr) FeO_3 as in $La_{0.95}Fe_{0.8}Ni_{0.05}Ti_{0.15}O_3$ [29] and $(La,Sr)(Fe,Ti)O_3$ [115]. For example, comparing with $La_{0.95}Fe_{0.8}Mg_{0.05}Ti_{0.15}O_3$, the perovskite $La_{0.95}Fe_{0.8}Ni_{0.05}Ti_{0.15}O_3$ with Ni^0 exsolution showed much lower R_p in 5% H_2 which could be further reduced by the testing in H_2 (Figure 7 b and d). According to the analysis of Barnett *et al.* on the R_p variation vs H_2 partial pressure on $SrFe_{0.7}Ti_{0.3}O_3$ without and with metal decoration, the FOR was limited by the charge transfer in the former while by the adsorption rate in the latter[113].

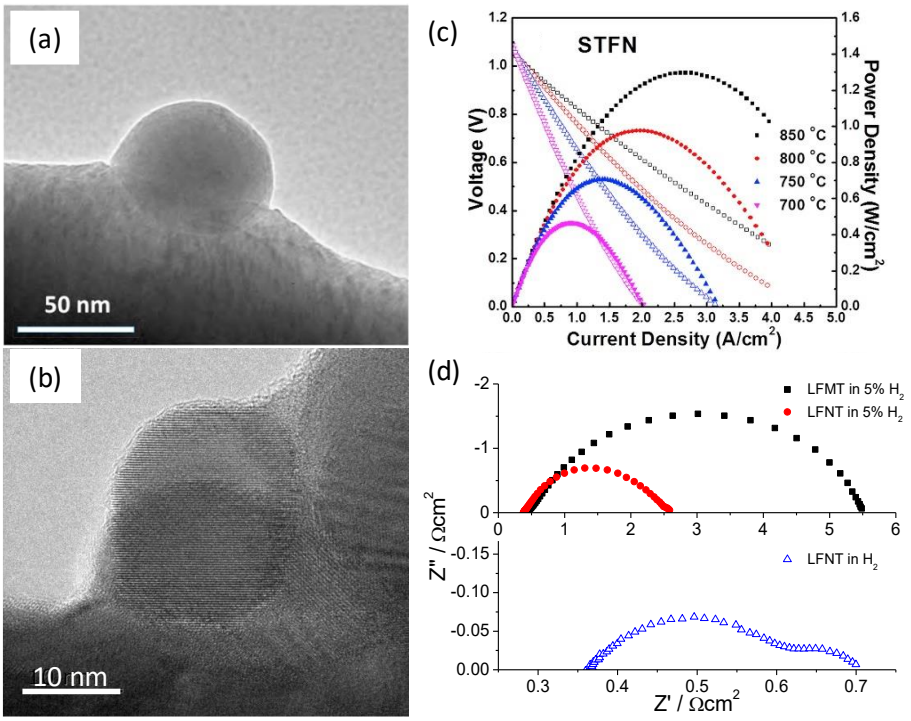

Figure 7. Microstructure of Ni-Fe and Ni^0 catalyst exsolved on the surface of $Sr_{0.95}(Ti_{0.3}Fe_{0.63}Ni_{0.07})O_{3-\delta}$ (STFN) (a) and $La_{0.95}Fe_{0.8}Ni_{0.05}Ti_{0.15}O_3$ (LFNT) (b) after *in situ* reduction at 850 °C and 800 °C, respectively. (c) *I-V* and *I-P* curves of the cell with STFN anode on a LSGM electrolyte (300 μm). (d) Electrochemical impedance spectroscopy of the stable $La_{0.95}Fe_{0.8}Mg_{0.05}Ti_{0.15}O_3$ (LFMT) and LFNT with Ni^0 exsolution under 5% H_2 ($P(O_2) = 10^{-19.6}$ bar) as well as the EIS of the latter under humidified H_2 ($P(O_2) = 10^{-21}$ bar)[29, 113]. (a) and (c) are reproduced from reference 113, copyright Elsevier, and (b) and (d) from reference 29, copyright Royal Society of Chemistry.

Although the power output of cell depends on the thickness/type of electrolyte and the selection of cathode, the statistics of the reported power output (Figure 8) in the

references from Table 1 could provide an overview of the effect of dopants. In most cases, the doping on B site increased the performance of the cell from less than 200 $mWcm^{-2}$ to near 1000 $mWcm^{-2}$ at 800 °C, but it is interesting that the power of the cells increases with the charge of the dopants either for the reducible ($Ni^{2+/3+}$ and $Co^{3+/4+}$) or stable ($Cr^{3/4+}$, Ti^{4+}, Nb^{5+}, and Mo^{6+}) cations.

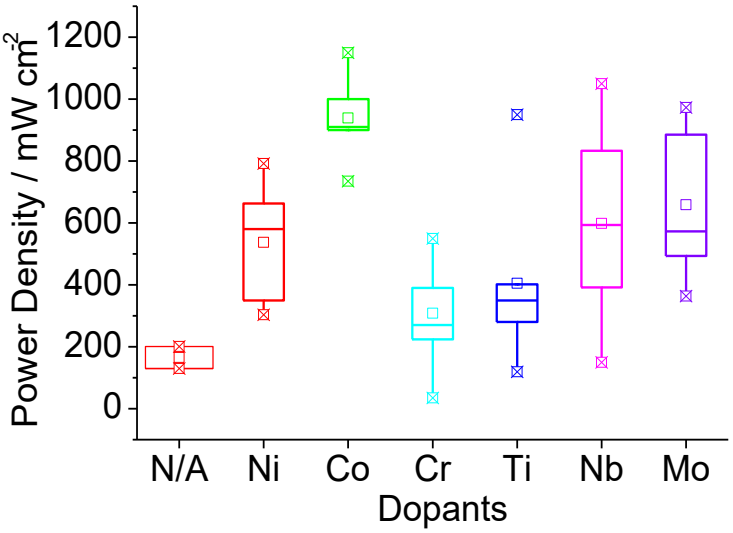

Figure 8 Box plots of the power densities of the cells based on perovskite-type ferrite anode with different B-site dopants. Testing temperature is 800 °C and the fuel is wet H_2.

As the oxides are generally synthesized in the ambient air when Fe^{3+} and Fe^{4+} are stable, the incorporation of higher valence cation requires the substitution of Sr^{2+} on the A site for La^{3+} content if the co-doping of $LaFeO_3$ is taking as an example. The incorporation of Sr^{2+} will expand the unit cell of the reduced oxides and decrease the <Fe-O> bonding energy for higher oxide-ion conductivity. It should be noted that Mo showed multiple valences and was stable as oxide in fuel condition, but it can also change from the stable Mo^{6+} in air to Mo^{5+} and Mo^{4+} for creating oxide-ion vacancies and electronic conduction.

Thermodynamic analysis indicates that FeO can be reduced to Fe^0 under a H_2 atmosphere with low humidity and the high stabilizing energy during the perovskite formation makes possible the utilization for oxide anode. There are limited ferrites other than perovskite explored as stable anodes since a significant quantity of stable cations is needed to reduce the activity of Fe and decomposition or phase transformation [143, 144, 161].

2.3 Iron-containing electrocatalysts

The use of Fe^0 in the catalysis for fuel conversion is also related partially to the stability between Fe^0 and its oxides [162]. In an SOFC, nanostructured metal catalysis can be infiltrated into MIEC oxides to produce long TPBs for the FOR, but the sintering of nano-particles will cause the growth of size along with the diminishing of reaction sites [163, 164]. The sintering of the nanoparticles will cause the loss of active sites of the anode. In order to reduce the degradation from the sintering of catalysts, one possibility is to infiltrate the high-melting-point metals, such as Co_3W alloy[165], while the other is to enhance metal catalysts thermal stability by encapsulating them in a thin, porous metal oxide shell. A Co–Fe alloy infiltrated $PrBaMn_2O_{5+\delta}$ electrode was reported to exhibit excellent activities for hydrocarbon electro-oxidation [25]. The nano-sized metal particles tend to interact strongly with an oxide support, thereby anchoring the metal particle and preventing sintering [166, 167].

The interaction of iron with the oxide support is well-known[162, 168]: iron oxide interacts strongly with γ-Al_2O_3 to produce some spinels which are difficult to reduce completely in hydrogen atmosphere at temperatures below 900 ^oC. The reduction of ferric oxide on the oxide support is also affected by the loading of oxides and alloying with other nobler metals. Specifically, the reduction of Fe^{3+}/Al_2O_3 in H_2 cannot go beyond the Fe^{2+} at low metal loading (0.05 wt.%) unless the temperature is higher than 750 ^oC because ferric ions tend to occupy empty octahedral positions on the alumina surface and are strongly held to retard migration on the surface[169]. Fe^0 should just be the stable form under the humidified H_2 (3% H_2O), but the actual operational SOFC was subjected to the oxidation of anodic current, *e.g.* at 0.7 V, which could vary the chemistry of Fe based catalyst. Irvine *et al.*[170, 171] studied the stability of Ni-Fe infiltrated $La_{0.2}Sr_{0.25}Ca_{0.45}TiO_3$ anode and found that the incorporation of iron could enhanced the performance by a factor of 2.5 compared with the one with Ni infiltration and, more importantly, retarded the degradation of the anode as a result of suppressing the oxide layer covering the metal catalyst and forming of an iron-rich oxide ($(La,Sr,Ca)_2Fe(Ti)O_4$ and/or $La(Sr,Ca)Fe(Ti)O_3$) interlayer (Figure 9) between the $La_{0.2}Sr_{0.25}Ca_{0.45}TiO_3$ backbone and the Fe metal particle.

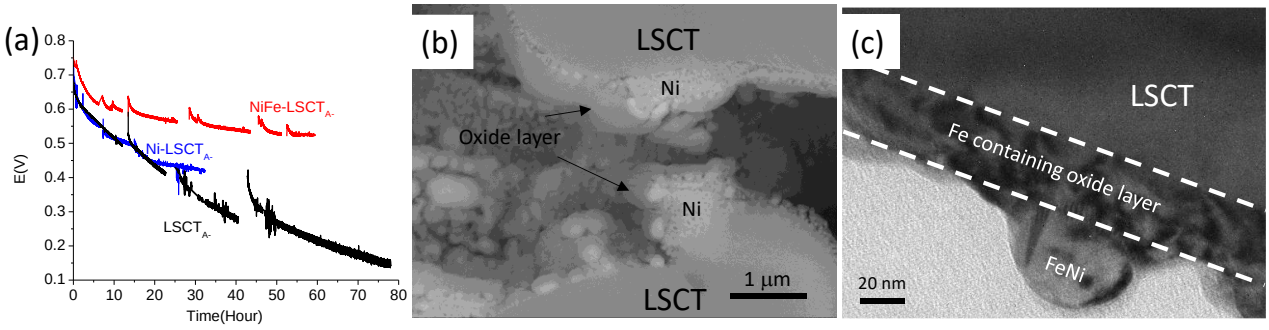

Figure 9. (a) Chronopotentiometry of the cells at 700 °C in humidified hydrogen (3% H_2O) at different current densities: 60, 130, and 280 mA cm^{-2} for the bare pre-reduced $La_{0.2}Sr_{0.25}Ca_{0.45}TiO_3$ (LSCT, Ni and Ni-Fe impregnated LSCT backbones, respectively. Microscopy of the anodes with Ni (b) and Ni-Fe (c) infiltration after stability test, respectively. [171]. Images are reproduced from reference 171. Copyright Royal Society of Chemistry.

Fe_2O_3 deposited on $PrBaMn_{1.7}Co_{0.3}O_{5+\delta}$ *via* infiltration (Figure 10) showed cation-swapping to create $PrBaMn_{1.7}Fe_{0.3}O_{5+\delta}$ with *in-situ* Co^0 alloy exsolution on the surface for high and stable performance under CH_4 for CO production [172]. The dissolution of Fe into the underlying perovskite lattice is ascribed to its low co-segregation energy compared to that of cobalt. Comparing to the Co^0 exsolution from $PrBaMn_{1.7}Co_{0.3}O_{5+\delta}$ creating layered perovskite or A-site cation segregation, the filling of iron on B site actually increased the ionic conductivity and stability.

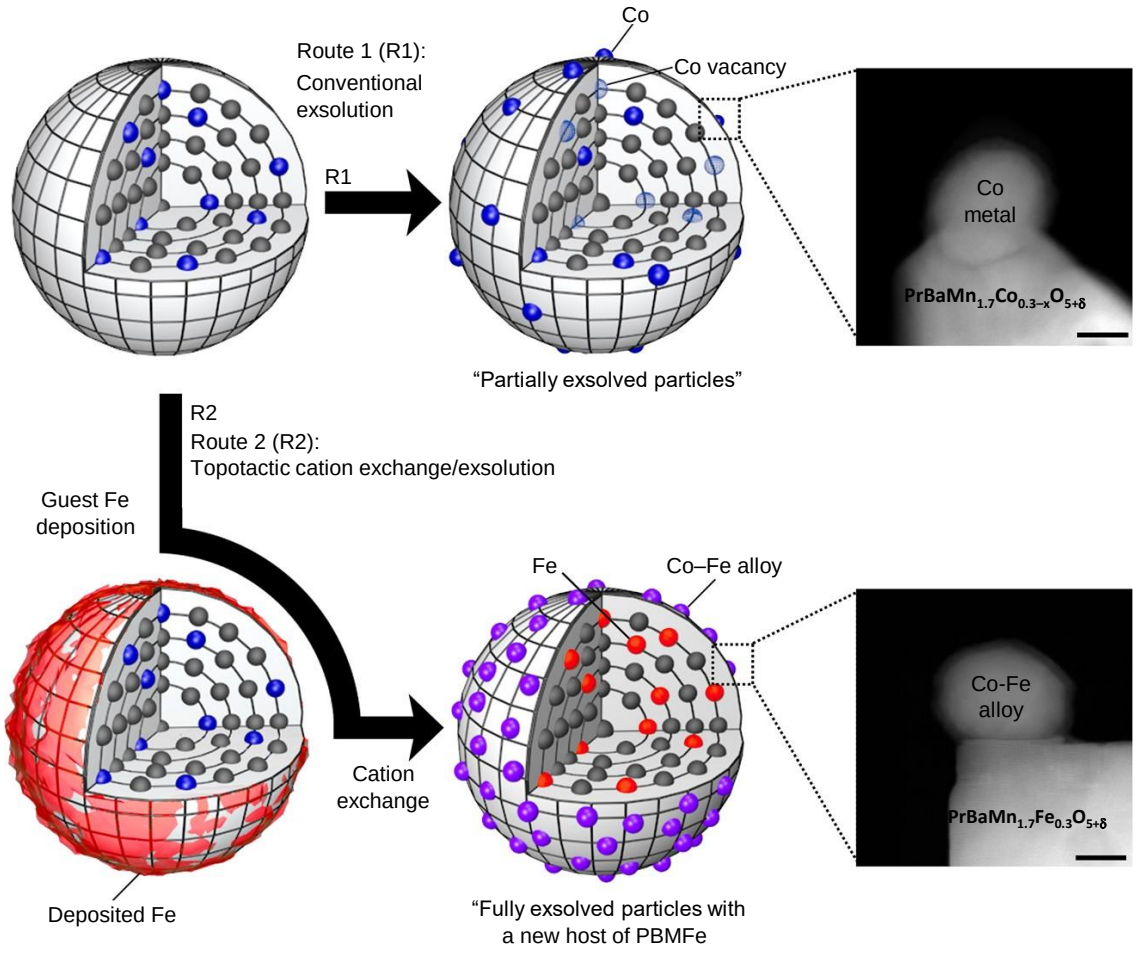

Figure 10 Scheme of cation-swapping between $PrBaMn_{1.7}Co_{0.3}O_{5+\delta}$ (PBMCo) and infiltrated Fe_2O_3 for the exsolution of Co-Fe alloy. Image is reproduced from reference 172, Copy right Springer-Nature.

The exsolved Fe^0 or alloy can be obtained from ferrite perovskite, but the incorporation of Fe^{3+} in other stable non-ferrite perovskites (*e.g.* chromite and titanate) could also induce the growth of nano-sized Fe-containing electrocalyst[173]. In $La_{0.4+x}Sr_{0.4-x}Fe_xTi_{1-x}O_3$ (x=0.06 or 0.09), the exsolution requires higher temperature and lower oxygen partial pressure than the Ni counterparts as the higher Fe-O energy for the segregation. The exsolved Ni-Fe nano-sized alloy on titanate perovskite improves CO oxidation at 450 °C and enhances sulfur tolerance than the exsolved Ni^0 as a result of preserving the initial spacing between the particles[174]. The TPO results (Figure 11) showed that the $(La_{0.7}Sr_{0.3})(Cr_{0.85}Ni_{0.1125}Fe_{0.0375})O_{3-\delta}$ anode had a better carbon deposition tolerance than

the $(La_{0.7}Sr_{0.3})(Cr_{0.85}Ni_{0.15})O_{3-\delta}$ anode as the addition of Fe increased the oxide-ion vacancies of the chromite and initiated the iron doping of the exsolved metal catalysts after reduction[89].

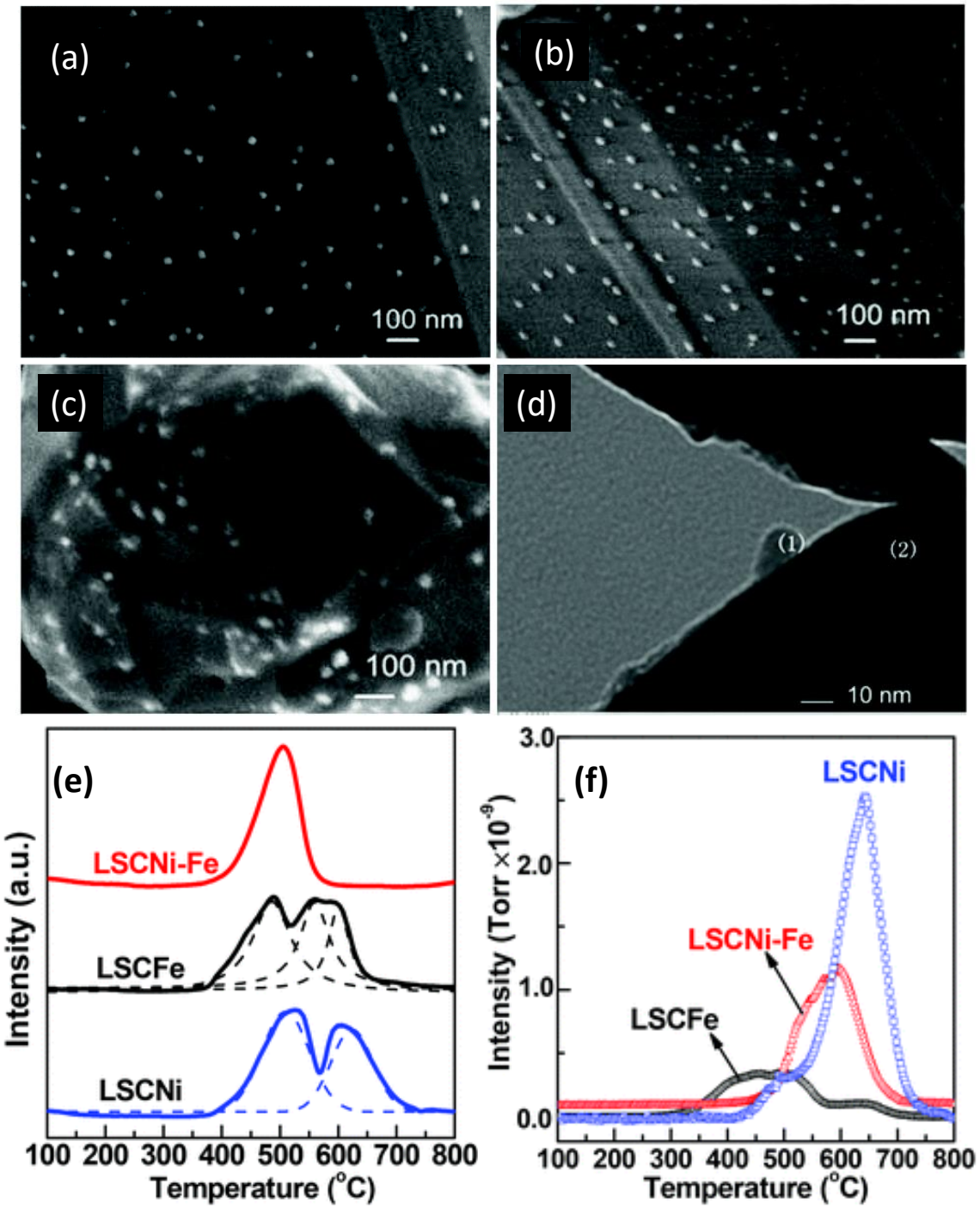

Figure 11. SEM images for the (a) $(La_{0.7}Sr_{0.3})(Cr_{0.85}Ni_{0.15})O_{3-\delta}$ (LSCNi) (b) $(La_{0.7}Sr_{0.3})(Cr_{0.85}Fe_{0.15})O_{3-\delta}$ (LSCFe) and (c) $(La_{0.7}Sr_{0.3})(Cr_{0.85}Ni_{0.1125}Fe_{0.0375})O_{3-\delta}$ (LSCNi–Fe)

materials reduced at 800 °C for 4 h; (d) TEM micrograph of the exsolved nano-particle anchored to the bulk $(La_{0.7}Sr_{0.3})(Cr_{0.85}Ni_{0.1125}Fe_{0.0375})O_{3-\delta}$ material; (e) H_2-TPR profiles for different anode materials and (f) TPO curves for CO_2 evolution of various materials treated with syngas at 850 °C for 24 h [89]. Images are reproduced from reference 89. Copyright Royal Society of Chemistry.

Cu/Fe-$La_{0.75}Sr_{0.25}Cr_{0.5}Mn_{0.5}O_{3-\delta}$ metal-oxide interface is constructed *via* the *in situ* reduction of $(La_{0.75}Sr_{0.25})_{0.9}(Cr_{0.5}Mn_{0.5})_{0.9}(Cu_{1-x}Fe_x)_{0.1}O_{3-\delta}$ (x = 0, 0.25, 0.5, 0.75 and 1) to enhance methane oxidation and redox stability while suppressing the coking and sulfur poisoning[175]. $Sr_2CoMo_{1-x}Fe_xO_{6-\delta}$ (x = 0, 0.05, 0.1) perovskite with Co-Fe alloy exsolution showed excellent coking resistance in CH_4, which could be attributed to the increased oxygen vacancies due to Fe doping and the effective catalysis of multiple-twinned Co-Fe alloy nanoparticles for reforming of CH_4 to H_2 and CO [176]. Co–Fe co-doped $La_{0.5}Ba_{0.5}MnO_{3-\delta}$ ($La_{0.5}Ba_{0.5}Mn_{0.8}Fe_{0.1}Co_{0.1}O_{3-\delta}$) with a cubic−hexagonal heterogeneous structure was found to produce $Co_{0.94}Fe_{0.06}$ alloy nanoparticles during the reduction in hydrogen [177]. A single cell with this anode on a 300 μm thick LSGM electrolyte exhibited maximum power densities of 1479 and 503 mW cm^{-2} at 850 °C with wet hydrogen and wet methane fuels, respectively, and the cell was coking resistant in 200 hours under a methane fuel.

3 Iron-based cathodes for SOECs

3.1 Steam electrolysis

The reversible potential, and therefore the required electrical energy, for steam decomposition decreases with an increasing temperature, leading to an increasing amount of heat energy needed to compensate for the entropy cooling [178]. Hence, the relatively cheap heat energy supplied provides an increasing proportion of the total energy required to produce hydrogen as the temperature increases. Moreover, the overpotential losses in the electrical energy are lower at higher temperatures [179].

At present, the practical development of SOEC lags behind that of SOFC partially because of the degradation of fuel electrode (cathode in SOEC mode) and oxygen electrode (anode in SOEC mode) caused by the interdiffusion and delamination at the

electrode/electrolyte interface[180]. While the delamination of the oxygen electrode is ascribed to the excessive pressure build-up with a high O_2 flow in an over-sintered (larger grain size and smaller pores) region, the R_p of an actual long-term galvanostatic electrolysis is ascribed to the Ni/YSZ fuel electrode [10, 181]. Ni alloying with Fe was found to show much better performance than pure Ni or Pt at 600 °C for the production of H_2 from steam at 600 °C on LSGM electrolyte [19], which is attributed to the preservation of dispersion state of Ni particles by Fe alloying. The water splitting on the Ni-YSZ cathode, for example, happens on the TPB boundary of Ni, YSZ and gas phase[182]: a) adsorption of water molecules (H_2O) on the TPB to form an OH^- ion and a hydrogen atom (reaction 5 to 6), (b) OH^- is reduced by an electron to produce O^{2-} and release a hydrogen atom to combine for H_2 (reaction 8, 9), (c) O^{2-} ions formed this way migrate to the YSZ phase, and (d) O^{2-} ions travel through the bulk of the electrolyte to the anode side to be oxidized for oxygen gas on the cathode.

For Ni-YSZ as hydrogen electrode of SOEC:

$$H_2O(gas) \rightleftharpoons (H_2O)_{ads}(TPB) \quad (5)$$

$$e_{Ni} \rightleftharpoons e_{YSZ}(TPB) \quad (6)$$

$$(H_2O)_{ads}(TPB) + e_{YSZ}(TPB) \rightleftharpoons H_{ads}-S_{Ni} + OH^-(TPB) \quad (7)$$

$$OH^-(TPB) + e_{YSZ}(TPB) \rightleftharpoons H_{ads}-S_{Ni} + O_{YSZ}^{2-} \quad (8)$$

$$2(H_{ads}-S_{Ni}) \rightleftharpoons H_2(gas) + 2S_{Ni} \quad (9)$$

S_{Ni}: an active Ni surface site for reaction species adsorption; $O–S_{Ni}$: an active metal surface site adjacent to an O_{ads} (adsorbed oxygen); H_{ads}: adsorbed hydrogen; O_{YSZ}^{2-}: oxygen ion on an YSZ lattice site; e_{YSZ}: an electron on YSZ surface near TPB; e_{Ni}, e_{YSZ}: an electron near TPB.

Perovskite oxides such as titanates[183, 184], $La_{0.75}Sr_{0.25}Cr_{0.5}Mn_{0.5}O_{3-\delta}$ [185] and ferrites[186] have been selected as the candidates for the dissociation of water molecules. One possible solution to decrease the R_p on the fuel electrode could be the utilization of an MIEC oxide that expands the reaction sites to the surface of the electrode rather than the TPBs for the dissociation of water molecules as in Ni/YSZ cermet[187]. The comparison between the reaction sites on TPBs and on surface of an MIEC is presented in Figure 12.

Moreover, the development of an alternative oxide electrode in SOEC is able to reduce the strain as in Ni(O) cermet cathode during the redox cycle[188] and bring about the avoidance of using H_2 for the pre-reduction or maintaining the reducing atmosphere[185]. For example, Sr_2FeNbO_6(SFN)-YSZ as hydrogen electrode of SOEC, the reaction mechanism could be illustrated in the following equations[189]:

$$H_2O(gas) \rightleftharpoons (H_2O)_{ads,SFN} \quad (10)$$

$$(H_2O)_{ads,SFN} + e_{SFN} \rightleftharpoons H_{ads}\text{-}S_{SFN} + OH_{SFN}^{-} \quad (11)$$

$$OH_{SFN}^{-} + e_{SFN} \rightleftharpoons H_{ads}\text{-}S_{SFN} + O_{SFN}^{2-} \quad (12)$$

$$O_{SFN}^{2-} \rightleftharpoons O_{YSZ}^{2-} \quad (13)$$

$(H_2O)_{ads,SFN}$: a water molecule adsorbed on SFN perovskite; H_{ads}–S_{SFN}: an SFN perovskite surface adjacent to an adsorbed hydrogen; OH_{SFN}^{-}: an OH^- on SFN surface; e_{SFN}: an electron on oxide surface; O_{SFN}^{2-}: oxygen ion on an SFN lattice site.

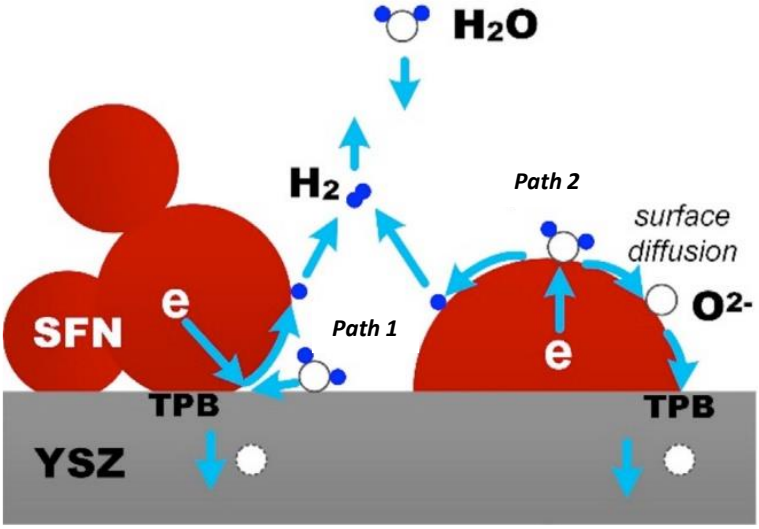

Figure 12. Paths for the decomposition of H_2O in SFN-YSZ electrode[189]. *Path 1* illustrates the reaction route on a TPB, similar to an Ni-YSZ composite anode and *Path 2* represents the reaction on the surface of an MIEC perovskite. Image is reproduced from reference 189, Copyright Elsevier.

The exchange current density of LSF from DC polarization is 14 mA cm^{-2} at 700 °C, which is very close to that of Ni-YSZ[186]. In this respect, the electrocatalysis of the metal-free ferrite towards the water splitting is desirable since it is subjected less to microstructural variation than the Ni cermet counterpart as it can survive the reduction process. Sr_{1-}

$_xPr_xFeO_{3-\delta}$ (SPF) (x=0.02, 0.04, 0.06, 0.08 and 0.10) was explored as the cathode for the electrolyser fed with steam and the best performance was found at x=0.04, showing an R_p of 0.25 Ω cm^2 in a reducing atmosphere at 800 °C [190]. The high performance of MIEC ferrite perovskite lies in the expansion of reaction sites, but the superficial reduction under a cathodic bias is also important to the electrocatalysis of water splitting. Opitz *et al.*[187] found that Fe^0 was evident in the *in situ* NAP-XPS (near-atmosphere-pressure X-ray Photoemission Spectroscopy) of the $La_{0.6}Sr_{0.4}FeO_3$ electrode under the slight cathodic current (Figure 13).

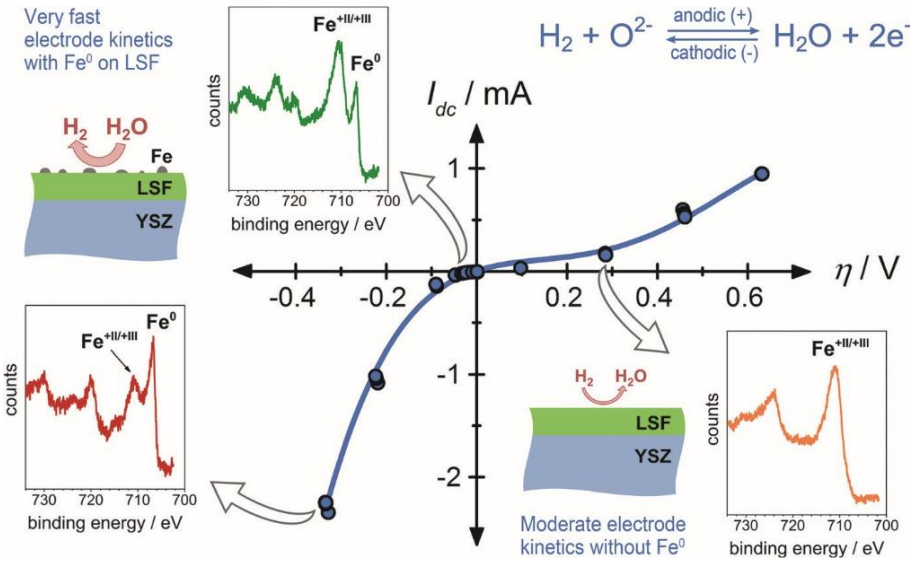

Figure 13. Current–overpotential curve (I_{dc} vs. η) of $La_{0.6}Sr_{0.4}FeO_{3-\delta}$ in a humid reducing atmosphere (0.25 mbar H_2 + 0.25 mbar H_2O). The symbols represent measured values; the line is not a fit but a guide for the eye. The reaction proceeding on the surface of the LSF working electrode is given top right. For selected points of the curve (indicated by arrows), Fe 2p XPS spectra are shown as insets. The sketches indicate the situation for the LSF surface and the resulting reactivity, respectively[187]. Image is reproduced from reference [187], Copyright Wiley-VCH.

The electrochemically-driven evolution of Fe^0 particles on the surface might induce the formation of R-P phase underneath with better thermodynamic stability limit than the perovskite and thus inhibit the further reduction and increase the structure and redox stability by confining the dimension of exsoluition[191]. The R_p of the cell with Fe loading in

$La_{0.7}Sr_{0.3}VO_3$ (LSV) cathode *via* infiltration decreased R_p by 50 %, though it was twice that of Ni-infiltrated LSV cathode, indicating that Fe^0 as metal electrocatalysts was not as efficient as Ni^0 in the water-splitting reaction but was still better than pure oxide[192]. The current density of the electrolysis cell with the $(La_{0.2}Sr_{0.8})_{0.9}Ti_{0.9}Fe_{0.1}O_{3-\delta}$ -GDC electrodes reached approximately 150 $mA{\cdot}cm^{-2}$ at 1.6 V at 800 °C, higher than 120 $mA{\cdot}cm^{-2}$ for the bare $(La_{0.2}Sr_{0.8})_{0.9}TiO_{3-\delta}$ -SDC electrodes, because of the reversible growth of Fe^0 particles on the surface in the former[193]. The improved electrocatalysis of Fe^0 over oxide cathode could indicate that the intrinsic exsolution of Fe^0 under cathodic current [194] could induce the "smart" behavior of ferrite perovskite that maintains high electrocatalysis and stability under a cathodic bias for electrolysis.

3.2 CO_2 electrolysis and CO_2/H_2O co-electrolysis

High-temperature CO_2 splitting SOEC could greatly assist the reduction of CO_2 emissions by electrochemically converting CO_2 to valuable fuels through effective electrothermal activation of the stable C=O bond[52]. Although Ni-cermet exhibits an excellent catalytic activity for CO_2/H_2O co-electrolysis, they tends to suffer from some drawbacks of impurity poisoning, oxidation, particle aggregation and coke deposition, *etc.*[195, 196]. These phenomena would result in cell performance degradation [197]: a short stack Jülich F10 design with anode-supported cells for CO_2-H_2O co-electrolysis for syngas production showed ~2% kh^{-1} voltage degradation at 800 °C as a result of the Ni depletion at the cathode/electrolyte interface.

$La_{0.8}Sr_{0.2}FeO_3$ was found to be an excellent electrocatalyst for CO_2 reduction reaction in SOECs [198] and the reactions on the cathode were proposed based on the result of Raman spectroscopy and density functional theory (DFT) calculations [199]:

$$CO_2(gas)+O_{LSF}^{2-}=CO_3^{2-}(ads) \quad (14)$$

$$CO_3^{2-}(ads)+e^-=CO_2^-(activated, bent)+O_{LSF}^{2-} \quad (15)$$

$$CO_2^-(activated, bent)+e^-=CO(ads)+O^{2-}(ad) \quad (16)$$

$$CO(ads)=CO(gas) \quad (17)$$

In the initial step, a CO_2 molecule is chemically adsorbed on the LaSrFeO terminated surface and transforms into stable adsorbed carbonate ($CO_3^{2-}(ads)$) species. $CO_3^{2-}(ads)$,

upon the accepting an electron can further transform to an activated bent CO_2^- (CO_2^- (activated, bent)) on the surface, which decomposes to adsorbed CO (ads) and an adsorbed oxygen anion (O^{2-}(ads)) upon further acceptance of an electron.

Operando NAP-XPS measurement on a $La_{0.6}Sr_{0.4}FeO_{3-\delta}$ cathode for CO_2 electrolysis indicated the formation of carbonate intermediates and Opitz *et al.*[200] proposed that the oxide ion vacancies (Vac) produce CO^{2-} or CO_3^{3-} radicals ($CO_2^{\bullet-}$(ads) or $CO_3^{\bullet 3-}$ (ads)) when CO_2 is adsorbed and attached to the surface of an MIEC ferrite with oxide ion vacancies and electron flow.

$$CO_2(gas) + Vac + e- = CO_2^{\bullet-}(ads) \quad (18)$$

$$CO_2^{\bullet-}(ads) + O^{2-} = CO_3^{\bullet 3-}(ads) \quad (19)$$

$$CO_3^{\bullet 3-}(ad) + e- = CO(gas) + 2O^{2-} \quad (20)$$

These reactions indicate that electron transfer is required to form the carbonate [201] and thus to activate CO_2 on the oxide surface while the number of reaction sites is controlled predominantly by the oxygen vacancies of the perovskite.

Ti doping in $La_{0.75}Sr_{0.25}Cr_{0.5-x}Fe_{0.5}Ti_xO_{3-\delta}$ (x = 0, 0.1, 0.2, 0.3, 0.4 and 0.5) [202] improves the current efficiencies at x=0.1 under a wide range of potentials for CO_2 electrolysis at 800 ^oC. SFO was unstable for a CO_2 electrolyser [203], but perovskite-type $La_{0.3}Sr_{0.7}Fe_{0.7}Ti_{0.3}O_3$ [204] and $La_{0.3}Sr_{0.7}Fe_{0.7}Cr_{0.3}O_{3-\delta}$ [205, 206] with the partial Cr^{3+} or Ti^{4+} substitution for $Fe^{3+/4+}$ were found to be stable. Ce was doped into A site of $La_{0.7}Sr_{0.3}Cr_{0.5}Fe_{0.5}O_{3-\delta}$ to promote the catalytic performance, and to introduce oxygen vacancies in the lattice *in situ* after reduction under the operational condition [207].

The increased amount of oxygen vacancies not only facilitated the mobility of oxygen ions, but also provided favorable accommodation for chemical adsorption of CO_2. The introduction of vanadium in ferrite perovskite ($La_{0.5}Sr_{0.5}Fe_{1-x}V_xO_{3-\delta}$, x=0, 0.05, 0.1, 0.15) promoted the formation of oxygen deficiencies and altered the electronic structure of Fe, thus greatly enhanced the adsorption and dissociation of CO_2 [208]. 10% Nb doping in in $La_{0.6}Sr_{0.4}FeO_3$ also found to increase the electrolysis of CO_2 and a current density of 0.85 Acm^{-1} at 1.5 V was obtained at 800 ^oC [209]. A small amount of Mn is effective for improving the activity of LFO-based cathode for CO_2 electrolysis: a cathodic current density of 335

and 240 mA cm^{-2} at 1.6 V/800 ^{o}C was achieved on a cell with $La_{0.6}Sr_{0.4}Fe_{0.9}Mn_{0.1}O_3$ and $La_{0.6}Sr_{0.4}FeO_3$ cathode on SLGM electrolyte, respectively[210].

$Sr_2Fe_{1.5}Mo_{0.5}O_{6-\delta}$ is a typical oxide cathode that can be used on LSGM based electrolyte and shows a superior performance for CO_2 electrolysis even under pure CO_2 feeding gas[211-214]. A high current density of 1.09 A cm^{-2} could be obtained at 1.5 V at 800 ^{o}C for a cell with $Sr_2Fe_{1.5}Mo_{0.5}O_{6-\delta}$/GDC cathode. F^- anion doping in $Sr_2Fe_{1.5}Mo_{0.5}O_{6-\delta}$ was found to increase the CO_2 adsorption: the electrolysis cell based on $Sr_2Fe_{1.5}Mo_{0.5}O_{6-\delta}F_{0.1}$ cathode could give a high current of 1.36 A cm^{-2} at 1.5V at 800 ^{o}C and high stability under continuous operation under a high current density [215].

Fe-Ni nanospheres exsolved from $La_{0.6}Sr_{0.4}Fe_{0.8}Ni_{0.2}O_{3-\delta}$ under reduction in H_2 were found to greatly enhance the performance of the electrode for CO_2 electrolysis (Figure 14) and a high current density of 1.78 A cm^{-2}, along with a high Faraday efficiency ($\sim$ 98.8%), were achieved at 1.6 V and 850 °C for the cell with $La_{0.6}Sr_{0.4}Fe_{0.8}Ni_{0.2}O_{3-\delta}$ cathode with the exsolved Ni-Fe metals[216]. Co-Fe outgrown on the surface of ferrite perovskite was found to be important for the CO_2 activation as a result of the metal/oxide interface [217, 218]. $La_{0.66}Ti_{0.8}Fe_{0.2}O_{3-\delta}$ with A-site deficiency exhibits stable electrochemical performance over 300 h with the current density maintained above 0.5 A cm^{-2} and the exsolution of Fe on the surface was found to be important for the high performance[219].

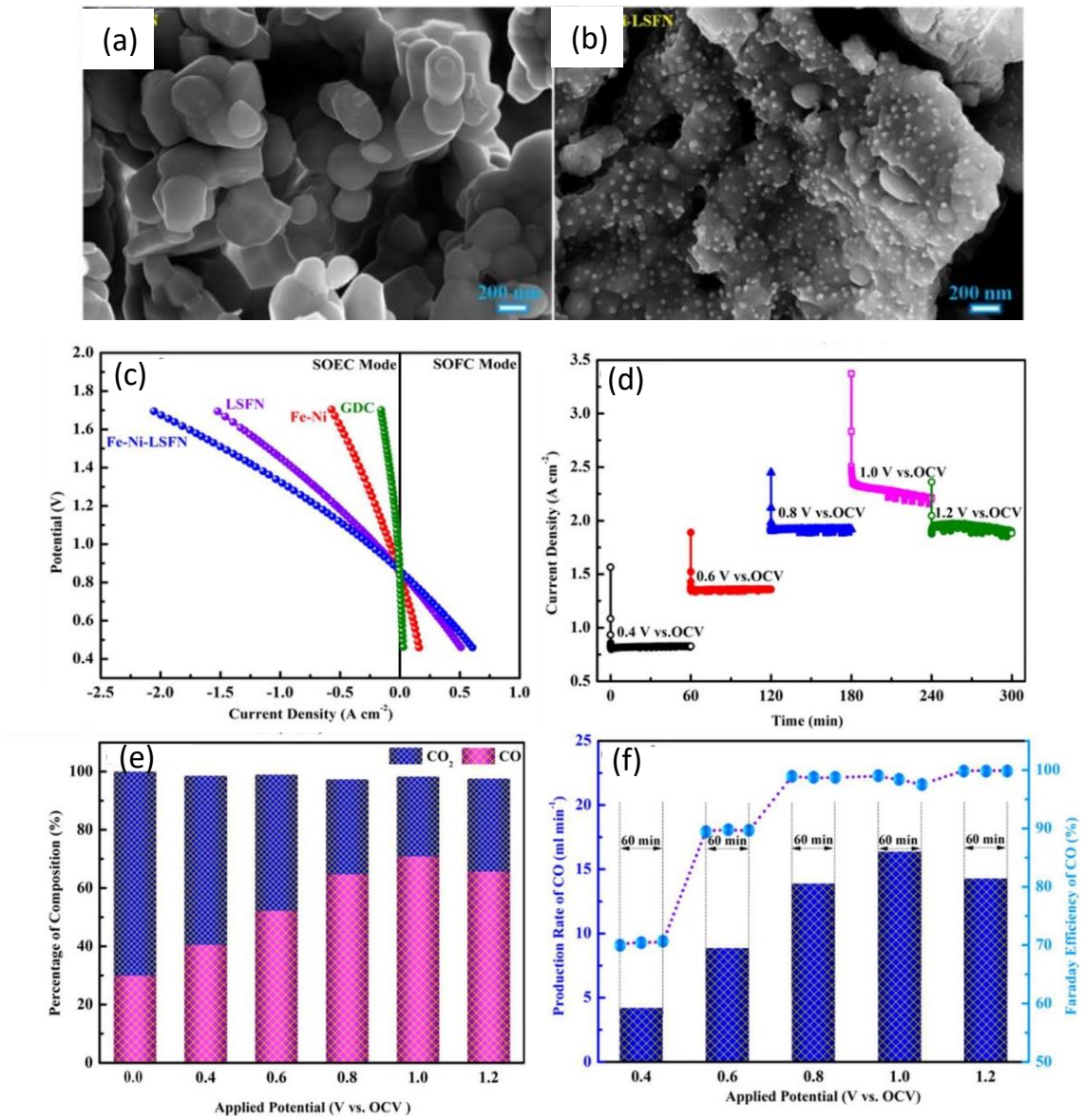

Figure 14 SEM images of $La_{0.6}Sr_{0.4}Fe_{0.8}Ni_{0.2}O_{3-\delta}$ powders (a) before and (b) after reduction in 5% H_2/N_2 at 850 °C for 2 h. (c) Comparison of current-voltage curves for CO_2 electrolysis using the Fe–Ni- $La_{0.6}Sr_{0.4}Fe_{0.8}Ni_{0.2}O_{3-\delta}$, $La_{0.6}Sr_{0.4}Fe_{0.8}Ni_{0.2}O_{3-\delta}$, GDC and Fe–Ni as cathode catalysts at 850 °C. (d) Potential static tests for CO_2 electrolysis at different applied potentials at 850 °C and (e) corresponding CO_2/CO compositions in the outlet gases. (f) Production rates and Faraday efficiencies of CO_2 electrolysis at different applied potentials at 850 °C. A GC run repeated every 10 min in 1 h. The average value of two measurements was taken as the gas volumetric concentration for Faraday efficiency

calculation, and three average values were used for the plot. Image was obtained from Ref. [216]. Images are reproduced from reference [216]. Copyright American Chemical Society.

Simultaneous electrolysis of CO_2 and H_2O are proposed to produce value-added chemical through the Fischer-Tropsch (FT) reaction besides simple H_2 or CO.[196, 220, 221] Fe(O) has been placed on the top of the $La_{0.2}Sr_{0.8}TiO_{3+\delta}$ cathode of an electrolyser for the *in situ* production of H_2/CO and CH_4 during the co-electrolysis of CO_2 and H_2O.[222] The Faraday efficiency was high for the production of H_2/CO at a high-temperature (e.g. 800 ^oC), but the production of CH_4 can be greatly enhanced by the lowering of temperature for the FT reaction [223] or the increase of operating pressure of the cathode[224].

Detailed summaries on CO_2 and H_2O co-electrolysis were found in a recent review by Zhang *et al.* and Bao *et al.* [196, 225]: Ni(O) cermet was still the popular choice for the cathode. Because the overpotential for CO_2 dissociation is much more difficult than H_2O, [221] the direct electrolysis of CO_2 in a mixed CO_2 and H_2O will not be significant unless the CO_2 concentration is much higher than that of H_2O.[220] Therefore, the requirement on the cathode of an electrolyser using CO_2 and H_2O as feedstock would not differ too much from that using CO_2: high stability, oxide-ion conductivity, affinity to CO_2 and coke resistance[226]. Though the reverse water-gas-shift reaction (RWGSR, H_2 (g) +CO_2 (g)=H_2O (g)+CO (g)) is thermodynamically favorable at a temperature higher than 810 ^oC, the final gas composition could be affected by the residence time of the gas on the electrode and kinetic limitations [227, 228].

The RWGSR could be beneficial to the production of CO, especially when H_2 is introduced along with H_2O and CO_2.[229-231] However, the input of H_2O or CO in the cathode chamber could be avoided if oxide rather than Ni(O) was used as cathode. $Sr_2Fe_{1.5}Mo_{0.5}O_{6-\delta}$ cathode for electrolysis of CO_2 and H_2O was found to show a polarization resistance than the titanite or chromite-based counterparts by one order of magnitude [232]. A-site deficient $La_{0.7}Sr_{0.2}Ni_xCo_yFe_{1-x-y}O_{3-\delta}$ (x, y=0; x=0, y=0.2; x=0.1, y=0.1; x=0.2, y=0) cathode with varied Co or Ni content showed higher Faraday efficiency and H_2/CO ratio when Ni is used to replace Co because the Co doped ones could be oxidized for by

CO_2+H_2O during the electrolysis [233]. $La_{0.7}Sr_{0.2}Ni_{0.2}Fe_{0.8}O_3$ cathode was found to be stable at a current density lower than 20 mA cm^{-2} and the CO/H_2 ration in the efflux and Faraday efficiency was found to increase with temperature from 700 °C to 800 °C.[234]

4. Iron-based oxygen electrodes

Oxygen atoms diffusing into the porous matrix of the cathode of an SOFC are supposed to be reduced to O^{2-} while the O^{2-} generated from the cathode of an SOEC will be transported to the oxygen electrode to be oxidized to oxygen molecule in the anode. The partial reduction of SFO can create oxygen vacancies and increase oxide-ion conduction providing that the oxide-ion defects are not in a long-range ordered state. However, SFO in the extreme case can also be reduced to $Sr_2Fe_2O_5$ [235], an orthorhombic brownmillerite below 850 °C [30]. The brownmillerite-type $Sr_2Fe_2O_5$ containing ordered corner-sharing <FeO_4> tetrahedra and <FeO_6> octahedra can possibly transform to a $Ca_2Mn_2O_5$-type structure with <FeO_5> pyramids at a temperature above 850 °C, but the long-range oxygen vacancy ordering in both structures causes low oxide-ion conductivity[30, 236].

Acceptor doping in LFO, such as Sr^{2+} on La^{3+} or Mg^{2+},Ni^{2+} on Fe^{3+} site, results in the formation of oxide-ion vacancies and a Fe^{3+} to Fe^{4+} charge compensating transition, and subsequent enhancements in both electronic and ionic conductivities[237, 238]. $LaFe_{1-x}Ni_xO_{3-\delta}$ (x=0.2-0.5) with Ni substitution for Fe also showed improved electronic and ionic conductivity than the parent LFO[239] and similar TEC ((8.9 –11.9) ppm K^{-1}) to the YSZ electrolyte. The ionic conductivity of $La_{0.8}Sr_{0.2}FeO_{3-\delta}$ was measured to be 4.5 x 10^{-3} S cm^{-1} at 800 °C[240] and the TEC was 12.6 ppm K^{-1}, slightly higher than that of YSZ. A cell based on 10 μm YSZ electrolyte with SDC buffer layer showed a high power output of 950 mW cm^{-2} at 750 °C[241]. Although no distinct insulating phase was found in a composite of LSF and YSZ at 1400 °C, LSF showed increased cation interdiffusion with YSZ (mostly Zr diffuses into perovskite phase) with the ratio of Sr/La in the perovskite that causes the decrease of electronic and ionic conductivity[242]. The donor doping of Zr^{4+} would decrease the oxygen non-stoichiometry of LSF and the undersized Fe^{3+} dopants in YSZ would compete for the oxygen vacancies[243]. CaO doped LFO (LCF) has also attracted attention to avoid

the use of SrO as in LSF to improve the Cr poisoning and mitigate the cation diffusion of Sr^{2+} into the adjacent electrolyte [244].

The ionic conductivity of perovskite oxides is in the sequence of manganite < ferrite < cobaltite, but the TEC match between the electrocatalysts with YSZ is in the reverse sequence (Figure 15). The ultra-high TEC of cobaltite perovskite could be an indication of structural instability as a result of chemical expansion related to the oxygen loss [245] and the spin-state transition of cobalt cation [246] upon heating. LSCF plays an important role as the oxygen electrode owing to the high MIEC properties, good structural stability and high electrochemical activity and has been reviewed by Jiang[247]. LSCF is not compatible with the most popular YSZ electrolyte, but it can be used for GDC or LSGM electrolyte. The Sr and Co incorporation increased the ionic conductivity (σ_i): *e.g.* the ionic conductivity of LSCF ranged in the order of 1-10^{-2} S cm^{-1} at 800 °C [248]. $Sr_{0.9}La_{0.1}Co_xFe_{1-x}O_{3-\delta}$ (x=0, 0.2 and 0.5) cathode on YSZ electrolyte if sintered at 1100 to 1250 °C showed the presence of the Sr-Zr-O layer, the thickness of which increased with Co content[249].

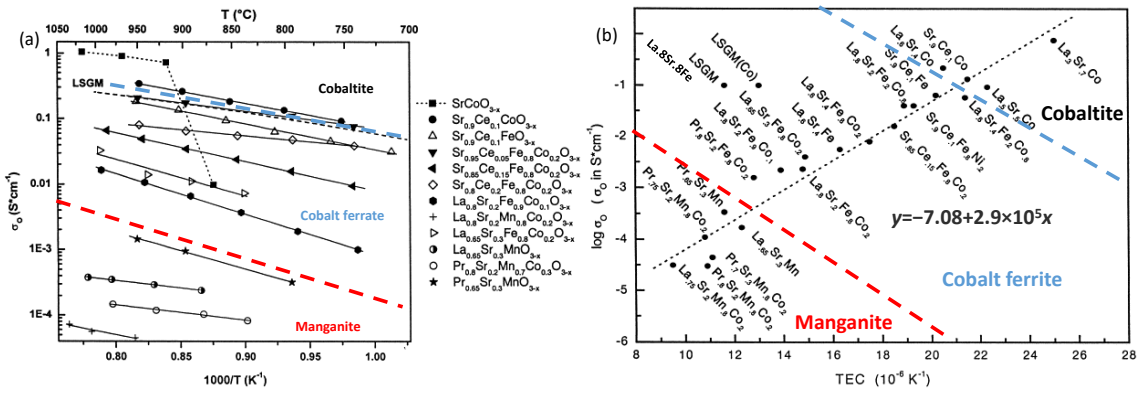

Figure 15. (a) Oxide-ion conductivity (σ_o) and (b) thermal expansion coefficient (TEC) of manganite, cobalt ferrite and cobaltites at 800 °C [250]. The equation in (b) indicates the fitted relationship between TEC and conductivity. (a, b) are modified from reference 250. Copyright Elsevier.

$La_{0.6}Sr_{0.4}Co_{0.2}Fe_{0.8}O_{3-\delta}$ is a widely studied composition considering the moderate TEC (around 15.0 ppm K^{-1} at 700 °C [251]), decent electrochemical performance and durability. The R_p of $La_{0.6}Sr_{0.4}Co_{0.2}Fe_{0.8}O_{3-\delta}$ depends on the preparation technique, *e.g.* particle size and calcination temperature on electrolyte for bonding, and surface modification (Figure

16a). The electrode sintered at 1100 °C showed an R_p 10 times than that sintered at 800 °C while the Pd and GDC infiltration into $La_{0.6}Sr_{0.4}Co_{0.2}Fe_{0.8}O_{3-\delta}$ could decrease the R_p by 75% [252].

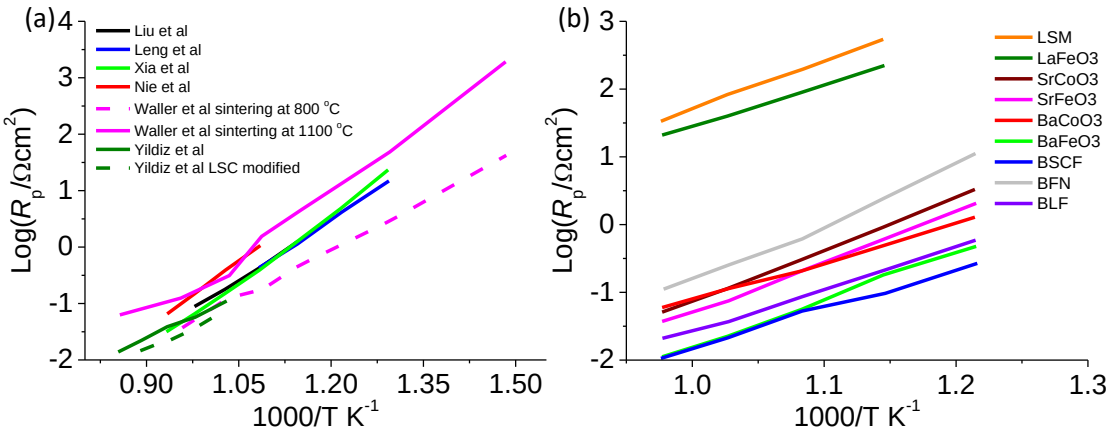

Figure 16. R_p of selected SFO or $BaFeO_3$ ferrite perovkites[253] in comparison with the reported R_p of (a) LSCF [254-258] and (b) the typical cobaltite and manganite on ceria-based electrolyte or buffer layer. BLF, BFN and BSCF represent $Ba_{0.9}La_{0.1}FeO_{3-\delta}$ [246], $BaFe_{0.9}Nb_{0.2}O_{3-\delta}$ [259], and $Ba_{0.5}Sr_{0.5}Co_{0.8}Fe_{0.2}O_{3-\delta}$ respectively.

Binary oxides of less reducible cations, such as Nb^{5+}, V^{5+}, Ti^{4+}, Hf^{4+} *et al.*, are also deposited onto LSCF to increase the surface stability and surface oxygen exchange coefficient, K_{chem} [260]. The deposition of these less reducible cations was stipulated to decrease the $V_O^{\bullet\bullet}$ to the perovskite to decrease the surface segregation of SrO. As these oxides reduce the surface $V_O^{\bullet\bullet}$ that accelerates the K_{chem} and the surface SrO that hindering the K_{chem}, a volcanic plot can be obtained between the oxygen formation enthalpy of the oxides and the K_{chem}. A recent study on the group IIIA oxides [261] (B_2O_3, Al_2O_3, Ga_2O_3 and In_2O_3) and NiO [262] and MgO [263] was also found to be effective in increasing the K_{chem} of LSCF. For example, at 800 °C, the deposition of 0.202 mg cm^{-2} In_2O_3 particles increases the coefficient from 4.53x 10^{-5} to 2.81 x 10^{-4} cm s^{-1} for LSCF and from 2.39 x 10^{-5} to 9.3 x 10^{-5} cm s^{-1} for LSF. More recent work on $Pr_{0.1}Ce_{0.9}O_{2-\delta}$ indicates that the acidity of the infiltrated binary oxides could be an excellent descriptor of the improvement/degradation in K_{chem} [264].

LSM coated LSCF has been demonstrated to show superior performance than the one without coating under a cathodic current around 0.1 A cm^{-2} and this could be related to surface activation under cathodic polarization due to the promotion of oxygen adsorption and/or dissociation associated with an Mn cation by the surface layer of a hybrid (La,Sr)(Mn,Co)O_3 phase and the dramatically increased oxygen vacancy population under a cathodic bias[265, 266]. LSCF inhibited the Cr poisoning as a result of the surface segregation of Co_3O_4 on the surface of the electrode[267].

LSCF/CeO_2 heterostructure composite nanofibers achieved an R_p of 0.031 Ω cm^2 at 700 °C, approximately 1/5 of that for the LSCF powder cathode (0.158 Ω cm^2), because the interfacial cation interdiffusion between CeO_2 and LSCF caused the aliovalent La^{3+} doping in the former and valence variation of Co^{3+} and Fe^{3+} in the latter to increase oxygen vacancy concentration and then facilitated the incorporation and transport of oxygen[268, 269]. $La_{0.8-x}Bi_xSr_{0.2}FeO_{3-\delta}$ ($0 \leqslant x \leqslant 0.8$) showed a decreased conductivity along with Bi^{3+} doping, but the K_{chem} and chemical diffusion coefficient (D_{chem}) can be improved along with Bi incorporation. Specifically, an R_p of 0.1 Ω cm^{-2} at 700 °C was obtained for $La_{0.4}Bi_{0.4}Sr_{0.2}FeO_{3-\delta}$ cathode on SDC electrolyte[270].

Rare-earth-element-free $Ca_2Fe_2O_{5-\delta}$, SFO, $BaFeO_{3-\delta}$ were also studied as the parent materials for oxygen electrodes. $Ca_2Fe_2O_{5-\delta}$, a brownmillerite, is almost stoichiometric at atmospheric oxygen pressure ($\delta < 0.02$). The TEC of $Ca_2Fe_2O_{5-\delta}$ is around 11-13 ppm K^{-1}, matching well with electrolyte material, but relatively low ionic conductivity, 2 mS cm^{-1} at 900 °C [271]. The cathode based on $Ca_2Fe_{2-x}Co_xO_{5-\delta}$ (x=0.2, 0.4, 0.6) showed its best performance of 0.2 Ω cm^{-2} at 700 °C when x=0.2 [272]. In contrast, the TEC of perovskite-type SFO was very high 40.8 ppm K^{-1} at 800 °C [148], while $BaFeO_{3-\delta}$ suffered from the phase change from corner-sharing perovskite to face-sharing oxygen-deficient 6H phase at 600 °C in the air[44].

Due to the drawbacks of SFO and BFO in the structure stability and large TEC, doping is generally acquired for practical oxygen electrode fabrication (Figure 16b). The donor doping (*e.g.* La^{3+} or Nb^{5+}) on Sr^{2+}/Ba^{2+} or $Fe^{4+/3+}$ site is the general technique to improve the stability and reduce the TEC by decreasing the smaller size Fe^{4+} cation in the structure.

$SrFe_{0.85}Ti_{0.1}Ni_{0.05}O_{3-\delta}$ cathode decorated with uniformly distributed and well bonded NiO nanoparticles prepared *via* the reduction under hydrogen for exsolution of Ni^0 was found to reduce 50% of the R_p for ORR[273]. Cobalt and titanium substituted SFO ($SrTi_{0.3}Fe_{0.63}Co_{0.07}O_{3-\delta}$) as the oxygen electrode material for intermediate-temperature SOC provided both excellent oxygen electrode performance and long-term stability even under high current densities (1 A cm^{-2})[274]. Mo-doped SFO ($SrFe_{1-x}Mo_xO_3$, $0<x<0.25$) was also used for the oxygen electrode[148] and the strong hybridization of the Fe-d and O-p states was proposed to promote the formation of oxygen vacancies, allowing for facile bulk oxide-ion diffusivity and electronic conductivity[275].

Anion doping in perovskite is also employed to enhance the mobility of oxide ions by increasing the oxygen reduction reaction. Cl^- and F^- are the popular choices for replacing the oxide ions [276, 277] in ferrite perovskite ($SrFeO_3$, $SrFe_{0.9}Ti_{0.1}O_3$, and $SrFe_{0.75}Mo_{0.25}O_3$) and the enhancement in electrocatalysis was ascribed to the increase in K_{chem} and D_{chem} [278, 279]. The incorporation of F^- or Cl^- decreases the valence electrons on O^{2-} and weakens its bonding with cations on A or B site, which increases the mobility of oxide ions.

5 Iron-based symmetrical and reversible SOCs

5.1 Symmetrical solid oxide fuel cells

One of the recent directions in the development of SOFCs is a symmetrical configuration, where identical electrode materials are used simultaneously for an oxygen electrode and fuel electrode. In the last decade, the development of symmetrical SOFCs has gained a lot of interest[8, 48, 280], because of the simple fabrication process with one thermal treatment step for both electrodes to reduce the cost of cell production and provide a possible way of reversing the sulfur degradation and carbon deposition through reversing the gas flow in the fuel electrode chamber to oxidizing atmosphere. Therefore, this state-of-the-art approach could allow for higher tolerance of sulfur- and carbon-containing fuels. However, the challenges of symmetrical SOCs lie in the selection of electrode materials boasting acceptable structural stability and electrical conductivity in both oxidizing and reducing atmospheres as well as reasonable electrochemical activity for oxygen reduction at the oxygen electrode and fuel oxidation at the fuel electrode[140]. The development of

symmetrical SOFCs has been reviewed in ref. [48] and [8], but we focus here more on iron-based symmetrical electrodes.

5.1.1 (Sr, Ba)FeO_3-Based Oxides

The electrode materials for symmetrical SOCs were initially limited to structurally stable oxides or mixed compounds under both reducing and oxidizing conditions[112]. Among the redox stable materials, iron-based perovskites could be potentially used as both anode and cathode in symmetrical SOFCs. SFO in air presented a semiconductor-type behavior between room temperature and 500 ^oC, which could be described by the small polaron conduction mechanism. A drop in the conductivity was observed as the temperature increased above 500 ^oC in air, which was related to the thermal reduction of Fe^{4+} to lower valence states and the consequent decrease in the number of charge carriers[281]. The high-valence transition-metal doping in SFO results in a decrease in conductivity in air due to a decrease of Fe^{4+} in Fe^{4+}-O-Fe^{3+} transition for electron/hole transport (Figure 17a).

The conductivity of SFO containing 25% B-site doped cations in $SrFe_{0.75}Ti_{0.25}O_3$ showed a maximum value of 40 S cm^{-1} at 600 ^oC [282]. The isothermal conductivity of undoped SFO is sensitive to the oxygen content and oxygen partial pressure: it showed a *p*-type conducting behavior under oxygen partial pressures above 10^{-5} atm. and predominant n-type conduction below 10^{-15} atm at 800 ^oC [283]. The conductivity of SFO in reducing atmosphere was quite low because of the losing Fe^{4+} and the phase transformation to brownmillerite ($Sr_2Fe_2O_5$) with ordered oxygen vacancies. SFO may be doped on B site with different more redox stable cations than $Fe^{2+/3+/4+}$ such as Ti^{4+}, Nb^{5+}, Zr^{4+},Mo^{6+}, and W^{6+}, to stabilize the cubic polymorph and increase conductivity in reducing atmosphere (Figure 17b) [132, 140].

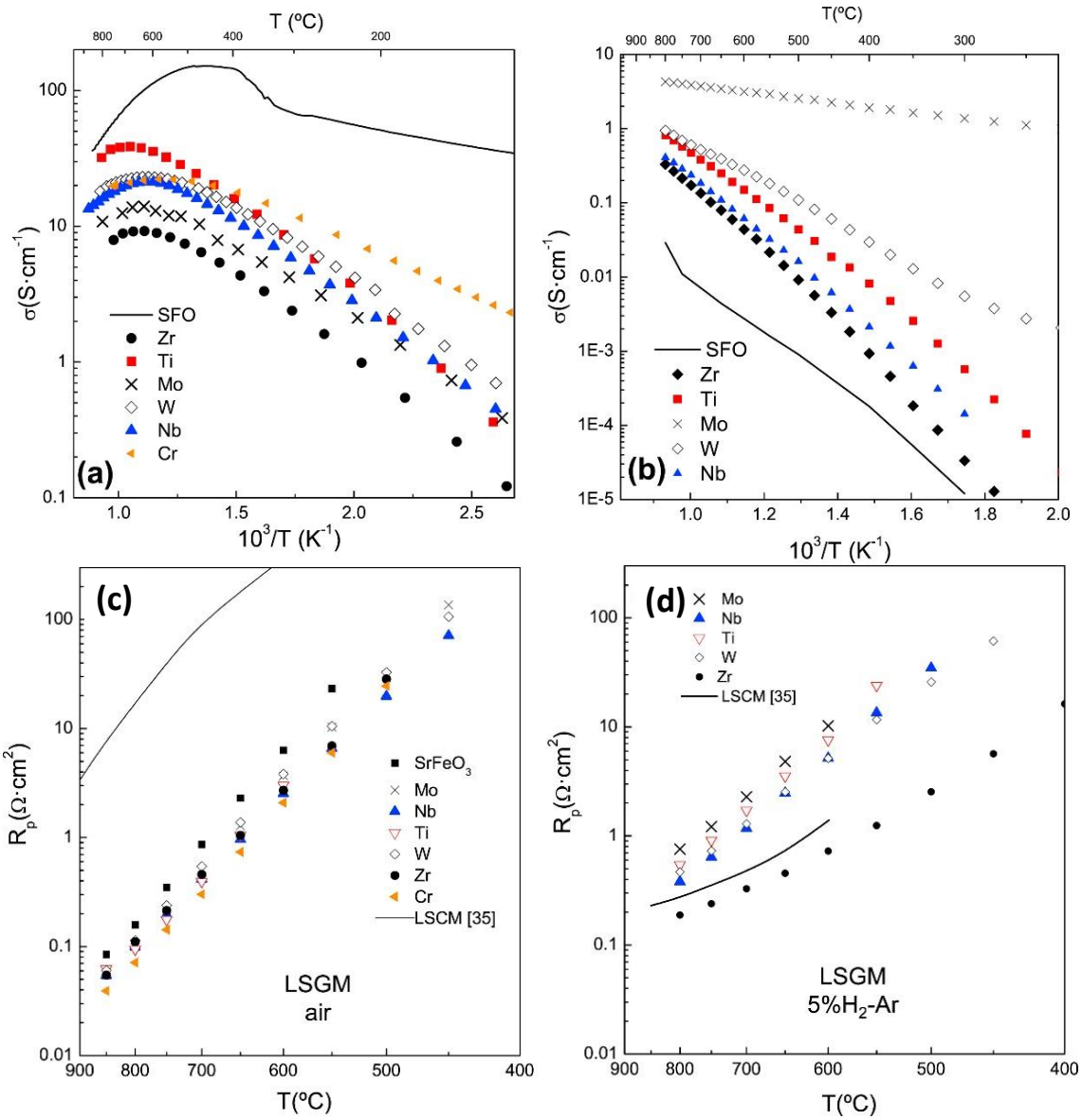

Figure 17. Arrhenius plots of the conductivity for $SrFe_{0.75}M_{0.25}O_{3-\delta}$ (M=Ti, Zr, Nb, Cr, Mo, W) series: (a) in air and (b) in 5% H_2-Ar. Temperature dependence of the R_p of $SrFe_{0.75}M_{0.25}O_{3-\delta}$ (M=Ti, Zr, Nb, Cr, Mo, W) electrodes deposited over the LSGM electrolyte in (c) air and (d) 5% H_2-Ar flow at open circuit conditions[282]. Images are reproduced from reference 282. Copyright Elsevier.

SFO-based materials doped with high valence transition metals can have beneficial effects on the electrochemical performance, making them potentially suitable for using as cathode and anode materials in symmetrical SOFC. The works on ferrite-based symmetrical fuel cell is listed in Table 1 with "&" marks.

Ti-doped SFO is also a promising material showing an R_p of 0.5 Ω cm^2 in 5% H_2–Ar and 0.1 Ω cm^2 in air at 800 °C [282]. Santos-G´omez *et al.* reported a maximum power density of 700 mW cm^{-2} at 800 °C with $Sr_{0.98}Fe_{0.8}Ti_{0.2}O_3$ symmetrical electrode[112]. Zr-doped $BaFeO_3$ (BFZ) on a LSGM (200 μm) electrolyte supported symmetrical SOFC exhibited a peak power density of 1097 mW cm^{-2} using humidified H_2 as the fuel and ambient air as the oxidant at 800 °C [139]. Mo-doped SFO perovskite structure was attractive greatly to be used as both cathode and anode in symmetrical SOFCs[129, 131, 153]: $Sr_2Fe_{1.5}Mo_{0.5}O_{6-\delta}$ exhibiting a cubic structure showed high electrical conductivity in both air and hydrogen atmospheres[129] and the Fe/Mo redox couples can be expected to remain mixed-valent in the reducing atmosphere. At 780 °C, the value of electrical conductivity reached up to 550 S cm^{-1} in air and 310 S cm^{-1} in H_2, respectively[129]. An LSGM electrolyte-supported symmetrical cell with the configuration of $Sr_2Fe_{1.5}Mo_{0.5}O_{6-\delta}$ |LSGM|& was fabricated and tested with different fuels (Figure 18). The R_p of $Sr_2Fe_{1.5}Mo_{0.5}O_{6-\delta}$ electrode in air was 0.10 Ω cm^2 while the value of R_p in wet H_2 was 0.21 Ω cm^2 at 850 °C. The maximum power densities at 900°C in wet H_2 and CH_4 were 835 and 230 mW cm^{-2}, respectively.

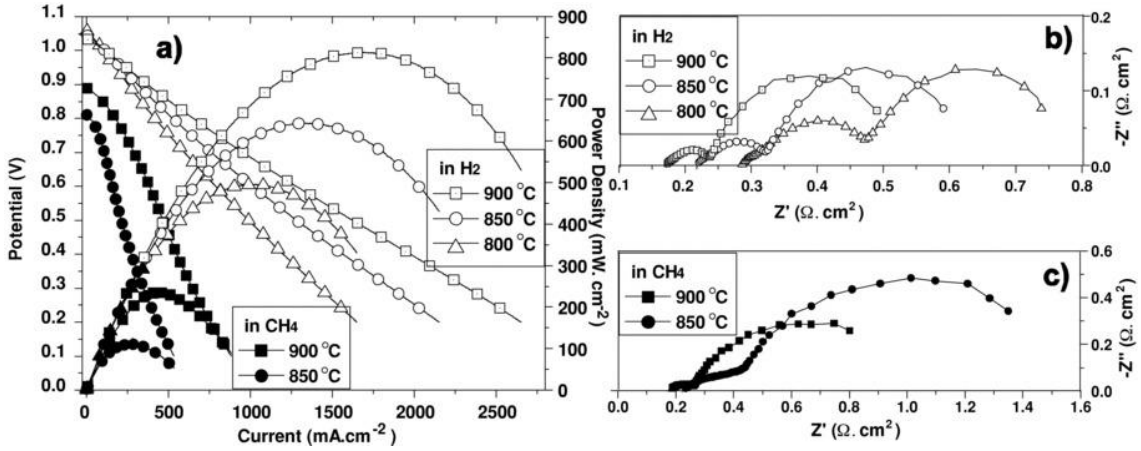

Figure 18. Performance of a symmetrical fuel cell $Sr_2Fe_{1.5}Mo_{0.5}O_{6-\delta}$ |LSGM|& with wet (3 vol. % H_2O) H_2 or CH_4 as fuel. (a) I–V and I–P curves; Impedance spectra of single cells in (b) wet H_2 and (c) wet CH_4.[129] Images were taken from reference 129. Copyright Wiley-VCH.

Ca-doping on the Sr site was found to increase the electric conductivity in humidified H_2 and a symmetrical fuel cell $Sr_{1.75}Ca_{0.25}Fe_{1.5}Mo_{0.5}O_{3-\delta}$ on LSGM electrolyte showed an

interface resistance of 0.09 and 0.2 Ω cm^2 in air and hydrogen at 800 °C [130]. Pd infiltrated $Sr_{1.9}FeNb_{0.9}Mo_{0.1}O_{6-\delta}$ was used for symmetrical electrode, but the conductivity in air was much lower than that in reducing atmosphere (1.42 x 10^{-2} S cm^{-1} vs 8.8 S cm^{-1}) [104]. The R_p values of $Sr_{1.9}FeNb_{0.9}Mo_{0.1}O_{6-\delta}$ were 0.469 and 0.353 Ω cm^2 at 800 °C in air and H_2, respectively and could be decreased significantly *via* Pd infiltration. The power output of the symmetrical cell Pd- $Sr_{1.9}FeNb_{0.9}Mo_{0.1}O_{6-\delta}$ /SDC/LSGM/& was 935.4 and 196.5 mW cm^{-2} at 850 °C in humidified H_2 and 17 vol%CH_4-83 vol% CO_2 fuel, respectively.

5.1.2 $RFeO_3$-Based Oxides (R=rare earth elements)

Apart from $AFeO_3$ (A=Sr, Ba) based perovskite, a lot of works evaluated the potential application of rare earth elements doped in A site of $RFeO_3$ as the electrodes for symmetrical SOFCs[78, 81, 82, 84, 100-103, 109, 111, 121, 137, 138, 284-286]. The substitution of rare earth elements on the A site, *i.e.* La^{3+}, Sm^{3+}, $Ce^{3+/4+}$, $Pr^{3+/4+}$ *et al.*, is one way to improve the phase stability of iron-based oxides. Ce-doped $SmFeO_3$ ($Sm_{0.95}Ce_{0.05}FeO_{3-\delta}$, SCFO) oxides have been explored as electrodes for symmetrical SOFCs[79, 111]. The partial replacement of Sm by Ce enhanced not only the phase stability, but also the electrical conductivity under reducing condition. A modest level of power density with a maximum value of 130 mW cm^{-2} was achieved at 800 °C for a 700 μm-thick YSZ electrolyte supported single cell with SCFO symmetrical electrodes. $Sm_{0.5}Sr_{0.5}FeO_{3-\delta}$ (SSF) in composite with GDC showed an R_p of 0.67 Ω cm^2 in air and 0.91 Ω cm^2 in humidified H_2 at 750 °C [78]. A peak power density of the symmetrical fuel cell was 201.74 mW cm^{-2} at 750 °C. However, it was unstable at 800 °C in the humidified H_2: the perovskite phase decomposed into Fe and R-P phase $SmSrFeO_4$.

Actually, co-doping in A-site and B-site of iron-based perovskites is also a popular strategy in designing highly active and stable electrodes for symmetrical SOFCs. $La_{0.7}Sr_{0.3}Fe_{0.9}Ni_{0.1}O_{3-\delta}$ as the electrode of symmetrical SOFCs was found to be stable in both oxidizing and moderately reducing environments, with only a minor amount of $SrLaFeO_4$ phase presenting under reducing condition[87]. At 850 °C, $La_{0.7}Sr_{0.3}Fe_{0.9}Ni_{0.1}O_{3-\delta}$-based symmetrical SOFCs illustrated excellent peak power densities not only in H_2 fuel (900 mW cm^{-2}) but also in wet CH_4/air (522 mW cm^{-2}). The stability of Sr-doped

$La_{0.6}Sr_{0.4}FeO_{3-\delta}$ was found to be conditional: oxides with 20% Sc^{3+} substitution for $Fe^{4+/3+}$ ($La_{0.6}Sr_{0.4}Fe_{0.8}Sc_{0.2}O_{3-\delta}$) were stable under H_2 at 800 °C while $La_{0.6}Sr_{0.4}Fe_{0.8}Sc_{0.1}O_{3-\delta}$ could be reduced to a composite containing a small amount of $LaSrFeO_4$ [124].

Haag *et al*. reported that rhombohedral $LaSr_2Fe_2CrO_{9-\delta}$ maintained the crystal structure after being reduced at 750 ◦C while a small $LaSrFeO_4$ peak presented for $LaSr_2Fe_2CrO_{9-\delta}$ after reduced at 800 ◦C [118, 287]. The electrical conductivities of LSFCr were 65∼ 75 S cm^{-1} at 500-800 °C in air but, as these are p-type, decreased to 0.01 S cm^{-1} at 550 °C and to 0.16 S cm^{-1} at 800 °C when in H_2. $La_{0.3}Sr_{0.7}Fe_{1-x}Cr_xO_{3-\delta}$ (x = 0–0.3) is used within a symmetrical SOFC[288]. The oxide with the highest Cr content $La_{0.3}Sr_{0.7}Fe_{0.7}Cr_{0.3}O_{3-\delta}$ showed an R_p of 0.1 Ω cm^2 in air and 0.4 Ωcm^2 in wet (ca. 3%H_2O) H_2 at 800 °C. The increasing Cr doping inhibited the formation of brownmillerite $LaSr_2Fe_3O_8$ in $La_{0.3}Sr_{0.7}FeO_3$, but $La_{0.3}Sr_{0.7}Fe_{0.7}Cr_{0.3}O_{3-\delta}$ still showed a slow decomposition to produce trace R-P $LaSrFeO_4$ plus Fe^0 that can be reversibly incorporated into the perovskite lattice during the reoxidation. The cell based on $La_{0.3}Sr_{0.7}Fe_{0.7}Cr_{0.3}O_{3-\delta}$|LDC|LSGM|& showed 30 % power drop within 48 h at 800 °C which was possibly attributed to the $LaSrGa_3O_7$ insulating phase, formed by cation interdiffusion at the LSGM/LDC interface under polarized conditions (Figure 19).

LSCF whilst an efficient cathode for SOFCs[289], is believed to be unstable under reducing atmosphere for a symmetrical SOFC at a high temperature, but an LSCF|YSZ|& micro-symmetrical SOFC was fabricated successfully to work at 545 °C with a power of 210 mW cm^{-2}. The phase stability of LSCF will be improved *via* B-site doping, such as Mo and Nb[97, 102, 138]. A-site deficient $(La_{0.6}Sr_{0.4})_{1-x}Co_{0.2}Fe_{0.6}Nb_{0.2}O_{3-\delta}$ (x= 0, 0.05 and 0.10) in a symmetrical SOFC[97] displayed good structural stability both in cathode and anode conditions and the electrochemical performance of electrode improved *via* the introduction of A-site deficiency to increase the oxygen-vacancy concentration and a weaker B-O bonding energy promoting the reduction of Fe ions. At 850 °C, the maximum power density of a LSGM electrolyte-supported single cell with $(La_{0.6}Sr_{0.4})_{0.9}Co_{0.2}Fe_{0.6}Nb_{0.2}O_{3-\delta}$ symmetrical electrodes was 651 mW cm^{-2} operating in H_2 fuel and was compatible with the fuel such as syngas, ethanol, and CH_4.

$La_{0.6}Sr_{0.4}Co_{0.2}Fe_{0.7}Mo_{0.1}O_{3-\delta}$ symmetrical electrode was synthesized by solid-state reaction through doping Mo at the B site of the LSCF cathode[136]. XPS revealed that the ratios of Fe^{4+}/Fe^{3+} were 1.2:1 for LSCF and 1:3.3 for $La_{0.6}Sr_{0.4}Co_{0.2}Fe_{0.7}Mo_{0.1}O_{3-\delta}$ for the reason of electroneutrality. The R_p of $La_{0.6}Sr_{0.4}Co_{0.2}Fe_{0.7}Mo_{0.1}O_{3-\delta}$ in air (0.041 Ω cm^2) was quite lower than that in H_2 (0.266 Ω cm^2) at 800 °C and the initial performance of the symmetrical fuel cell was found to be stable in either H_2 or liquefied petroleum gas[138].

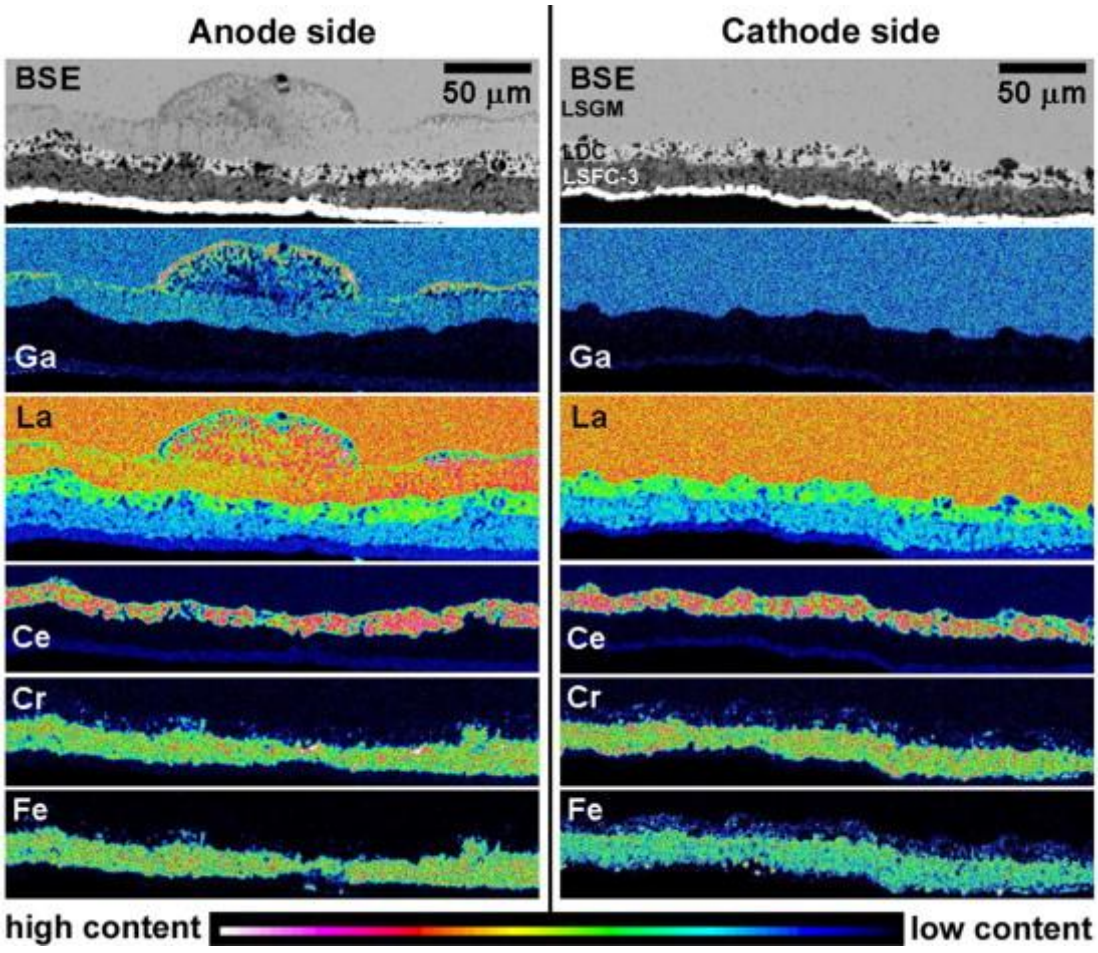

Figure 19. Back-scattering electron images and element maps for Ga, La, Ce, Cr and Fe at the LSGM|LDC| $La_{0.3}Sr_{0.7}Fe_{0.7}Cr_{0.3}O_{3-\delta}$ interface at both the anode and cathode side of a symmetrical SOFC after 350 h in wet-H_2 at 800 °C [288]. Images are reproduced from reference 288. Copyright Elsevier.

$PrBaMn_2O_{5+\delta}$ with Pr and Ba ordering was reported to be coke resistant anode showing high MIEC under reducing atmosphere[25]. $PrBaMn_2O_{5+\delta}$ was synthesized *via* the hydrogen reduction of oxygenated $PrBaMn_2O_{6-\delta}$ containing hexagonal $BaMnO_3$ as a secondary

phase as a result of the Mn^{4+} in air. $PrBaMn_{1.5}Fe_{0.5}O_{5-d}$ (PBMFO) showed good stability in both oxidizing and reducing atmospheres, and high electrical conductivities (112.5 and 7.4 S cm^{-1} at 800 °C in air and 5% H_2/Ar, respectively)[290]. A single cell based on PBMFO|LSGM(520 μm)|PBMFO exhibited a maximum power density of 0.54 W cm^{-2} at 800 °C and 0.34 W cm^{-2} at 850 °C using humidified H_2 (3% H_2O) and humidified CH_4 as fuel, respectively. $PrBa(Fe_{0.8}Sc_{0.2})_2O_{5-\delta}$ and $(PrBa)_{0.95}(Fe_{0.9}Mo_{0.1})_2O_{5+\delta}$ with a well-formed tetragonal structure were applied as both cathode and anode in the symmetrical SOFCs[291]. $PrBa(Fe_{0.8}Sc_{0.2})_2O_{5-\delta}$ retained superior structural stability after annealing in 5% H_2/N_2 and wet H_2 for 10 h at 800 °C. The R_p values were only 0.05 Ω cm^2 and 0.18 Ω cm^2 at 800 °C in air and humidified H_2 (3wt% H_2O), respectively. A LSGM electrolyte-supported cell with $PrBa(Fe_{0.8}Sc_{0.2})_2O_{5-\delta}$ (Figure 20) as symmetrical electrodes exhibited a peak power density of 921 mW cm^{-2} at 850 °C and 275 mW cm^{-2} at 900 °C using H_2 and CH_4 as a fuel, respectively [291]. The excellent cyclic stability is obtained on the symmetrical cell using the wet H_2 and the ambient air in the anode chamber at 750 °C.

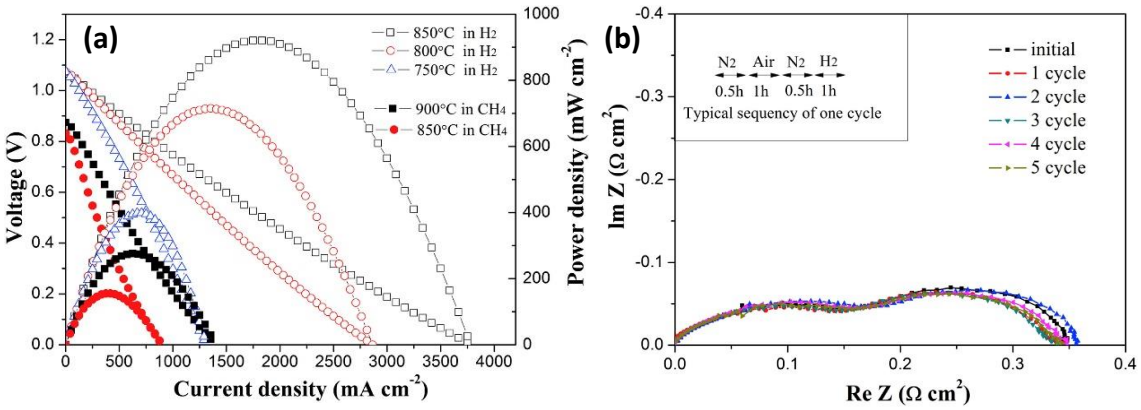

Figure 20. (a) Electrochemical performance of a symmetrical cell with $PrBa(Fe_{0.8}Sc_{0.2})_2O_{5-\delta}$ electrode under wet H_2 and wet CH_4 as fuels at different temperatures. (b) Polarization impedance of single cell at 750 °C after each cycling test. [291] Images were taken from reference 291. Copyright Elsevier.

Incorporation of ionic conductive oxides or metal catalysts into iron-based perovskites is also an effective strategy to improve the catalytic activity of ORR and FOR reactions in symmetrical SOFCs[86, 99]. Composite electrodes prepared *via* the infiltration of the $La_{0.6}Sr_{0.4}Fe_{0.9}Sc_{0.1}O_{3-\delta}$ perovskites into porous LSGM skeleton were found to show very

small R_p: 0.015 Ω cm^2 in air and 0.29 Ω cm^2 in hydrogen at 800 °C. The cell with thin LSGM electrolyte and symmetrical $La_{0.6}Sr_{0.4}Fe_{0.9}Sc_{0.1}O_{3-\delta}$/LSGM electrode prepared *via* infiltration showed a maximum power density of 0.56 W cm^{-2} in wet H_2 (3% H_2O) at 800 °C. [124] $La_{0.6}Sr_{0.4}Fe_{0.9}Sc_{0.1}O_{3-\delta}$ oxide was impregnated as symmetric electrode catalysts into porous 430L substrates and YSZ backbones and the maximum power density of the cell was 0.65 W cm^{-2} measured at 800 °C [292]. $La_{0.6}Ca_{0.4}Fe_{0.8}Ni_{0.2}O_{3-\delta}$ (LCFN)-$Sm_{0.2}Ce_{0.8}O_{1.9}$ (SDC) composite was prepared *via* infiltration and physical mixing methods[86] and the Fe-Ni bimetallic nanoparticles exsolved through the *in-situ* growth was found to induce an enhanced hydrogen oxidation reaction. In the meantime, the chemical activity towards ORR in air was further improved by infiltration of SDC nanoparticles. A symmetrical SOFC with nano-sized $La_{0.6}Ca_{0.4}Fe_{0.8}Ni_{0.2}O_{3-\delta}$–SDC composite electrode was prepared *via* infiltration to enhance the performance compared with the one with physically mixed composite electrode [85]. ASRs of the nano $La_{0.6}Ca_{0.4}Fe_{0.8}Ni_{0.2}O_{3-\delta}$ – infiltrated SDC cathode was only 0.009 Ω cm^2 at 750 °C in air. Using H_2 as a fuel gas, the maximum power density of the cell exhibited a value of 507 mW cm^{-2} at 800 °C. The authors also tested the cell using a mixture CH_4-O_2 (molar ratio of 2 : 1) as fuel and the maximum power density reached 350 mW cm^{-2} at 800 °C. $Sm_{0.8}Sr_{0.2}Fe_{0.8}Ti_{0.15}Ru_{0.05}O_{3-\delta}$ was found to be stable at 800 °C in wet H_2 and the engineering of A-site deficiency as in $Sm_{0.7}Sr_{0.2}Fe_{0.8}Ti_{0.15}Ru_{0.05}O_{3-\delta}$ greatly enhanced the power output of the symmetrical SOFC as a result of the exsolution of Ru^0 in the latter[110]. $La_{0.7}Sr_{0.3}Fe_{0.7}Ga_{0.3}O_{3-\delta}$ oxide with modest TEC 13.79 ppm K^{-1} in air and 13.88 ppm K^{-1} in 5% H_2 at 200–800 °C was stable as the electrode material for a symmetrical SOFC using H_2 containing 100 ppm H_2S and humidified 17CH_4-83CO_2 as the fuel[105].

5.1.3 R-P phase oxides for a symmetrical SOFC

In the Section 2.2, quite a few perovskite oxides were found to decompose into stable R-P phase ferrites along with the formation of metal catalysts, indicating that the latter could stable in reducing atmosphere. R-P phase oxides, such as A_2NiO_4 and A_2CoO_4, are good candidates as oxygen electrode due to the interstitial sites in the rock-salt AO layers which can accommodate excess oxide ions assisting their high oxygen-diffusion and

surface-exchange coefficients[293-296], and thus R-P phase ferrites can be easily fitted into the symmetrical SOFCs.

The simplest R-P phase oxide, K_2NiF_4-type crystal structure has been found to have much better stability than simple ferrite perovskites under reducing conditions[27]. $LaSrFeO_{4-\delta}$ showed reasonable stability according to low oxygen release down to oxygen partial pressures of 10^{-10} Pa at a temperature of 800 °C in $Ar/H_2/H_2O$ [297]. $La_xSr_{2-x}FeO_4$ (x=0.6-1.4) showed a good stability in 5% H_2/Ar at 850°C for 20 h and has been evaluated as electrodes for symmetrical SOFCs[298]. The electrical conductivity of $La_{0.6}Sr_{1.4}FeO_4$ was 23 S cm^{-1} at 800 °C in air, but the highest electrical conductivity was only 0.20 S cm^{-1} in 5% H_2/Ar. Meanwhile, the R_p of $La_xSr_{2-x}FeO_4$ showed better catalytic activity toward ORR than that of H_2 oxidation reaction. At 800 °C, a cell with LSGM electrolyte and $La_{0.8}Sr_{1.2}FeO_4$-LSGM mixture as symmetrical electrodes showed a maximum power density of 73 mW cm^{-2}. $LaSrCo_{0.5}Fe_{0.5}O_4$ was stable under reducing condition (10% H_2/N_2) up to 800 °C forming a nonstoichiometric $LaSrCo_{0.5}Fe_{0.5}O_{3.75}$ phase[299], but the $La_{0.8}Sr_{1.2}Fe_{0.9}Co_{0.1}O_{4-\delta}$ (Figure 21) as electrodes for symmetrical SOFCs showed a small Co^0 peak after the reduction at 850 °C for 20 h in a flow of 5% H_2/Ar [300]. Although nano-sized Co^0 particles (~ 10 nm) exsolved on the surface of the reduced sample, the oxygen non-stoichiometry implied the remnant R-P phase remained stable, even after five redox cycles between air and 5% H_2. The Co doping on the Fe site increased the electrical conductivity and electrocatalysis for FOR in reducing atmosphere, which is similar to a perovskite material, as a result of the exsolved metallic particles.

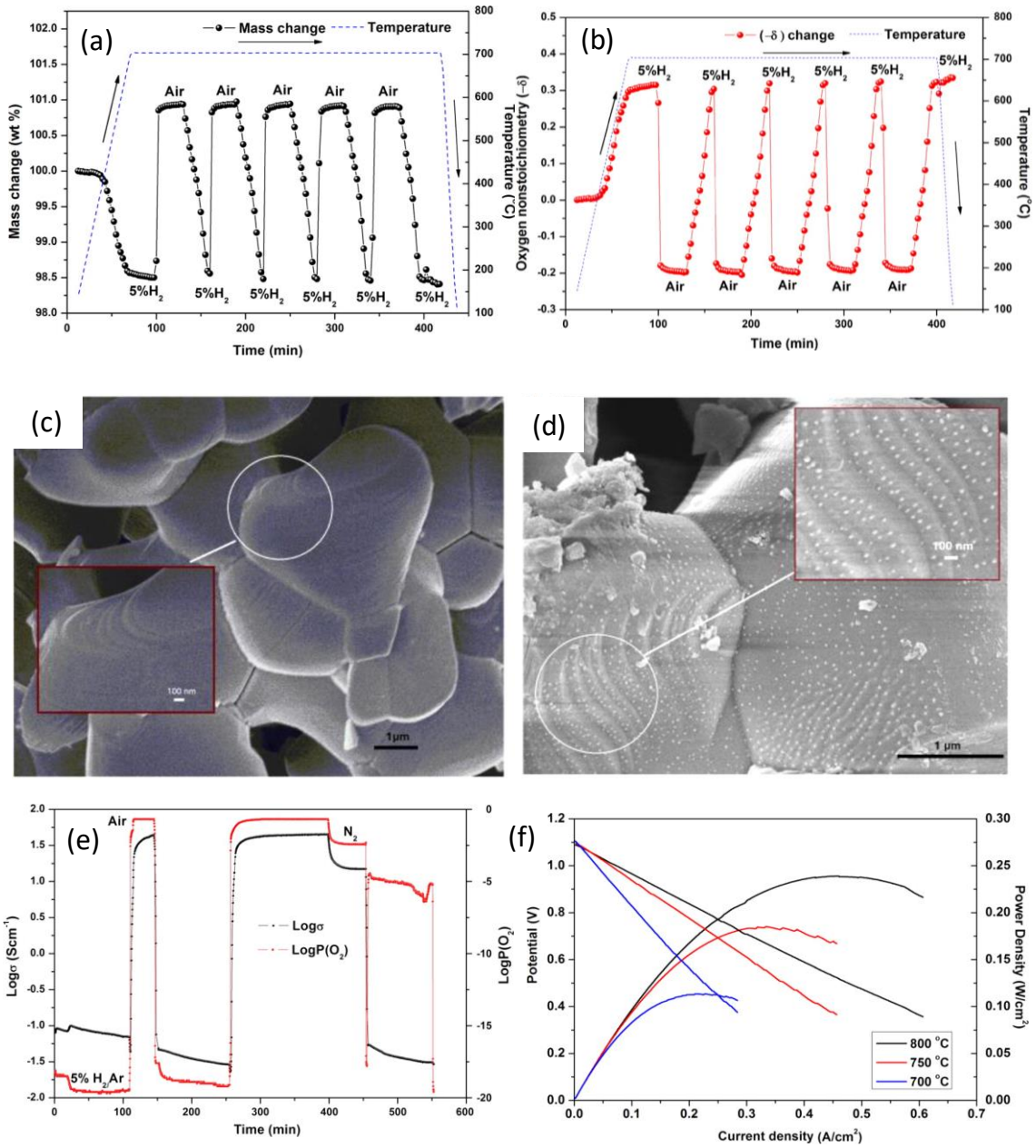

Figure 21. (a) Isothermal TG and (b) oxygen nonstoichiometry curves for $La_{0.8}Sr_{1.2}Fe_{0.9}Co_{0.1}O_{4-\delta}$ treated in different atmospheres. SEM images of (c) as-synthesized $La_{0.8}Sr_{1.2}Fe_{0.9}Co_{0.1}O_{4-\delta}$ and (d) the reduced $La_{0.8}Sr_{1.2}Fe_{0.9}Co_{0.1}O_{4-\delta}$ powders. (e) Evolution with time of the conductivity of $La_{0.8}Sr_{1.2}Fe_{0.9}Co_{0.1}O_{4-\delta}$ at 800 °C under various atmospheres. (f) I-V curves and power density versus current density for symmetrical SOFCs with $La_{0.8}Sr_{1.2}Fe_{0.9}Co_{0.1}O_{4-\delta}$/CGO electrode measured in humidified H_2 (3 vol % H_2O)

as fuel at 700−800 °C [300]. Images are reproduced from reference 300. Copyright American Chemical Society.

5.2 Symmetrical solid oxide electrolysis cells

As mentioned previously, Fe-based perovskite oxides are candidates as oxygen electrodes for SOECs, thus efficient electrolysis of pure CO_2 has been achieved in symmetrical SOECs with Fe-based perovskite electrodes[204, 212]. The Fe-based oxides for symmetrical SOEC are summarized in Table 2.

Table 2. Recent research on the Fe-based perovskite oxides used for symmetrical electrodes in SOECs.

Cathode|buffer|electrolyte|&[a]	Current density (A cm^{-2}) @bias @ temperature	Feeding gas	Ref.
$La_{0.3}Sr_{0.7}Fe_{0.7}Ti_{0.3}O_{3-\delta}$ |YSZ(700)|&	0.52 @ 2.0 V @ 800°C	CO_2	204
$La_{0.6}Sr_{0.4}Fe_{0.9}Mn_{0.1}O_{3-\delta}$/GDC|GDC |YSZ(200)|&	1.10@2.0 V @ 850 °C	CO_2	301
$La_{0.3}Sr_{0.7}Fe_{0.7}Cr_{0.3}O_{3-\delta}$|GDC|YSZ(300)|&	0.28 @ 1.5V @800 °C	10%CO-CO_2	205
$La_{0.6}Sr_{0.4}Fe_{0.8}Ni_{0.2}O_{3-\delta}$|GDC|YSZ(400)|&	1.03 @ 2.0 V @ 800 °C	CO_2	302
$La_{0.6}Sr_{0.4}Fe_{0.8}Ni_{0.2}O_{3-\delta}$|GDC|YSZ(500)|&	1.42 @2.0V @850 °C	CO_2	303
$La_{0.4}Sr_{0.6}Co_{0.2}Fe_{0.7}Nb_{0.1}O_{3-\delta}$ |GDC|YSZ(150)|&	0.64 @1.3V@ 850 °C	75% CO_2-15% H_2O-10% H_2	231
$La_{0.5}Sr_{0.5}Fe_{0.9}Nb_{0.1}O_{3-\delta}$ |LSGM(250)|&	1.46 @ 1.3V @800 °C	20%H_2O+CO_2	304

$Pr_{0.95}Ba_{0.95}(Fe_{0.9}Mo_{0.1})_2O_{5+\delta}$|LSGM(450)|&	0.51@1.3V @800 °C	3% H_2O–97% H_2	305
Sr_2FeMoO_6|LSGM(15)|&	1.24@1.5V @800 °C	CO_2	212
$Sr_2Fe_{1.5}Mo_{0.5}O_{6-\delta}$/$Sm_{0.2}Ce_{0.8}O_{1.9}$|LSGM(502)|&	0.73@1.3V @800 °C	H_2O+CO_2	229
$Sr_2Fe_{1.5}Mo_{0.5}O_{6-\delta}$|LSGM(502)|&	0.88@1.3V@900 °C	60%H_2O +H_2	306

SOECs with symmetrical $La_{0.3}Sr_{0.7}Fe_{0.7}Ti_{0.3}O_3$ electrodes for electrolysis of pure CO_2 at 800 °C showed an R_p of 0.08 Ω cm^2 and current density of 521 mA cm^{-2} at 2.0 V. [202] $La_{0.6}Sr_{0.4}Fe_{0.9}Mn_{0.1}O_{3-\delta}$ with surface area of 22.93 m^2/g was used as the symmetrical electrodes for a high-temperature electrolysis of pure CO_2 [301]. The electrolysis cell on a YSZ electrolyte support with GDC blocking layer showed an R_p of 0.068 Ω cm^2 and a current density of 1.1 A cm^{-2} at 800 °C under an operating voltage of 2.0 V. Ni-doping in $La_{0.6}Sr_{0.4}FeO_{3-\delta}$ ($La_{0.6}Sr_{0.4}Fe_{0.8}Ni_{0.2}O_{3-\delta}$) increased the oxygen vacancies and effectively enhanced the chemical adsorption ability of CO_2 as symmetrical cell for electrolysis of pure CO_2 [302, 303]. Although the main perovskite phase was retained after pure CO_2 treatment for 24 h, $SrCO_3$ secondary phase emerged in X-ray diffraction (XRD) pattern after electrolysis at 850 °C [302]. The maximum current density reached was 1.42 A cm^{-2} at 2.0 V for CO_2 electrolysis with high Faraday efficiency if *in-situ* exsolved Ni-Fe nanoparticles were initiated on the cathode side under a pre-reduction in H_2 [303]. Several works were focused on Mo-doped ferrite perovskite for both cathode and anode simultaneously in SOECs[212, 229, 305]. For example, a symmetrical cell with Sr_2FeMoO_6 infiltrated into the symmetric tri-layer structure of porous-LSGM exhibited a current density of 1.24 A cm^{-2} at 1.5 V at 800 °C for pure CO_2 electrolysis. Fe-based perovskites have also been applied as symmetrical electrodes for co-electrolysis of CO_2 and H_2O in SOECs [196]. A cell consisting of a 150-μm YSZ electrolyte and 15-μm GDC buffer layers and $La_{0.4}Sr_{0.6}Co_{0.2}Fe_{0.7}Nb_{0.1}O_{3-\delta}$ symmetrical electrodes showed a current density of 0.638 A

cm^{-2} at 850 °C under an applied voltage of 1.3 V using a mixture of 75% CO_2-15% H_2O-10% H_2 at the fuel electrode[231].

Because the cathode and anode of a symmetrical SOEC can survive in reducing atmosphere and fuel (e.g. H_2, C and CH_4) can be introduced in the anode chamber to decrease the external voltage that is required to initiate the dissociation of H_2O or CO_2 on the cathode[307]. The introduction of H_2 on the anode will not be meaningful in terms of energy efficiency, but the introduction of widely available natural gas will decrease the consumption of electricity and increase the overall efficiency of an SOEC to 70% from 32% of a conventional SOEC.[308]

The first symmetrical CH_4-assisted SOEC (Ce/Cu/Co/YSZ|YSZ(50 μm)|&) prepared *via* impregnation showed a current density 0.2 A cm^{-2} at 0.4 V for the dissociation of steam [309]. The overall reaction for CH_4-assisted electrolysis of H_2O is the same as the one for methane steam reforming ($CH_4(g)+ H_2O(g) = 3H_2(g)+ CO(g)$), but the former can produce pure H_2 on the cathode that can be used for PEMFCs.

A symmetrical electrolysis cell with (La, Sr)(Co,Fe,Mn)O_3 electrode was proposed for the oxidation of methane on the anode [307], further demonstrations were on symmetrical cell based on Mo-doped $SrFeO_3$ for the partial oxidation of CH_4 to produce mixed CO and H_2.[307] Ni infiltration into $Sr_2Fe_{1.5}Mo_{0.5}O_{6-\delta}$-SDC anode was found to increase the current density of the CH_4-assisted electrolyser [310]. A symmetrical cell with "$Sr_2Fe_{1.5+x}Fe_{0.5}O_{6-\delta}$" ($0<x<0.1$) anode [311] was found to be efficient in producing C_2 ethylene from CH_4. Solid carbon deposited on the anode of an $Sr_2Fe_{1.5}Mo_{0.5}O_{6-\delta}$/SDC|LSGM (500 μm)|& was also effective in decreasing the potential for the electrolysis of CO_2/H_2O on the cathode. As the oxidation of O^{2-} from the cathode is proposed to take place on the region of electrolyte/anode interface, the chemical or electrochemical nature of the fuel-assisted electrolysis is not very clear. Because the build-up of oxygen pressure on the interface of the anode/electrolyte was found to be one of the reasons for the delamination of an SOEC [312], the introduction of fuel in the anode chamber could also affect the long-term stability of the anode.

5.3 Reversible RSOCs

The coupling of an SOFC and an SOEC for energy storage using the conversion between H_2O, CO_2 feedstock and H_2, CO fuel could be performed on the same cell at different operating modes or separate cells. The advantage of an RSOC that can operated in fuel-cell or electrolysis mode is obvious because it can reduce the cost and space, but it at the same time puts extra demand for the material to reduce the cell loss. The working progress and development of RSOC have been reviewed very recently by Mogensen *et al.*[54], and we focus more on the iron-based electrodes for RSOC. As the ferrite oxygen electrode and fuel electrode have been discussed previously, the work on ferrite electrodes is basically more on demonstration.

The performance of oxygen electrode would vary under a cathodic or anodic current in an SOFC and SOEC mode, respectively[313, 314]. LSCF and $La_{0.6}Sr_{0.4}Fe_{0.8}Ni_{0.2}O_{3-\delta}$ perovskites[315, 316] are used as oxygen electrodes for RSOCs. Specifically, $La_{0.6}Sr_{0.4}Fe_{0.8}Ni_{0.2}O_{3-\delta}$ exhibited good performance in SOFC as well as SOEC mode. In SOFC mode, the single cell using $La_{0.6}Sr_{0.4}Fe_{0.8}Ni_{0.2}O_{3-\delta}$ as oxygen electrode showed the maximum power density of 961 mW cm^{-2} and R_p of 0.142 Ω cm^2 at 800 °C, while in SOEC mode, the hydrogen production rate of RSOC was up to 1348.5 mL cm^{-2} h^{-1}.

Symmetrical SOCs with ferrite electrodes have also been demonstrated as RSOCs for power generation and CO_2 reduction. A single cell with the LSFCr $La_{0.3}Sr_{0.7}Fe_{0.7}Cr_{0.3}O_{3-\delta}$|GDC|YSZ|GDC|$La_{0.3}Sr_{0.7}Fe_{0.7}Cr_{0.3}O_{3-\delta}$ symmetrical configuration[205] was examined as a CO/CO_2 fuel electrode material both in SOFC mode and SOEC mode respectively. The cell exhibited a decent electrochemical performance during both SOEC mode and SOFC mode. Doping CeO_2 into $La_{0.3}Sr_{0.7}Ti_{0.3}Fe_{0.7}O_{3-\delta}$ porous backbone can be used as fuel electrode in different CO/CO_2 atmospheres under reversible SOFC and SOEC operating conditions[107]. At 850 °C, a current density of 3.56 A cm^{-2} was obtained at 2.0 V in 50% CO+ 50% CO_2 in SOEC mode, while the maximum power density was 437 mW cm^{-2} at 800 °C in 70% CO+ 30% CO_2 in SOFC mode. A slow degradation in both SOFC and SOEC modes was observed during the reversible operation. Bian *et al.* [304] found that $La_{0.5}Sr_{0.5}Fe_{0.9}Nb_{0.1}O_{3-\delta}$ perovskite oxide used as a symmetric electrode for both SOFCs and H_2O/CO_2 co-electrolysis cells

showed a peak power density of 1157 mW cm^{-2} (Figure 22) at 850 °C in SOFC mode and a current density of 1464 mA cm^{-2} was obtained at 1.3 V in SOEC mode. The CO/H_2 ratio in output gas was ~ 1.2-1.3 and was insensitive to the applied current density. The cell can electrolyze CO_2 or CO_2/H_2O at high Faraday efficiency (96.5%) without carbon deposition.

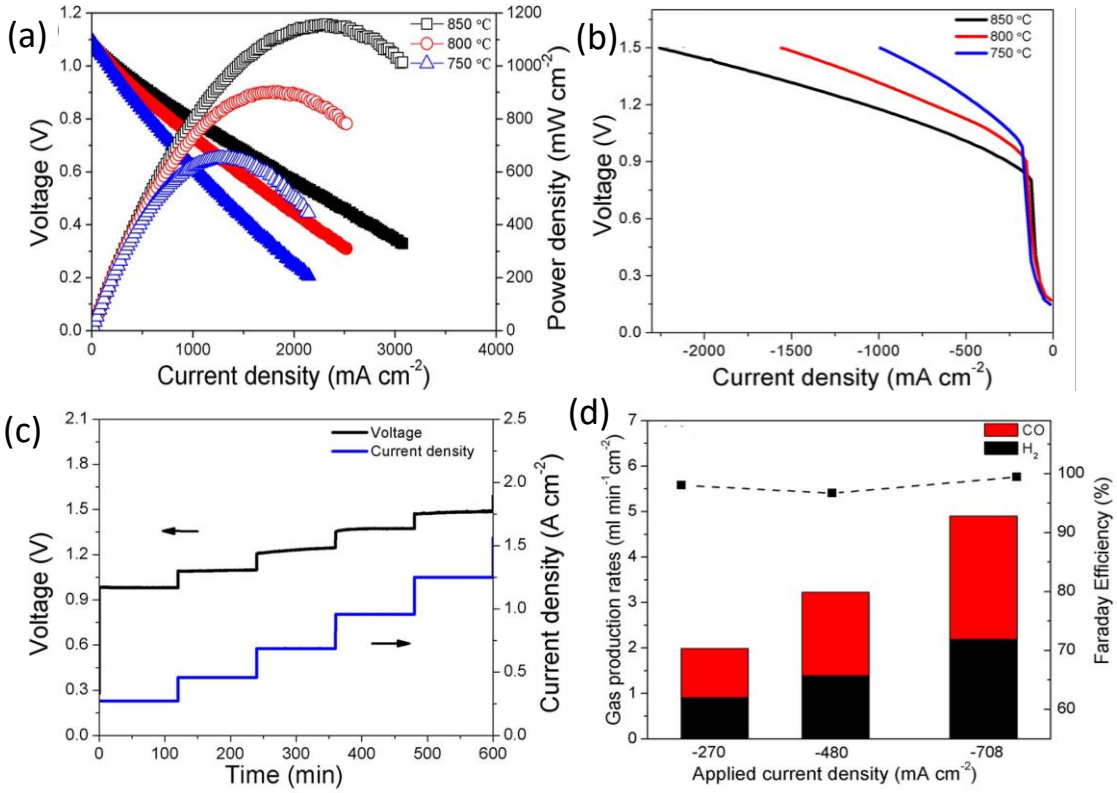

Figure 22. I-V curves of the $La_{0.5}Sr_{0.5}Fe_{0.9}Nb_{0.1}O_{3-\delta}$ symmetric cell with LSGM electrolyte (250 μm in thickness) in SOFC mode (a) and SOEC mode (b). (c) Short-term stability of the cell potential at various applied current densities under co-electrolysis operation with CO_2-20 vol% H_2O at 800 °C. (d) CO and H_2 production rates and corresponding faradaic efficiency at several applied current densities[304]. Images are reproduced from reference 304. Copyright the Electrochemical Society.

Summary and outlook

The need to decrease the cost and impact on environment is a huge opportunity to promote the industrialization of SOCs. Iron is one of the most earth-abundant and available elements. Iron-based materials have been selected to fabricate key components

of SOFC and SOEC for several decades. The stability and "flexibility" of Fe-O bond allow for efficient doping of other highly active elements in FeO_6 octahedra. It also provides adjustable conductivity due to the multiple valence states and coordination number changes of Fe in iron-based oxides. The interesting interaction of Fe-O brings many sectors to design new iron-based materials. In addition to academic research, it can be found that iron-based materials are also applied in commercial electrochemical devices or stacks. These motivate the extensive use of iron-based materials in the future.

Iron-based alloys can be used as the support for a fuel cell to provide mechanical strength and electronic conduction, while iron-based oxides can be used for either fuel electrode or oxygen electrode because they are more reducible than chromite and titanate in creating MIEC and more stable than cobaltite or manganite in reducing atmosphere. Iron-based oxides attract increasing attention for SOCs due to their variable oxygen stoichiometries in oxidizing and reducing atmosphere, providing the opportunity to generate Fe^0 metals/alloys for boosted electrocatalysis. Generally, replacing of ca. 20% $Fe^{4+/3+}$ in a perovskite with stable cations, such as Zr^{4+}, Ti^{4+}, Cr^{3+}, Ga^{3+}, is able to prevent the decomposition or formation of brownmillerite in fuel condition, while the substitution with Ni^{2+}, Co^{3+} for $Fe^{3+/4+}$ is able to cause the exsolution metal catalyst to enhance the adsorption and dissociation processes in FOR. Iron-based oxides also provide the opportunities for tunable properties to reach the balance between TEC and MIEC *via* the doping strategy since Fe^{4+} in a perovskite can be reduced thermally in air for chemical expansion while Fe^{3+} is fairly stable. Moreover, the abundant valence states of Fe in ferrites demonstrate great potential application as catalysts in a wide range of oxygen partial pressures. All these properties dictated by the thermodynamics of valency energy of Fe-O bonding provide iron-based materials the opportunities to be used for anode and cathode of an SOFC or SOEC.

Recent development in SOC also provides the opportunities for new electrochemical syntheses: e.g. $Pr_{0.4}Sr_{0.6}Co_{0.2}Fe_{0.7}Mo_{0.1}O_{3-\delta}$, $(La_{0.6}Sr_{0.4})_{0.95}Fe_{0.8}Ni_{0.1}Mo_{0.1}O_{3-\delta}$ and $Pr_{0.6}Ba_{0.4}Fe_{0.8}Cu_{0.2}O_{3-\delta}$ have been used for the electrochemical production of ethylene from ethane in a protonic SOC at 750 ^oC and ammonia at low temperature, respectively[317-

[319]. Along with the development of protonic conducting SOCs operating at low temperatures[320-322], the special properties of iron-based materials will find more opportunities to be used to balance the stability and performance, especially in symmetrical cells[139, 323].

Although high performance has been achieved using iron-based electrodes, there are several challenges remaining to be addressed. While the development of metal-supported SOC can provide a thin electrolyte to reduce the ohmic resistance at lower temperatures, the ferrite oxides with low melting points are very difficult to be used as supports unless costly deposition techniques were used to prepare thin electrolyte[143]. The reactivity of ferrite with the popular zirconia normally needs to be addressed by the blocking layer to inhibit the unexpected reaction, while the interfacial stability at the LSGM/ferrite perovskite needs to be monitored in longer times. The development of ferrite electrocatalysts was confined mainly on perovskites, and the development of other types of oxides was demanded to reduce the use of costly rare earth elements or mobile alkaline earth elements[324]. It is significant to clarify the stability and controlled phase evolution of iron-based oxides as fuel electrode under long-term operation, especially in pure hydrogen or hydrocarbon at high temperatures. Combined *in-situ* operando characterization techniques (e.g. XRD, Raman spectroscopy, XPS) and the theoretical simulation could give a comprehensive analysis of the kinetic and thermodynamic behavior of iron-based oxides. Although nano-sized metallic particles can be exsolved from iron-based oxides to enhance the electrochemical activity, future studies may focus on pursuing *in-situ* growth on various exsolved nanoparticles or alloy nanoparticles, which can be used as high-performance catalysts for mixed gases as fuels. Overall, iron-based materials have showed great potential application in SOC and are related to interesting area, allowing an increasing commercialization of these energy conversion technologies in the near future.

Acknowledgment

We would like to acknowledge the support from the Natural Science Foundation of China (NSFC, 51702264, 41371275, 51877173, 51737011), the Fundamental Research Funds for

the central universities (XDJK2020B066; SWURC2020002) and EPSRC (EP/R023522/1, EP/P024807/1). C.N. also thanks the support from Bayu Young Scholar.

TOC image

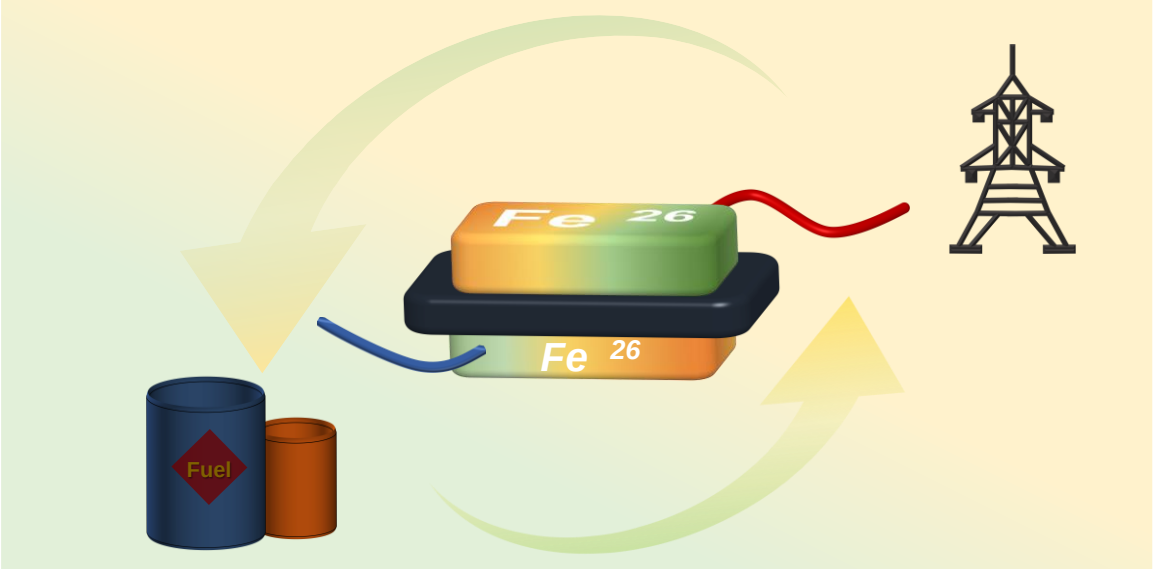

References

1. I. EG&G Technical Services, *Fuel Cell Handbook (Seventh edition)* West Virgina, 2004.
2. B. C. Steele and A. Heinzel, *Nature*, 2001, **414**, 345-352.
3. N. Q. Minh, *J. Am. Ceram. Soc.*, 1993, **76**, 563-588.
4. A. Atkinson, S. Barnett, R. J. Gorte, J. T. S. Irvine, A. J. McEvoy, M. Mogensen, S. C. Singhal and J. Vohs, *Nat. Mater.*, 2004, **3**, 17-27.
5. P. Boldrin and N. P. Brandon, *Nat. Catal.*, 2019, **2**, 571-577.
6. S. H. Jensen, C. Graves, M. Mogensen, C. Wendel, R. Braun, G. Hughes, Z. Gao and S. A. Barnett, *Energy Environ. Sci.*, 2015, **8**, 2471-2479.
7. T. M. Gür, *Energy Environ. Sci.*, 2018, **11**, 2696-2767.
8. J. C. Ruiz-Morales, D. Marrero-Lopez, J. Canales-Vazquez and J. T. S. Irvine, *RSC Adv.*, 2011, **1**, 1403-1414.
9. R. J. Gorte and J. M. Vohs, *Annu. Rev. Chem. Biomol.*, 2011, **2**, 9-30.
10. J. T. S. Irvine, D. Neagu, M. C. Verbraeken, C. Chatzichristodoulou, C. Graves and M. B. Mogensen, *Nat. Energy*, 2016, **1**, 15014.
11. Z. Gao, L. V. Mogni, E. C. Miller, J. G. Railsback and S. A. Barnett, *Energy Environ. Sci.*, 2016, **9**, 1602-1644.
12. E. D. Wachsman and K. T. Lee, *Science*, 2011, **334**, 935-359.
13. B. X. Li, S. He, J. B. Li, X. L. Yue, J. T. S. Irvine, D. T. Xie, J. P. Ni and C. S. Ni, *ACS Catal.*, 2020, **10**, 14398-14409.
14. S. W. Tao and J. T. S. Irvine, *Nat. Mater.*, 2003, **2**, 320-323.

15. W. Wang, C. Su, Y. Z. Wu, R. Ran and Z. P. Shao, *Chem Rev*, 2013, **113**, 8104-8151.
16. P. I. Cowin, C. T. G. Petit, R. Lan, J. T. S. Irvine and S. W. Tao, *Adv. Energy Mater.*, 2011, **1**, 314-332.
17. S. Sengodan, S. Choi, A. Jun, T. H. Shin, Y. W. Ju, H. Y. Jeong, J. Shin, J. T. Irvine and G. Kim, *Nat. Mater.*, 2015, **14**, 205-209.
18. H. Yokokawa, *Annu. Rev. Mater. Res.*, 2003, **33**, 581-610.
19. T. Ishihara, N. Jirathiwathanakul and H. Zhong, *Energy Environ. Sci.*, 2010, **3**, 665-672.
20. S. P. Jiang, L. Liu, P. O. B. Khuong, W. B. Ping, H. Li and H. Pu, *J. Power Sources*, 2008, **176**, 82-89.
21. Q. Y. Hu, D. Y. Kim, W. G. Yang, L. X. Yang, Y. Meng, L. Zhang and H. K. Mao, *Nature*, 2016, **534**, 241-244.
22. T. Ishihara, *Perovskite oxide for solid oxide fuel cells*, Springer Science & Business Media, 2009.
23. M. A. Peña and J. L. G. Fierro, *Chem. Rev. (Washington, DC, U. S.)*, 2001, **101**, 1981-2018.
24. L. Shu, J. Sunarso, S. S. Hashim, J. Mao, W. Zhou and F. Liang, *Int. J. Hydrogen Energy*, 2019, **44**, 31275-31304.
25. S. Sengodan, S. Choi, A. Jun, T. H. Shin, Y.-W. Ju, H. Y. Jeong, J. Shin, J. T. S. Irvine and G. Kim, *Nat. Mater.*, 2015, **14**, 205-209.
26. T. Katsura, K. Kitayama, T. Sugihara and N. Kimizuka, *Bull. Chem. Soc. Jpn.*, 1975, **48**, 1809-1811.
27. H. Yokokawa, N. Sakai, T. Kawada and M. Dokiya, *Solid State Ionics*, 1992, **52**, 43-56.
28. H. Yokokawa, N. Sakai, T. Kawada and M. Dokiya, *J. Solid State Chem.*, 1991, **94**, 106-120.
29. C. Ni, Q. Zeng, D. He, L. Peng, D. Xie, J. T. S. Irvine, S. Duan and J. Ni, *J. Mater. Chem. A*, 2019, **7**, 26944-26953.
30. J. C. Grenier, N. Ea, M. Pouchard and P. Hagenmuller, *J. Solid State Chem.*, 1985, **58**, 243-252.
31. M. Kuhn, S. Hashimoto, K. Sato, K. Yashiro and J. Mizusaki, *Solid State Ionics*, 2011, **195**, 7-15.
32. R. Thalinger, M. Gocyla, M. Heggen, B. Klotzer and S. Penner, *J. Phys. Chem. C*, 2015, **119**, 22050-22056.
33. O. M. Sreedharan and M. S. Chandrasekharaiah, *J. Mater. Sci.*, 1986, **21**, 2581-2584.
34. K. T. Jacob, S. Gupta and P. Singh, *J. Am. Ceram. Soc.*, 2013, **96**, 3272-3278.
35. J. Mizusaki, T. Sasamoto, W. R. Cannon and H. K. Bowen, *J. Am. Ceram. Soc.*, 2010, **65**, 363-368.
36. T. Nakamura, G. Petzow and L. J. Gauckler, *Mater. Res. Bull.*, 1979, **14**, 649-659.
37. B. Hua, M. Li, Y. F. Sun, J. H. Li and J. L. Luo, *ChemSusChem*, 2017, **10**, 3333-3341.
38. Y. F. Li, W. Q. Zhang, Y. Zheng, J. Chen, B. Yu, Y. Chen and M. L. Liu, *Chem. Soc. Rev.*, 2017, **46**, 6345-6378.
39. Y. Nishihata, J. Mizuki, T. Akao, H. Tanaka, M. Uenishi, M. Kimura, T. Okamoto and N. Hamada, *Nature*, 2002, **418**, 164-167.
40. X. Sun, H. J. Chen, Y. M. Yin, M. T. Curnan, J. W. Han, Y. Chen and Z. F. Ma, *Small*, 2021, **17**, 2005383.
41. K. Kousi, C. Tang, I. S. Metcalfe and D. Neagu, *Small*, 2021, **17**, 2006479.
42. O. Kwon, S. Joo, S. Choi, S. Sengodan and G. Kim, *Journal of Physics-Energy*, 2020, **2**, 032001.
43. T. Cao, O. Kwon, R. J. Gorte and J. M. Vohs, *Nanomaterials*, 2020, **10**, 2445.
44. N. Hayashi, T. Yamamoto, H. Kageyama, M. Nishi, Y. Watanabe, T. Kawakami, Y. Matsushita, A. Fujimori and M. Takano, *Angew. Chem. Int. Edit.*, 2011, **50**, 12547-12550.

45. M. W. Schmidt, PhD, Australian National University, 2001.
46. A. Fossdal, M.-A. Einarsrud and T. Grande, *J. Solid State Chem.*, 2004, **177**, 2933-2942.
47. S. McIntosh and R. J. Gorte, *Chem Rev*, 2004, **104**, 4845-4865.
48. C. Su, W. Wang, M. L. Liu, M. O. Tade and Z. P. Shao, *Adv. Energy Mater.*, 2015, **5**, 1500188.
49. P. A. Connor, X. L. Yue, C. D. Savaniu, R. Price, G. Triantafyllou, M. Cassidy, G. Kerherve, D. J. Payne, R. C. Maher, L. F. Cohen, R. I. Tomov, B. A. Glowacki, R. V. Kumar and J. T. S. Irvine, *Adv. Energy Mater.*, 2018, **8**, 1800120.
50. J. M. Vohs and R. J. Gorte, *Adv. Mater. (Weinheim, Ger.)*, 2009, **21**, 943-956.
51. C. H. Zhao, Y. F. Li, W. Q. Zhang, Y. Zheng, X. M. Lou, B. Yu, J. Chen, Y. Chen, M. L. Liu and J. C. Wang, *Energy Environ. Sci.*, 2020, **13**, 53-85.
52. Y. F. Song, X. M. Zhang, K. Xie, G. X. Wang and X. H. Bao, *Adv. Mater.*, 2019, **31**, e1902033.
53. A. Hauch, R. Kungas, P. Blennow, A. B. Hansen, J. B. Hansen, B. V. Mathiesen and M. B. Mogensen, *Science*, 2020, **370**, eaba6118.
54. M. B. Mogensen, M. Chen, H. L. Frandsen, C. Graves, J. B. Hansen, K. V. Hansen, A. Hauch, T. Jacobsen, S. H. Jensen, T. L. Skafte and X. Sun, *Clean Energy*, 2019, **3**, 175-201.
55. D. Ding, X. X. Li, S. Y. Lai, K. Gerdes and M. L. Liu, *Energy Environ. Sci.*, 2014, **7**, 552-575.
56. S. Harboe, A. Schreiber, N. Margaritis, L. Blum, O. Guillon and N. H. Menzler, *Int. J. Hydrogen Energy*, 2020, **45**, 8015-8030.
57. P. Blennow, J. Hjelm, T. Klemenso, A. H. Persson, S. Ramousse and M. Mogensen, *Fuel Cells*, 2011, **11**, 661-668.
58. X. Chen, P. Y. Hou, C. P. Jacobson, S. J. Visco and L. C. De Jonghe, *Solid State Ionics*, 2005, **176**, 425-433.
59. C. S. Ni, D. F. Zhang, C. Y. Ni and Z. M. Wang, *Int. J. Hydrogen Energy*, 2014, **39**, 13314-13319.
60. L. Niewolak, E. Wessel, L. Singheiser and W. J. Quadakkers, *J. Power Sources*, 2010, **195**, 7600-7608.
61. M. C. Tucker, *J. Power Sources*, 2010, **195**, 4570-4582.
62. Y. C. Zhou, H. Wu, T. Luo, J. Q. Wang, Y. X. Shi, C. R. Xia, S. R. Wang and Z. L. Zhan, *Adv. Energy Mater.*, 2015, **5**, 1500375.
63. E. Stefan, D. Neagu, P. B. Tullmar, A. H. Persson, B. R. Sudireddy, D. Miller, M. Chen and J. Irvine, *Mater. Res. Bull.*, 2017, **89**, 232-244.
64. M. C. Tucker, G. Y. Lau, C. P. Jacobson, L. C. DeJonghe and S. J. Visco, *J. Power Sources*, 2007, **171**, 477-482.
65. T. Ishihara, J. Yan, M. Shinagawa and H. Matsumoto, *Electrochim. Acta*, 2006, **52**, 1645-1650.
66. R. Knibbe, H.-J. Wang, P. Blennow, K. Thydén, Å. H. Persson, L. Mikkelsen and T. Klemensø, *J. Power Sources*, 2013, **228**, 75-82.
67. B. Kang, J. Matsuda and T. Ishihara, *J. Mater. Chem. A*, 2019, **7**, 26105-26115.
68. H. C. Park and A. V. Virkar, *J. Power Sources*, 2009, **186**, 133-137.
69. X. G. Zhang, S. Ohara, H. Okawa, R. Maric and T. Fukui, *Solid State Ionics*, 2001, **139**, 145-152.
70. Y. W. Ju, H. Eto, T. Inagaki, S. Ida and T. Ishihara, *J. Power Sources*, 2010, **195**, 6294-6300.
71. S. B. Simonsen, T. T. Muhl, K. T. S. Thyden, C. Chatzichristodoulou, J. Nielsen and B. R. Sudireddy, *Solid State Ionics*, 2019, **340**, 115019.
72. L. L. Petschnig, G. Fuhrmann, D. Schildhammer, M. Tribus, H. Schottenberger and H. Huppertz, *Ceram. Int.*, 2016, **42**, 4262-4267.
73. M. Robbins, G. K. Wertheim, A. Menth and R. C. Sherwood, *J. Phys. Chem. Solids*, 1969, **30**, 1823-1825.

74. J. M. Haag, S. A. Barnett, J. W. Richardson and K. R. Poeppelmeier, *Chem. Mater.*, 2010, **22**, 3283-3289.
75. T. H. Shin, P. Vanalabhpatana and T. Ishihara, *J. Electrochem. Soc.*, 2010, **157**, B1896-B1901.
76. T. H. Shin, S. Ida and T. Ishihara, *J. Am. Chem. Soc.*, 2011, **133**, 19399-19407.
77. Y. S. Chung, T. Kim, T. H. Shin, H. Yoon, S. Park, N. M. Sammes, W. B. Kim and J. S. Chung, *J. Mater. Chem. A*, 2017, **5**, 6437-6446.
78. Y. Wu, Y. Yang, S. Zhou, W. Zhu, W. Song, H. Bao, H. Chen, X. Ou, M. Khan and Y. Ling, *Ceram. Int.*, 2020, **46**, 6714-6722.
79. W. W. Fan, Z. Sun, J. K. Wang, J. Zhou, K. Wu and Y. H. Cheng, *J. Power Sources*, 2016, **312**, 223-233.
80. A. Marcucci, F. Zurlo, I. N. Sora, E. Placidi, S. Casciardi, S. Licoccia and E. Di Bartolomeo, *J. Mater. Chem. A*, 2019, **7**, 5344-5352.
81. J. Shen, Y. Chen, G. M. Yang, W. Zhou, M. O. Tadé and Z. P. Shao, *J. Power Sources*, 2016, **306**, 92-99.
82. A. Marcucci, F. Zurlo, I. N. Sora, I. Luisetto, S. Licoccia and E. Di Bartolomeo, *Materialia*, 2019, **8**, 100460.
83. M. Qin, Y. Xiao, H. Yang, T. Tan, Z. Wang, X. Fan and C. Yang, *Appl. Catal. B*, 2021, **299**, 120613.
84. H. L. Tao, J. J. Xie, Y. F. Wu and S. R. Wang, *Int. J. Hydrogen Energy*, 2018, **43**, 15423-15432.
85. G. M. Yang, C. Su, Y. B. Chen, M. O. Tadé and Z. P. Shao, *J. Mater. Chem. A*, 2014, **2**, 19526-19535.
86. X. F. Ding, H. Liu, Z. P. Gao, G. X. Hua, L. X. Wang, L. M. Ding and G. L. Yuan, *Int. J. Hydrogen Energy*, 2017, **42**, 24968-24977.
87. L. Z. Bian, C. C. Duan, L. J. Wang, R. O'Hayre, J. Cheng and K. C. Chou, *J. Mater. Chem. A*, 2017, **5**, 15253-15259.
88. Z. H. Du, H. L. Zhao, S. Yi, Q. Xia, Y. Gong, Y. Zhang, X. Cheng, Y. Li, L. Gu and K. Swierczek, *ACS Nano*, 2016, **10**, 8660-8669.
89. Y. F. Sun, J. H. Li, L. Cui, B. Hua, S. H. Cui, J. Li and J. L. Luo, *Nanoscale*, 2015, **7**, 11173-11181.
90. J. Lu, Y. M. Yin, J. C. Li, L. Xu and Z. F. Ma, *Electrochem. Commun.*, 2015, **61**, 18-22.
91. C. L. Lu, B. B. Niu, W. D. Yi, Y. Ji and B. M. Xu, *Electrochim. Acta*, 2020, **358**, 136916.
92. C. H. Yang, J. Li, Y. Lin, J. Liu, F. L. Chen and M. L. Liu, *Nano Energy*, 2015, **11**, 704-710.
93. L. Zhang, C. H. Yang, A. I. Frenkel, S. W. Wang, G. L. Xiao, K. Brinkman and F. L. Chen, *J. Power Sources*, 2014, **262**, 421-428.
94. X. Y. Chen, W. J. Ni, J. Wang, Q. Zhong, M. F. Han and T. L. Zhu, *Electrochim. Acta*, 2018, **277**, 226-234.
95. X. W. Kong, X. L. Zhou, Y. Tian, X. Y. Wu, J. Zhang, W. Zuo, X. B. Gong and Z. H. Guo, *J. Power Sources*, 2016, **316**, 224-231.
96. H. P. Ding, D. S. Zhou, S. Liu, W. Wu, Y. T. Yang, Y. C. Yang and Z. T. Tao, *Appl. Energy*, 2019, **233**, 37-43.
97. B. B. Niu, F. J. Jin, T. Feng, L. L. Zhang, Y. Zhang and T. M. He, *Electrochim. Acta*, 2018, **270**, 174-182.
98. L. Z. Bian, C. C. Duan, L. J. Wang, L. Z. Zhu, R. O'Hayre and K. C. Chou, *J. Power Sources*, 2018, **399**, 398-405.
99. N. Xu, T. L. Zhu, Z. B. Yang and M. F. Han, *Electrochim. Acta*, 2018, **265**, 259-264.
100. P. Zhang, G. Q. Guan, D. S. Khaerudini, X. G. Hao, C. F. Xue, M. F. Han, Y. Kasai and A. Abudula, *J. Power Sources*, 2014, **266**, 241-249.

101. P. Zhang, G. Q. Guan, D. S. Khaerudini, X. G. Hao, M. F. Han, Y. Kasai, K. Sasagawa and A. Abudula, *J. Power Sources*, 2014, **248**, 163-171.
102. N. Xu, T. L. Zhu, Z. B. Yang and M. F. Han, *J. Mater. Sci. Tech.*, 2017, **33**, 1329-1333.
103. X. W. Kong, X. L. Zhou, Y. Tian, X. Y. Wu, J. Zhang and W. Zuo, *J. Power Sources*, 2016, **326**, 35-42.
104. R. J. Fu, P. p. Jiang, H. Xu, B. B. Niu, F. Jiang, L. Yang, T. Feng and T. M. He, *Int. J. Hydrogen Energy*, 2019, **44**, 31394-31405.
105. Z. B. Yang, Y. Chen, C. Jin, G. L. Xiao, M. F. Han and F. L. Chen, *RSC Adv.*, 2015, **5**, 2702-2705.
106. J. Xu, X. L. Zhou, X. L. Dong, L. Pan and K. N. Sun, *Ceram. Int.*, 2017, **43**, 10750-10756.
107. J. Xu, X. L. Zhou, L. Pan, M. X. Wu and K. N. Sun, *J. Power Sources*, 2017, **371**, 1-9.
108. S. Sengodan, J. S. Yoon, M. Y. Yoon, H. J. Hwang, J. Shin and G. Kim, *ECS Electrochem. Lett.*, 2013, **2**, F45-F49.
109. Z. Q. Cao, Y. H. Zhang, J. P. Miao, Z. H. Wang, Z. Lu, Y. Sui, X. Q. Huang and W. Jiang, *Int. J. Hydrogen Energy*, 2015, **40**, 16572-16577.
110. W. W. Fan, Z. Sun, Y. Bai, K. Wu and Y. H. Cheng, *ACS Appl. Mater. Interfaces*, 2019, **11**, 23168-23179.
111. W. W. Fan, Z. Sun, J. Zhou, K. Wu and Y. H. Cheng, *J. Power Sources*, 2017, **348**, 94-106.
112. L. dos Santos-Gómez, J. M. Porras-Vázquez, E. R. Losilla and D. Marrero-López, *RSC Adv.*, 2015, **5**, 107889-107895.
113. T. L. Zhu, H. E. Troiani, L. V. Mogni, M. F. Han and S. A. Barnett, *Joule*, 2018, **2**, 478-496.
114. S. Cho, D. E. Fowler, E. C. Miller, J. S. Cronin, K. R. Poeppelmeier and S. A. Barnett, *Energy Environ. Sci.*, 2013, **6**, 1850-1857.
115. Z. Q. Cao, L. D. Fan, G. H. Zhang, K. Shao, C. X. He, Q. L. Zhang, Z. Lv and B. Zhu, *Catal. Today*, 2019, **330**, 217-221.
116. M. B. Hanif, J.-T. Gao, K. Shaheen, Y.-P. Wang, M. Yasir, S.-L. Zhang, C.-J. Li and C.-X. Li, *J. Power Sources*, 2020, **472**, 228498.
117. R. Glaser, T. Zhu, H. Troiani, A. Caneiro, L. Mogni and S. Barnett, *J. Mater. Chem. A*, 2018, **6**, 5193-5201.
118. J. M. Haag, D. M. Bierschenk, S. A. Barnett and K. R. Poeppelmeier, *Solid State Ionics*, 2012, **212**, 1-5.
119. Q. Zhou, C. Yuan, D. Han, T. Luo, J. L. Li and Z. L. Zhan, *Electrochim. Acta*, 2014, **133**, 453-458.
120. S. W. Tao and J. T. S. Irvine, *Chem. Mater.*, 2004, **16**, 4116-4121.
121. J. Peña-Martínez, D. Marrero-López, D. Pérez-Coll, J. C. Ruiz-Morales and P. Núñez, *Electrochim. Acta*, 2007, **52**, 2950-2958.
122. Y. F. Sun, J. H. Li, K. T. Chuang and J. L. Luo, *J. Power Sources*, 2015, **274**, 483-487.
123. Y. H. Wan, Y. L. Xing, Z. Q. Xu, S. S. Xue, S. W. Zhang and C. R. Xia, *Appl. Catal. B-Environ.*, 2020, **269**, 118809.
124. X. J. Liu, D. Han, Y. C. Zhou, X. Meng, H. Wu, J. L. Li, F. R. Zeng and Z. L. Zhan, *J. Power Sources*, 2014, **246**, 457-463.
125. Q. Zhang, T. Wei and Y. H. Huang, *J. Power Sources*, 2012, **198**, 59-65.
126. S. E. Hou, A. Aguadero, J. A. Alonso and J. B. Goodenough, *J. Power Sources*, 2011, **196**, 5478-5484.
127. H. P. Ding, Z. T. Tao, S. Liu and Y. T. Yang, *J. Power Sources*, 2016, **327**, 573-579.
128. Y. C. Zhou, X. Meng, X. J. Liu, X. Pan, J. L. Li, X. F. Ye, H. W. Nie, C. R. Xia, S. R. Wang and Z. L. Zhan, *J. Power Sources*, 2014, **267**, 148-154.
129. Q. Liu, X. Dong, G. L. Xiao, F. Zhao and F. L. Chen, *Adv. Mater.*, 2010, **22**, 5478-5482.

130. Z. Q. Xu, X. Y. Hu, Y. H. Wan, S. S. Xue, S. W. Zhang, L. J. Zhang, B. Z. Zhang and C. R. Xia, *Electrochim. Acta*, 2020, **341**, 136067.
131. B. B. Niu, F. J. Jin, L. L. Zhang, P. F. Shen and T. M. He, *Electrochim. Acta*, 2018, **263**, 217-227.
132. X. Meng, X. J. Liu, D. Han, H. Wu, J. L. Li and Z. L. Zhan, *J. Power Sources*, 2014, **252**, 58-63.
133. X. Yang, J. Chen, D. Panthi, B. B. Niu, L. B. Lei, Z. H. Yuan, Y. H. Du, Y. F. Li, F. L. Chen and T. M. He, *J. Mater. Chem. A*, 2019, **7**, 733-743.
134. M. Gou, R. Ren, W. Sun, C. Xu, X. Meng, Z. Wang, J. Qiao and K. Sun, *Ceram. Int.*, 2019, **45**, 15696-15704.
135. S. S. Xue, N. Shi, Y. H. Wan, Z. D. Xu, D. M. Huan, S. W. Zhang, C. R. Xia, R. R. Peng and Y. L. Lu, *J. Mater. Chem. A*, 2019, **7**, 21783-21793.
136. F. Liu, L. L. Zhang, G. Z. Huang, B. B. Niu, X. R. Li, L. Wang, J. Zhao and Y. Jin, *Electrochim. Acta*, 2017, **255**, 118-126.
137. P. Zhang, G. Q. Guan, D. S. Khaerudini, X. Q. Hao, C. F. Xue, M. F. Han, Y. Kasai and A. Abudula, *J. Power Sources*, 2015, **276**, 347-356.
138. C. L. Lu, B. B. Niu, S. L. Yu, W. D. Yi, S. J. Luo, B. M. Xu and Y. Ji, *Electrochim. Acta*, 2019, **323**, 134857.
139. W. He, J. C. Fan, H. Zhang, M. N. Chen, Z. M. Sun and M. Ni, *Int. J. Hydrogen Energy*, 2019, **44**, 32164-32169.
140. L. dos Santos-Gómez, J. M. Compana, S. Bruque, E. R. Losilla and D. Marrero-López, *J. Power Sources*, 2015, **279**, 419-427.
141. Y. X. Cao, Z. W. Zhu, Y. J. Zhao, W. Zhao, Z. L. Wei and T. Liu, *J. Power Sources*, 2020, **455**, 227951.
142. T. L. Su, Y. H. Li, Y. Yang, Z. Q. Xu, N. Shi, Y. H. Wan, Y. Xie, D. M. Huan, S. S. Xue and C. R. Xia, *Int. J. Hydrogen Energy*, 2020, **45**, 23401-23410.
143. E. Stefan, G. Tsekouras and J. T. S. Irvine, *Adv. Energy Mater.*, 2013, **3**, 1454-1462.
144. C. Ni, J. Feng, J. Cui, J. Zhou and J. Ni, *J. Electrochem. Soc.*, 2017, **164**, F283-F288.
145. I. Nagai, N. Shirakawa, S.-i. Ikeda, R. Iwasaki, H. Nishimura and M. Kosaka, *Appl. Phys. Lett.*, 2005, **87**, 024105.
146. R. B. Macquart, B. J. Kennedy and M. Avdeev, *J. Solid State Chem.*, 2010, **183**, 250-255.
147. G. Y. Liu, G. H. Rao, X. M. Feng, H. F. Yang, Z. W. Ouyang, W. F. Liu and J. K. Liang, *J. Alloys Compd.*, 2003, **353**, 42-47.
148. G. Xiao, Q. Liu, S. Wang, V. G. Komvokis, M. D. Amiridis, A. Heyden, S. Ma and F. Chen, *J. Power Sources*, 2012, **202**, 63-69.
149. Q. Liu, D. E. Bugaris, G. L. Xiao, M. Chmara, S. Ma, H. C. zur Loye, M. D. Amiridis and F. L. Chen, *J. Power Sources*, 2011, **196**, 9148-9153.
150. J. Feng, G. Q. Yang, N. N. Dai, Z. H. Wang, W. Sun, D. Rooney, J. S. Qiao and K. N. Sun, *J. Mater. Chem. A*, 2014, **2**, 17628-17634.
151. J. Feng, J. S. Qiao, W. Y. Wang, Z. H. Wang, W. Sun and K. N. Sun, *Electrochim. Acta*, 2016, **215**, 592-599.
152. B. B. He, L. Zhao, S. X. Song, T. Liu, F. L. Chen and C. R. Xia, *J. Electrochem. Soc.*, 2012, **159**, B619-B626.
153. J. Liu, Y. Lei, Y. Li, J. Gao, D. Han, W. T. Zhan, F. Q. Huang and S. R. Wang, *Electrochem. Commun.*, 2017, **78**, 6-10.
154. L. L. Zhang, Q. J. Zhou, Q. He and T. M. He, *J. Power Sources*, 2010, **195**, 6356-6366.
155. H. Yokokawa, T. Horita, N. Sakai, K. Yamaji, M. E. Brito, Y. P. Xiong and H. Kishimoto, *Solid State Ionics*, 2006, **177**, 3193-3198.
156. B. L. Chamberland, *Solid State Commun.*, 1967, **5**, 663-666.

157. D. E. Fowler, J. M. Haag, C. Boland, D. M. Bierschenk, S. A. Barnett and K. R. Poeppelmeier, *Chem. Mater.*, 2014, **26**, 3113-3120.
158. T. R. Clevenger, *J. Am. Ceram. Soc.*, 1963, **46**, 207-210.
159. N. H. Perry, J. J. Kim, S. R. Bishop and H. L. Tuller, *J. Mater. Chem. A*, 2015, **3**, 3602-3611.
160. A. Nenning, L. Volgger, E. Miller, L. V. Mogni, S. Barnett and J. Fleig, *J. Electrochem. Soc.*, 2017, **164**, F364-F371.
161. X. J. Liu, D. T. Xie, J. T. S. Irvine, J. P. Ni and C. S. Ni, *Electrochim. Acta*, 2020, **335**, 135692.
162. L. Guczi, *Catal. Rev.*, 1981, **23**, 329-376.
163. L. Adijanto, A. Sampath, A. S. Yu, M. Cargnello, P. Fornasiero, R. J. Gorte and J. M. Vohs, *ACS Catal.*, 2013, **3**, 1801-1809.
164. M. Cargnello, J. J. Delgado Jaen, J. C. Hernandez Garrido, K. Bakhmutsky, T. Montini, J. J. Calvino Gamez, R. J. Gorte and P. Fornasiero, *Science*, 2012, **337**, 713-717.
165. N. Yan, J. Pandey, Y. Zeng, B. S. Amirkhiz, B. Hua, N. J. Geels, J.-L. Luo and G. Rothenberg, *ACS Catal.*, 2016, **6**, 4630-4634.
166. J. S. Kim, N. L. Wieder, A. J. Abraham, M. Cargnello, P. Fornasiero, R. J. Gorte and J. M. Vohs, *J. Electrochem. Soc.*, 2011, **158**, B596-B600.
167. N. L. Wieder, M. Cargnello, K. Bakhmutsky, T. Montini, P. Fornasiero and R. J. Gorte, *J. Phys. Chem. C*, 2010, **115**, 915-919.
168. R. Brown, M. E. Cooper and D. A. Whan, *Appl. Catal.*, 1982, **3**, 177-186.
169. R. Garten, *J. Catal.*, 1974, **35**, 232-246.
170. L. Y. Lu, C. S. Ni, M. Cassidy and J. T. S. Irvine, *J. Mater. Chem. A*, 2016, **4**, 11708-11718.
171. C. S. Ni, L. Y. Lu, D. N. Miller, M. Cassidy and J. T. S. Irvine, *J. Mater. Chem. A*, 2018, **6**, 5398-5406.
172. S. Joo, O. Kwon, K. Kim, S. Kim, H. Kim, J. Shin, H. Y. Jeong, S. Sengodan, J. W. Han and G. Kim, *Nat. Commun.*, 2019, **10**, 697.
173. D. Neagu, G. Tsekouras, D. N. Miller, H. Menard and J. T. S. Irvine, *Nature Chem.*, 2013, **5**, 916-923.
174. E. I. Papaioannou, D. Neagu, W. K. W. Ramli, J. T. S. Irvine and I. S. Metcalfe, *Top. Catal.*, 2018, **62**, 1149-1156.
175. W. Y. Wang, C. L. Zhu, K. Xie and L. Z. Gan, *J. Power Sources*, 2018, **406**, 1-6.
176. W. W. Zhang, H. C. Wang, K. Guan, J. L. Meng, Z. Y. Wei, X. J. Liu and J. Meng, *ACS Appl. Mater. Interfaces*, 2020, **12**, 461-473.
177. N. J. Hou, T. T. Yao, P. Li, X. L. Yao, T. Gan, L. J. Fan, J. Wang, X. J. Zhi, Y. C. Zhao and Y. D. Li, *ACS Appl. Mater. Interfaces*, 2019, **11**, 6995-7005.
178. S. H. Jensen, P. H. Larsen and M. Mogensen, *Int. J. Hydrogen Energy*, 2007, **32**, 3253-3257.
179. B. G. Pound, D. J. M. Bevan and J. O. Bockris, *Int. J. Hydrogen Energy*, 1981, **6**, 473-486.
180. M. S. Sohal, J. E. O'Brien, C. M. Stoots, V. I. Sharma, B. Yildiz and A. Virkar, *J. Fuel Cell Sci. Technol.*, 2012, **9**, 011017.
181. A. Hauch, S. D. Ebbesen, S. H. Jensen and M. Mogensen, *J. Electrochem. Soc.*, 2008, **155**, B1184-B1193.
182. H. P. Dasari, S.-Y. Park, J. Kim, J.-H. Lee, B.-K. Kim, H.-J. Je, H.-W. Lee and K. J. Yoon, *J. Power Sources*, 2013, **240**, 721-728.
183. G. Tsekouras, D. Neagu and J. T. S. Irvine, *Energy Environ. Sci.*, 2013, **6**, 256-266.
184. J. H. Myung, D. Neagu, D. N. Miller and J. T. Irvine, *Nature*, 2016, **537**, 528-531.
185. X. D. Yang and J. T. S. Irvine, *J. Mater. Chem.*, 2008, **18**, 2349-2354.
186. K. Hosoi, H. Hagiwara, S. Ida and T. Ishihara, *J. Phys. Chem. C*, 2016, **120**, 16110-16117.

187. A. K. Opitz, A. Nenning, C. Rameshan, R. Rameshan, R. Blume, M. Havecker, A. Knop-Gericke, G. Rupprechter, J. Fleig and B. Klotzer, *Angew. Chem. Int. Ed. Engl.*, 2015, **54**, 2628-2632.
188. T. Liu, Y. Q. Zhao, X. Y. Zhang, H. Zhang, G. Jiang, W. Zhao, J. Y. Guo, F. L. Chen, M. F. Yan, Y. X. Zhang and Y. Wang, *J. Mater. Chem. A*, 2020, **8**, 582-591.
189. B. Ge, J. T. Ma, D. S. Ai, C. S. Deng, X. P. Lin and J. M. Xu, *Electrochim. Acta*, 2015, **151**, 437-446.
190. Z. Li, S. S. Li, C. J. Tseng, S. W. Tao and K. Xie, *Electrochim. Acta*, 2017, **229**, 48-54.
191. D. Papargyriou, D. N. Miller and J. T. Sirr Irvine, *J. Mater. Chem. A*, 2019, **7**, 15812-15822.
192. Y. X. Li, G. J. Wu, C. Ruan, Q. Zhou, Y. Wang, W. Doherty, K. Xie and Y. C. Wu, *J. Power Sources*, 2014, **253**, 349-359.
193. Q. Q. Qin, G. J. Wu, S. G. Chen, W. Doherty, K. Xie and Y. C. Wu, *Electrochim. Acta*, 2014, **127**, 215-227.
194. X. J. Liu, J. Zhou, D. T. Xie, J. P. Ni and C. S. Ni, *Solid State Ionics*, 2020, **345**, 115181.
195. D. Dogu, S. Gunduz, K. E. Meyer, D. J. Deka, A. C. Co and U. S. Ozkan, *Catal. Lett.*, 2019, **149**, 1743-1752.
196. X. M. Zhang, Y. F. Song, G. X. Wang and X. H. Bao, *J. Energy Chem.*, 2017, **26**, 839-853.
197. D. Schafer, Q. P. Fang, L. Blum and D. Stolten, *J. Power Sources*, 2019, **433**, 126666.
198. S. Hu, L. Zhang, H. Liu, Z. Cao, W. Yu, X. Zhu and W. Yang, *J. Power Sources*, 2019, **443**, 227268.
199. Y. Yang, Y. H. Li, Y. A. Jiang, M. H. Zheng, T. Hong, X. J. Wu and C. R. Xia, *Electrochim. Acta*, 2018, **284**, 159-167.
200. A. K. Opitz, A. Nenning, C. Rameshan, M. Kubicek, T. Gotsch, R. Blume, M. Havecker, A. Knop-Gericke, G. Rupprechter, B. Klotzer and J. Fleig, *ACS Appl. Mater. Interfaces*, 2017, **9**, 35847-35860.
201. S. Hu, L. Zhang, Z. Cao, W. Yu, P. Zhang, X. Zhu and W. Yang, *J. Power Sources*, 2021, **485**, 229343.
202. W. T. Yao, T. Duan, Y. X. Li, L. M. Yang and K. Xie, *New J. Chem.*, 2015, **39**, 2956-2965.
203. C. L. Zhu, S. S. Hou, L. X. Hou and K. Xie, *Int. J. Hydrogen Energy*, 2018, **43**, 17040-17047.
204. Z. Q. Cao, B. Wei, J. P. Miao, Z. H. Wang, Z. Lu, W. Y. Li, Y. H. Zhang, X. Q. Huang, X. B. Zhu, Q. Feng and Y. Sui, *Electrochem. Commun.*, 2016, **69**, 80-83.
205. P. K. Addo, B. Molero‐Sanchez, M. Chen, S. Paulson and V. Birss, *Fuel Cells*, 2015, **15**, 689-696.
206. B. Molero-Sanchez, P. Addo, A. Buyukaksoy, S. Paulson and V. Birss, *Faraday Discuss.*, 2015, **182**, 159-175.
207. Y. Q. Zhang, J. H. Li, Y. F. Sun, B. Hua and J. L. Luo, *ACS Appl. Mater. Interfaces*, 2016, **8**, 6457-6463.
208. Y. J. Zhou, Z. W. Zhou, Y. F. Song, X. M. Zhang, F. Guan, H. F. Lv, Q. X. Liu, S. Miao, G. X. Wang and X. H. Bao, *Nano Energy*, 2018, **50**, 43-51.
209. S. Wang, B. Qian, Z. Wang, B. Yin, Y. Zheng, L. Ge, H. Chen and H. Yang, *J. Alloys Compd.*, 2021, **888**, 161573.
210. S. Wang and T. Ishihara, *ECS Trans.*, 2013, **57**, 3171-3176.
211. Y. H. Li, B. B. Hu, C. R. Xia, W. Q. Xu, J. P. Lemmon and F. L. Chen, *J. Mater. Chem. A*, 2017, **5**, 20833-20842.
212. Y. H. Li, Z. L. Zhan and C. R. Xia, *Catal. Sci. Technol.*, 2018, **8**, 980-984.
213. Y. H. Li, X. R. Chen, Y. Yang, Y. Jiang and C. R. Xia, *ACS Sustain. Chem. Eng.*, 2017, **5**, 11403-11412.

214. H. Lv, L. Lin, X. Zhang, D. Gao, Y. Song, Y. Zhou, Q. Liu, G. Wang and X. Bao, *J. Mater. Chem. A*, 2019, **7**, 11967-11975.
215. Y. H. Li, Y. Li, Y. H. Wan, Y. Xie, J. F. Zhu, H. B. Pan, X. S. Zheng and C. R. Xia, *Adv. Energy Mater.*, 2019, **9**, 1803156.
216. S. B. Liu, Q. X. Liu and J.-L. Luo, *ACS Catal.*, 2016, **6**, 6219-6228.
217. H. Lv, T. Liu, X. Zhang, Y. Song, H. Matsumoto, N. Ta, C. Zeng, G. Wang and X. Bao, *Angew. Chem. Int. Ed.*, 2020, **59**, 15968-15973.
218. H. Lv, L. Lin, X. Zhang, Y. Song, H. Matsumoto, C. Zeng, N. Ta, W. Liu, D. Gao, G. Wang and X. Bao, *Adv. Mater. (Weinheim, Ger.)*, 2020, **32**, 1906193.
219. S. Hu, L. Zhang, L. Cai, Z. Cao, Q. Jiang, W. Yu, Y. Wu, X. Zhu and W. Yang, *J. Mater. Chem. A*, 2020, **8**, 21053-21061.
220. L. Z. Bian, C. C. Duan, L. J. Wang, Z. Y. Chen, Y. T. Hou, J. Peng, X. W. Song, S. L. An and R. O'Hayre, *J. Power Sources*, 2021, **482**, 228887.
221. Z. Zhan, W. Kobsiriphat, J. R. Wilson, M. Pillai, I. Kim and S. A. Barnett, *Energy Fuels*, 2009, **23**, 3089-3096.
222. K. Xie, Y. Q. Zhang, G. Y. Meng and J. T. S. Irvine, *Energy Environ. Sci.*, 2011, **4**, 2218-2222.
223. L. Chen, F. L. Chen and C. R. Xia, *Energy Environ. Sci.*, 2014, **7**, 4018-4022.
224. L. G. Wang, M. Rao, S. Diethelm, T. E. Lin, H. F. Zhang, A. Hagen, F. Marechal and J. Van Herle, *Appl. Energy*, 2019, **250**, 1432-1445.
225. Y. Zheng, J. C. Wang, B. Yu, W. Q. Zhang, J. Chen, J. L. Qiao and J. J. Zhang, *Chem. Soc. Rev.*, 2017, **46**, 1427-1463.
226. V. Kyriakou, D. Neagu, E. I. Papaioannou, I. S. Metcalfe, M. C. M. van de Sanden and M. N. Tsampas, *Appl. Catal. B*, 2019, **258**, 117950.
227. M. Ni, *J. Power Sources*, 2012, **202**, 209-216.
228. S. D. Ebbesen, C. Graves and M. Mogensen, *International Journal of Green Energy*, 2009, **6**, 646-660.
229. Y. Wang, T. Liu, S. M. Fang and F. L. Chen, *J. Power Sources*, 2016, **305**, 240-248.
230. C. Graves, S. D. Ebbesen and M. Mogensen, *Solid State Ionics*, 2011, **192**, 398-403.
231. Z. B. Yang, N. Wang, C. Y. Ma, X. F. Jin, Z. Lei, X. Y. Xiong and S. P. Peng, *J. Electroanal. Chem.*, 2019, **836**, 107-111.
232. Y. H. Li, P. Li, B. B. Hu and C. R. Xia, *J. Mater. Chem. A*, 2016, **4**, 9236-9243.
233. D. J. Deka, S. Gunduz, T. Fitzgerald, J. T. Miller, A. C. Co and U. S. Ozkan, *Appl. Catal. B*, 2019, **248**, 487-503.
234. D. J. Deka, J. Kim, S. Gunduz, M. Ferree, A. C. Co and U. S. Ozkan, *Appl. Catal. A-Gen.*, 2020, **602**, 117697.
235. V. Sereda, A. Sednev, D. Tsvetkov and A. Zuev, *J. Mater. Res.*, 2019, **34**, 3288-3295.
236. S. Stolen, C. E. Mohn, P. Ravindran and N. L. Allan, *J. Phys. Chem. B*, 2005, **109**, 12362-12365.
237. Q. M. Zeng, X. J. Liu, D. T. Xie, J. P. Ni and C. S. Ni, *Int. J. Hydrogen Energy*, 2019, **44**, 15387-15399.
238. K. Huang, H. Y. Lee and J. B. Goodenough, *J. Electrochem. Soc.*, 2019, **145**, 3220-3227.
239. V. V. Kharton, A. P. Viskup, E. N. Naumovich and V. N. Tikhonovich, *Mater. Res. Bull.*, 1999, **34**, 1311-1317.
240. F. Bidrawn, S. Lee, J. M. Vohs and R. J. Gorte, *J. Electrochem. Soc.*, 2008, **155**, B660-B665.
241. S. P. Simner, J. F. Bonnett, N. L. Canfield, K. D. Meinhardt, V. L. Sprenkle and J. W. Stevenson, *Electrochem. Solid-State Lett.*, 2002, **5**, A173-A175.
242. Y. Cheng, T. S. Oh, R. Wilson, R. J. Gorte and J. M. Vohs, *J. Electrochem. Soc.*, 2017, **164**, F525-F529.

243. P. Li, I. W. Chen and J. E. Penner‐Hahn, *J. Am. Ceram. Soc.*, 1994, **77**, 118-128.
244. Y. Yamaguchi, I. Kagomiya, S. Minami, H. Shimada, H. Sumi, Y. Ogura and Y. Mizutani, *J. Power Sources*, 2020, **448**, 227426.
245. S. R. Bishop, D. Marrocchelli, C. Chatzichristodoulou, N. H. Perry, M. B. Mogensen, H. L. Tuller and E. D. Wachsman, *Annu. Rev. Mater. Res.*, 2014, **44**, 205-239.
246. F. F. Dong, D. J. Chen, Y. B. Chen, Q. Zhao and Z. P. Shao, *J. Mater. Chem.*, 2012, **22**, 15071-15079.
247. S. P. Jiang, *Int. J. Hydrogen Energy*, 2019, **44**, 7448-7493.
248. Y. Teraoka, H. M. Zhang, K. Okamoto and N. Yamazoe, *Mater. Res. Bull.*, 1988, **23**, 51-58.
249. S. P. Simner, J. R. Bonnett, N. L. Canfield, K. D. Meinhardt, J. P. Shelton, V. L. Sprenkle and J. W. Stevenson, *J. Power Sources*, 2003, **113**, 1-10.
250. H. Ullmann, N. Trofimenko, F. Tietz, D. Stover and A. Ahmad-Khanlou, *Solid State Ionics*, 2000, **138**, 79-90.
251. G. C. Kostogloudis and C. Ftikos, *Solid State Ionics*, 1999, **126**, 143-151.
252. J. Chen, F. L. Liang, B. Chi, J. Pu, S. P. Jiang and L. Jian, *J. Power Sources*, 2009, **194**, 275-280.
253. F. F. Dong, Y. B. Chen, D. J. Chen and Z. P. Shao, *ACS Appl. Mater. Interfaces*, 2014, **6**, 11180-11189.
254. M. Li, M. H. Zheng, B. B. Hu, Y. X. Zhang and C. R. Xia, *Electrochim. Acta*, 2017, **230**, 196-203.
255. J. W. Ju, Y. Xie, Z. Y. Wang, Y. X. Zhang and C. R. Xia, *J. Electrochem. Soc.*, 2016, **163**, F393-F400.
256. D. Waller, J. A. Lane, J. A. Kilner and B. C. H. Steele, *Solid State Ionics*, 1996, **86-8**, 767-772.
257. Y. J. Leng, S. H. Chan and Q. L. Liu, *Int. J. Hydrogen Energy*, 2008, **33**, 3808-3817.
258. L. F. Nie, M. F. Liu, Y. J. Zhang and M. L. Liu, *J. Power Sources*, 2010, **195**, 4704-4708.
259. S. S. Jiang, J. Sunarso, W. Zhou, J. Shen, R. Ran and Z. P. Shao, *J. Power Sources*, 2015, **298**, 209-216.
260. N. Tsvetkov, Q. Lu, L. Sun, E. J. Crumlin and B. Yildiz, *Nat. Mater.*, 2016, **15**, 1010-1017.
261. M. Nadeem, Y. H. Wan and C. R. Xia, *Compos. Part B-Eng.*, 2020, **189**, 107924.
262. M. Nadeem, B. B. Hu and C. R. Xia, *Int. J. Hydrogen Energy*, 2018, **43**, 8079-8087.
263. Y. Yang, M. Li, Y. Y. Ren, Y. H. Li and C. R. Xia, *Int. J. Hydrogen Energy*, 2018, **43**, 3797-3802.
264. C. Nicollet, C. Toparli, G. F. Harrington, T. Defferriere, B. Yildiz and H. L. Tuller, *Nat. Catal.*, 2020, **3**, 913-920.
265. M. E. Lynch, L. Yang, W. Qin, J.-J. Choi, M. Liu, K. Blinn and M. Liu, *Energy Environ. Sci.*, 2011, **4**, 2249-2258.
266. D. Ding, M. F. Liu, Z. B. Liu, X. X. Li, K. Blinn, X. B. Zhu and M. L. Liu, *Adv. Energy Mater.*, 2013, **3**, 1149-1154.
267. L. Zhao, J. Drennan, C. Kong, S. Amarasinghe and S. P. Jiang, *J. Mater. Chem. A*, 2014, **2**, 11114-11123.
268. W. W. Zhang, H. C. Wang, K. Guan, Z. Y. Wei, X. Zhang, J. L. Meng, X. J. Liu and J. Meng, *ACS Appl. Mater. Interfaces*, 2019, **11**, 26830-26841.
269. E. Konysheva, R. Blackley and J. T. S. Irvine, *Chem. Mater.*, 2010, **22**, 4700-4711.
270. M. Li, Y. Y. Ren, Z. S. Zhu, S. Y. Zhu, F. L. Chen, Y. X. Zhang and C. R. Xia, *Electrochim. Acta*, 2016, **191**, 651-660.
271. A. L. Shaula, Y. V. Pivak, J. C. Waerenborgh, P. Gaczynski, A. A. Yaremchenko and V. V. Kharton, *Solid State Ionics*, 2006, **177**, 2923-2930.
272. Q. A. Li, L. P. Sun, L. H. Huo, H. Zhao and J. C. Grenier, *Int. J. Hydrogen Energy*, 2010, **35**, 9151-9157.

273. G. M. Yang, W. Zhou, M. L. Liu and Z. P. Shao, *ACS Appl. Mater. Interfaces*, 2016, **8**, 35308-35314.
274. S.-L. Zhang, H. Wang, M. Y. Lu, A.-P. Zhang, L. V. Mogni, Q. Liu, C.-X. Li, C.-J. Li and S. A. Barnett, *Energy Environ. Sci.*, 2018, **11**, 1870-1879.
275. A. B. Munoz-Garcia, D. E. Bugaris, M. Pavone, J. P. Hodges, A. Huq, F. Chen, H. C. zur Loye and E. A. Carter, *J. Am. Chem. Soc.*, 2012, **134**, 6826-6833.
276. L. H. Zhang, W. Sun, C. M. Xu, R. Z. Ren, X. X. Yang, J. S. Qiao, Z. H. Wang and K. N. Sun, *J. Mater. Chem. A*, 2020, **8**, 14091-14098.
277. Y. L. Zhang, Z. C. Zhu, Y. H. Gu, H. Chen, Y. F. Zheng and L. Ge, *Ceram. Int.*, 2020, **46**, 22787-22796.
278. Z. B. Zhang, Y. L. Zhu, Y. J. Zhong, W. Zhou and Z. P. Shao, *Adv. Energy Mater.*, 2017, **7**, 1700242.
279. J. W. Zhu, G. P. Liu, Z. K. Liu, Z. Y. Chu, W. Q. Jin and N. P. Xu, *Adv. Mater.*, 2016, **28**, 3511-3515.
280. D. M. Bastidas, S. W. Tao and J. T. S. Irvine, *J. Mater. Chem.*, 2006, **16**, 1603-1605.
281. A. A. Markov, O. A. Savinskaya, M. V. Patrakeev, A. P. Nemudry, I. A. Leonidov, Y. T. Pavlyukhin, A. V. Ishchenko and V. L. Kozhevnikov, *J. Solid State Chem.*, 2009, **182**, 799-806.
282. A. J. Fernandez-Ropero, J. M. Porras-Vazquez, A. Cabeza, P. R. Slater, D. Marrero-Lopez and E. R. Losilla, *J. Power Sources*, 2014, **249**, 405-413.
283. M. V. Patrakeev, I. A. Leonidov, V. L. Kozhevnikov and V. V. Kharton, *Solid State Sci.*, 2004, **6**, 907-913.
284. W. W. Fan, Z. Sun, J. K. Wang, J. Zhou, K. Wu and Y. H. Cheng, *RSC Adv.*, 2016, **6**, 34564-34573.
285. X. Y. Lu, Y. Yang, Y. Z. Ding, Y. H. Chen, Q. W. Gu, D. Tian, W. L. Yu and B. Lin, *Electrochim. Acta*, 2017, **227**, 33-40.
286. J. Canales-Vazquez, J. C. Ruiz-Morales, D. Marrero-Lopez, J. Pena-Martinez, P. Nunez and P. Gomez-Romero, *J. Power Sources*, 2007, **171**, 552-557.
287. J. M. Haag, B. D. Madsen, S. A. Barnett and K. R. Poeppelmeier, *Electrochem. Solid-State Lett.*, 2008, **11**, B51-B53.
288. M. Chen, S. Paulson, V. Thangadurai and V. Birss, *J. Power Sources*, 2013, **236**, 68-79.
289. B. K. Lai, K. Kerman and S. Ramanathan, *J. Power Sources*, 2011, **196**, 1826-1832.
290. L. Zhao, K. F. Chen, Y. X. Liu and B. B. He, *J. Power Sources*, 2017, **342**, 313-319.
291. W. He, X. L. Wu, F. F. Dong and M. Ni, *J. Power Sources*, 2017, **363**, 16-19.
292. Y. C. Zhou, X. J. Liu, J. L. Li, H. W. Nie, X. F. Ye, S. R. Wang and Z. L. Zhan, *J. Power Sources*, 2014, **252**, 164-168.
293. S. Gupta, M. K. Verma and D. Singh, *Ceram. Int.*, 2016, **42**, 18418-18424.
294. J. Zhou, G. Chen, K. Wu and Y. H. Cheng, *J. Power Sources*, 2013, **232**, 332-337.
295. G. M. Yang, C. Su, R. Ran, M. O. Tade and Z. P. Shao, *Energy Fuels*, 2014, **28**, 356-362.
296. J. Zhou, G. Chen, K. Wu and Y. H. Cheng, *J. Phys. Chem. C*, 2013, **117**, 12991-12999.
297. M. Al Daroukh, *Solid State Ionics*, 2003, **158**, 141-150.
298. J. Zhou, Y. Chen, G. Chen, K. Wu and Y. H. Cheng, *J. Alloys Compd.*, 2015, **647**, 778-783.
299. H. El Shinawi and C. Greaves, *J. Solid State Chem.*, 2008, **181**, 2705-2712.
300. J. Zhou, T. H. Shin, C. S. Ni, G. Chen, K. Wu, Y. H. Cheng and J. T. S. Irvine, *Chem. Mater.*, 2016, **28**, 2981-2993.
301. X. Z. Peng, Y. F. Tian, Y. Liu, W. J. Wang, L. C. Jia, J. Pu, B. Chi and J. Li, *J. CO2 Util.*, 2020, **36**, 18-24.

302. Y. F. Tian, H. Y. Zheng, L. L. Zhang, B. Chi, J. Pu and J. Li, *J. Electrochem. Soc.*, 2018, **165**, F17-F23.
303. Y. F. Tian, L. L. Zhang, L. C. Jia, X. Wang, J. Yang, B. Chi, J. Pu and J. Li, *J. CO2 Util.*, 2019, **31**, 43-50.
304. L. Z. Bian, C. C. Duan, L. J. Wang, Y. T. Hou, L. Z. Zhu, R. O'Hayre and K. C. Chou, *J. Electrochem. Soc.*, 2018, **165**, F981-F985.
305. J. Zhou, L. Y. Xu, C. W. Ding, C. Y. Wei and Z. T. Tao, *Mater. Lett.*, 2019, **257**, 126758.
306. Q. Liu, C. H. Yang, X. H. Dong and F. L. Chen, *Int. J. Hydrogen Energy*, 2010, **35**, 10039-10044.
307. US6051125A, 2000.
308. J. Martinez-Frias, A. Q. Pham and S. M. Aceves, *Int. J. Hydrogen Energy*, 2003, **28**, 483-490.
309. W. S. Wang, J. M. Vohs and R. J. Gorte, *Top. Catal.*, 2007, **46**, 380-385.
310. Y. Wang, J. H. Xu, X. Y. Meng, T. Liu and F. L. Chen, *Electrochem. Commun.*, 2017, **79**, 63-67.
311. C. L. Zhu, S. S. Hou, X. L. Hu, J. H. Lu, F. L. Chen and K. Xie, *Nat. Commun.*, 2019, **10**, 1173.
312. A. V. Virkar, *Int. J. Hydrogen Energy*, 2010, **35**, 9527-9543.
313. C. Ni and J. T. Irvine, *Faraday Discuss.*, 2015, **182**, 289-305.
314. C. Graves, S. D. Ebbesen, S. H. Jensen, S. B. Simonsen and M. B. Mogensen, *Nat. Mater.*, 2015, **14**, 239-244.
315. H. Fan, M. Keane, N. Li, D. Tang, P. Singh and M. F. Han, *Int. J. Hydrogen Energy*, 2014, **39**, 14071-14078.
316. Y. F. Tian, W. J. Wang, Y. Liu, L. L. Zhang, L. C. Jia, J. Yang, B. Chi, J. Pu and J. Li, *ACS Appl. Energy Mater.*, 2019, **2**, 3297-3305.
317. S. B. Liu, K. T. Chuang and J. L. Luo, *ACS Catal.*, 2015, **6**, 760-768.
318. R. Lan, K. A. Alkhazmi, I. A. Amar and S. W. Tao, *Appl. Catal. B-Environ.*, 2014, **152**, 212-217.
319. Y. Fan, X. Xi, J. Li, Q. Wang, M.-M. Li, L.-J. Wang, D. Medvedev, J.-L. Luo and X.-Z. Fu, *Electrochim. Acta*, 2021, **393**, 139096.
320. C. C. Duan, J. H. Tong, M. Shang, S. Nikodemski, M. Sanders, S. Ricote, A. Almansoori and R. O'Hayre, *Science*, 2015, **349**, 1321-1326.
321. C. C. Duan, R. J. Kee, H. Y. Zhu, C. Karakaya, Y. C. Chen, S. Ricote, A. Jarry, E. J. Crumlin, D. Hook, R. Braun, N. P. Sullivan and R. O'Hayre, *Nature*, 2018, **557**, 217-222.
322. Y. Zhang, R. Knibbe, J. Sunarso, Y. J. Zhong, W. Zhou, Z. P. Shao and Z. H. Zhu, *Adv. Mater.*, 2017, **29**, 1700132.
323. L. R. Tarutina, J. G. Lyagaeva, A. S. Farlenkov, A. I. Vylkov, G. K. Vdovin, A. A. Murashkina, A. K. Demin and D. A. Medvedev, *J. Solid State Electrochem.*, 2020, **24**, 1453-1462.
324. W. Ruan, X. Yue, J. Ni, D. Xie and C. Ni, *J. Power Sources*, 2021, **483**, 229234.